The parton momentum distributions of the nucleon and A(_QCD)

Peter Neil Harriman

The Parton Momentum Distributions of the Nucleon and Λ_{QCD}

Peter Neil Harriman

Hatfield College

University of Durham

A thesis submitted for the degree of
Doctor of Philosophy
in the Department of Physics,
University of Durham

September 1990

ABSTRACT

Next-to-leading order QCD fits are performed to $F_2^{\mu p}$, $F_2^{\mu n}/F_2^{\mu p}$, $F_2^{\nu Fe}$ and $xF_3^{\nu Fe}$ deep-inelastic scattering data using the $F_2^{\mu p}$ data of either the EMC or BCDMS collaborations, appropriately renormalized for consistency with the re-analysed SLAC F_2^{ep} data.

The parton distributions from these fits are then used to predict next-to-leading order prompt photon production cross-sections. The variation in the quality of the overall description of the deep-inelastic scattering and prompt photon production data simultaneously determines $\Lambda_{\overline{\rm MS}}$ and the form of the gluon distribution of the proton.

Next, cross-sections are predicted at next-to-leading order for the Drell-Yan process. Here, the quality of the overall description determines the antiquark content of the proton.

Two sets of parton distributions are presented according to whether the EMC or BCDMS $F_2^{\mu p}$ data were used in the analysis.

Possible alternatives for the low-x behaviour of the gluon distribution—outside the range of the fitted data—are discussed and predictions are made for future experiments which have the potential to distinguish between these alternatives.

Acknowledgements

I should like to express my thanks to Alan Martin, James Stirling, and Dick Roberts for their many helpful suggestions and their collaboration in three related publications, and also to Patrick Aurenche, Krzysztof Charchula, Jan Kwiecinski, Chris Maxwell, Mike Pennington, Mike Whalley and Marc Virchaux for miscellaneous help and encouragement.

Thanks are also due to the fellow students and postdoctoral researchers without whom this thesis may well have been produced more quickly, but perhaps not as enjoyably: David Barclay, Ahmed Bawa, Nick Brown, Tom Carter, Duncan Curtis, Frank Cuypers, Andrew Eastwood, Mohammad Hussein, Choong Sun Kim, Shabirali Ladha, Foster Langbein, Yanos Michopoulos, Paul Murphy, Anders Nilsson, Cho Ng, Jenny Nicholls, Mohammed Nobary, Magnus Olsson, David Pentney, Alec Schramm, Dave Slaven, Peter Sutton, Neil Shaban, Mike Wade, Dominic Walsh and Simon Webb.

Alan Martin and Peter Sutton were both kind enough to read through the entire thesis for which I'd like to thank them.

I am grateful to Durham University for financing this research

This thesis is dedicated

to the memory of my late father

Warrant Officer John Harriman (RAF)

DECLARATION

I declare that no material in this thesis has previously been submitted for a degree at this or any other university.

Some of this research has been carried out following suggestions from, and using computer programs provided by, Professor A.D. Martin, Dr R.G. Roberts, Dr W.J. Stirling and Dr P. Aurenche and has been published as:

(*i*) " Parton Distributions Extracted from Data on Deep-Inelastic Lepton Scattering, Prompt Photon Production and the Drell-Yan Process"
P.N. Harriman, A.D. Martin, W.J. Stirling & R.G. Roberts,
Phys. Rev. **D42** 798 (1990)

(*ii*) "The Gluon Distribution at Small x: a Phenomenological Analysis"
P.N. Harriman, A.D. Martin, W.J. Stirling & R.G. Roberts,
Phys. Lett. **243B** 421 (1990)

(*iii*) "Phenomenological Consequences of HMRS Partons"
P.N. Harriman, A.D. Martin, W.J.Stirling & R.G. Roberts,
Proceedings of the Workshop on Hadron Structure Functions and Parton Distributions, 26–28th April 1990, Fermilab, Batavia, Illinois, USA.

STATEMENT OF COPYRIGHT

CONTENTS

1. Introduction

Nothing exists except atoms and empty space;
everything else is opinion
Democritos of Abdera, ca. 400 BC

This thesis aims to be a step forward towards the goal of understanding the fundamental structure of matter and the interactions between the fundamental constituents. The quest for this goal has come a long way: matter was found to consist of atoms (Greek for 'indivisible'—an early example of over-optimism!); these were found to comprise a minute central nucleus orbited by electrons; the nucleus was further resolved into protons and neutrons; and we now believe that these are built from quarks, bound together by gluons. As a 'working hypothesis', these are thought to be the truly fundamental particles although to believe this to be true could be considered a contemporary example of over-optimism! With present experiments, we are unable to discern any further substructure of the particles we consider to be fundamental. We have managed, however, to collate all the information we have acquired into a very successful 'Standard Model'. Although some of the pieces of this model have not yet been discovered experimentally (the top quark, Higgs boson and graviton), the model is proving quite resilient to experimental attacks on it which try to show that it is incorrect or incomplete. The Standard Model is, however, only a model and not a 'theory of everything'. There is much in it that is apparently arbitrary—parameters such as fermion masses, coupling constants and mixing angles are not determined by the model and seem to have to be determined empirically. Even the fact that the charge of an electron is an integer multiple of the charge of a quark is not explained by the model.

There is, however, much theoretical speculation on the resolution of these problems and extensions to the Standard Model such as Grand Unified theories [1] (in which all the 'fundamental' forces are low-energy manifestations of one *truly* fundamental force), Supersymmetry [2] (a symmetry relating fermions and bosons) and String Theory [3] (which considers elementary entities to be one-dimensional 'strings' rather than zero-dimensional points). However elegant and appealing these theories may be, the final arbiter on their correctness or otherwise is experimental testing. Today, most of this experimentation is done at high-energy particle accelerators where the most common particle-particle interactions

studied are e^+e^-, e^-p and μ^-p, νp and $\overline{\nu}p$, pp and $p\overline{p}$. It is apparent, then, that the proton is considered a very useful tool in the probing of the interactions of its more-fundamental constituents. It is thus important that we understand the detailed structure of the proton—*how* it is made up of quarks and gluons. Unfortunately, this structure is another example of something in the Standard Model which is not predicted but which has to be decided empirically. However, there have been many experiments dedicated to this end and a wealth of data now exists which, after appropriate analysis, can tell us much about the structure of the proton.

Here, we shall attempt to use this data, in as systematic a way as possible, to determine the most accurate picture of the proton to date, as well as an estimate of a fundamental mass scale, $\Lambda_{\rm QCD}$.

2. Measuring the Proton's Structure

Every statement in physics has to state relations between observable quantities.
Mach's Principle

2.1 Elastic Electron-Proton Scattering

We shall begin our investigation of the detailed structure of the proton by briefly reviewing the not-so-detailed structure revealed in low-energy elastic electron-proton scattering. Details of the derivations of the formulae given are in most elementary textbooks [4], [5], [6] and are not reproduced here. Figure 2.1 defines the notation we shall be using.

The differential cross-section for the case in which the proton is approximated as a spinless point particle is

$$\left(\frac{d\sigma}{d\Omega}\right)_{\text{Mott}} = \frac{\alpha^2}{4E^2\sin^4(\theta/2)}\frac{E'}{E}\cos^2(\theta/2) \tag{2.1}$$

with

$$\frac{E}{E'} = 1 + \frac{2E}{M_P}\sin^2(\theta/2) \tag{2.2}$$

where, as in all that follows, the electron has been assumed to be relativistic ($E \gg m_e$) so that $|\vec{k}| = E$. As indicated, this is known as the Mott cross-section and occurs as a factor in the more realistic cross-sections discussed below. In fact, we can write the cross-section for an electron scattering from an arbitrary charge distribution as

$$\frac{d\sigma}{d\Omega} = \left(\frac{d\sigma}{d\Omega}\right)_{\text{Mott}}|F(\vec{q})|^2 \tag{2.3}$$

where $F(\vec{q})$ is known as a 'form factor' with $\vec{q}$ the (three-)momentum transfer, $\vec{k} - \vec{k}'$. $F(\vec{q})$ is just the Fourier transform of the charge density provided the charge does not recoil:

$$F(\vec{q}) = \int_{\text{all space}} \rho(\vec{x})e^{i\vec{q}\cdot\vec{x}}d^3\vec{x}\ . \tag{2.4}$$

If we now consider a more realistic spin-1/2 proton (still regarding it as a point),

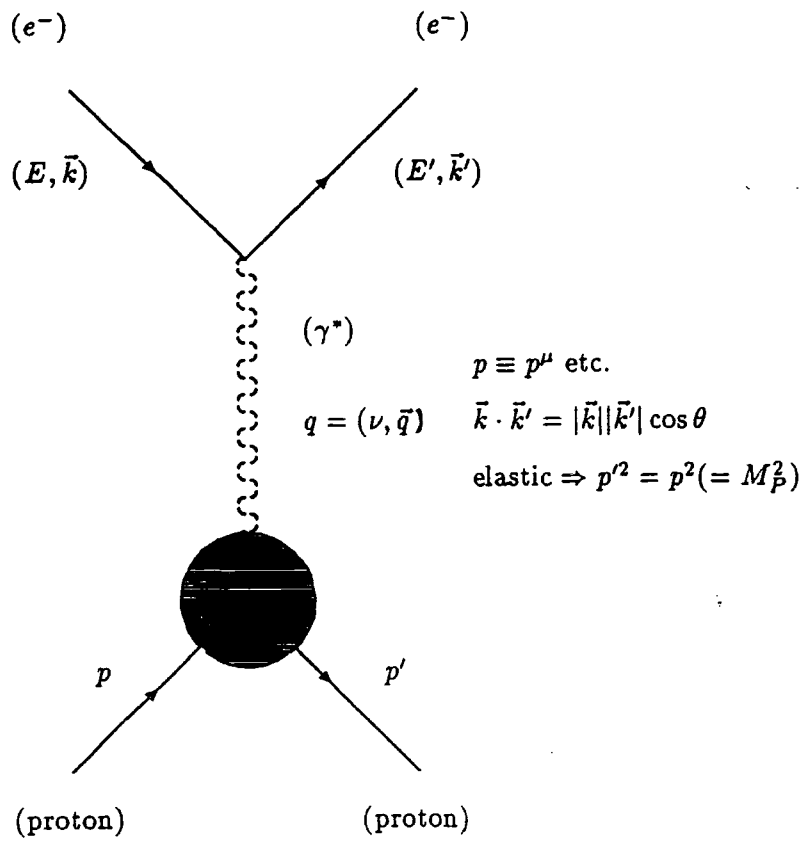

Figure 2.1 Notation for elastic $e^- p$ scattering. The angle between the incident and scattered electron in the LAB frame is θ.

Equation (2.1) is modified to

$$\left(\frac{d\sigma}{d\Omega}\right)_{\text{Dirac}} = \frac{\alpha^2}{4E^2 \sin^4(\theta/2)} \frac{E'}{E} \left(\cos^2(\theta/2) - \frac{q^2}{2M_p^2} \sin^2(\theta/2)\right) \tag{2.5}$$

where it can be seen that the extra term becomes significant for large momentum transfers or large scattering angles, i.e. collisions with small impact parameters. In fact, this term is caused by 'magnetic scattering' and dominates at sufficiently

small distances because the magnetic dipole potential of the proton varies as r^{-2} while the electric potential varies as r^{-1}.

Finally, we consider a wholly realistic spin-1/2 proton with unknown, spatially extended structure. In this case, we can no longer write the proton transition current (used in the derivation of Equation (2.5)) as proportional to γ^μ sandwiched between Dirac spinors as is appropriate for a point-like vertex. Instead, we must replace γ^μ by the most general sum of four-vectors we can construct, each term being multiplied by an arbitrary scalar function of q^2 (being the only independent Lorentz scalar product at the $\gamma^* p$ vertex). Explicitly, relativistic covariance, time-reversal symmetry, and parity conservation imply that

$$\gamma^\mu \longrightarrow F_1(q^2)\gamma^\mu + \frac{\kappa}{2M_P}F_2(q^2)i\sigma^{\mu\nu}q_\nu \tag{2.6}$$

where κ ($= \mu_P^{\text{exp}}/\mu_P^{\text{Dirac}} - 1$—the anomalous magnetic moment of the proton) and M_P have been extracted from (the arbitrary) $F_2(q^2)$ for convenience (i.e. such that in the limit $q^2 \to 0$ when the virtual photon's resolution is so low that it does not 'see' any structure, Equation (2.6) reduces to that of a point particle with anomalous magnetic moment κ, provided we choose $F_1(0) = F_2(0) = 1$).

This general vertex further modifies our differential cross-section to

$$\left(\frac{d\sigma}{d\Omega}\right)_{\text{Rosenbluth}} = \frac{\alpha^2}{4E^2\sin^4(\theta/2)}\frac{E'}{E}\cdot \left(\left(F_1^2 - \frac{\kappa^2 q^2}{4M_P^2}F_2^2\right)\cos^2(\theta/2) - \frac{q^2}{2M_P^2}(F_1+\kappa F_2)^2\sin^2(\theta/2)\right). \tag{2.7}$$

Conventionally, two new form factors are defined as $G_E = F_1 + (\kappa q^2/4M_P^2)F_2$, $G_M = F_1 + \kappa F_2$ such that cross terms F_1F_2 are eliminated:

$$\begin{aligned}\left(\frac{d\sigma}{d\Omega}\right)_{\text{Rosenbluth}} &= \frac{\alpha^2}{4E^2\sin^4(\theta/2)}\frac{E'}{E}\cdot \left[\frac{G_E^2 + \zeta G_M^2}{1+\zeta}\cos^2(\theta/2) + 2\zeta G_M^2\sin^2(\theta/2)\right] \\ &= \left(\frac{d\sigma}{d\Omega}\right)_{\text{Mott}}\left[\frac{G_E^2+\zeta G_M^2}{1+\zeta} + 2\zeta G_M^2\tan^2(\theta/2)\right]\end{aligned} \tag{2.8}$$

with $\zeta = -q^2/4M_P^2$. Now, we should like to interpret the contents of the square bracket in Equation (2.8) as the modulus-squared of the Fourier transform of

the charge density and magnetic moment distributions of the proton (see (2.3)). In fact, it can be shown that $G_E(q^2)$ is the Fourier transform of the charge density distribution and $G_M(q^2)$ is the Fourier transform of the magnetic moment distribution, but only provided that $|\vec{q}| \ll M_P$. This is because we do not have a function of $|\vec{q}|$ as in Equation (2.3), but one of q^2.

These form factors have been determined experimentally and are found to obey the empirical law (see Figure 2.2)

$$G_E = \frac{G_M}{\mu_P} = \left(1 - \frac{q^2}{(0.84)^2}\right)^{-2} \tag{2.9}$$

with q^2 in GeV^2 .

The inverse Fourier transform of this function gives us a charge or magnetic moment distribution which falls exponentially with radius:

$$\rho(r) = \rho_0 e^{-0.84r} \tag{2.10}$$

with r in GeV^{-1} (where 1 $\text{GeV}^{-1} \equiv 0.2$ fm) A typical measure of the electric or magnetic 'size' of the proton is thus (1/0.84) $\text{GeV}^{-1} = 0.24$ fm.

It is apt, at this point, to introduce a piece of notation. Figure 2.2 shows that q^2 is *negative* for a scattering process. This is easily derived: from Figure 2.1, we see that $q^\mu = (E - E', \vec{k} - \vec{k}')$ so that $q^2 = -2(EE' - |k||k'|\cos\theta)$ (neglecting the mass of the proton) which, with our assumption of relativistic speeds, becomes $q^2 \approx -2EE'(1 - \cos\theta)$ which is negative for all θ. We therefore define $Q^2 = -q^2$ for use when it is more convenient.

We should like to resolve more and more structure by increasing Q^2, but if we select only elastic events, we soon run into trouble. For $Q^2 \gg M_P^2$, the Q^2 dependence of the form factors is $G \sim Q^{-4}$ which, on substitution into Equation (2.8) gives

$$\left(\frac{d\sigma}{d\Omega}\right)_{\text{Rosenbluth}} \sim \frac{1}{Q^6} \tag{2.11}$$

i.e. the cross-section for elastic scattering falls rapidly with increasing Q^2. This is because the proton is much more likely to break up when it has to absorb a large amount of four-momentum. In other words, we must understand inelastic scattering if we want to probe the proton with high resolution.

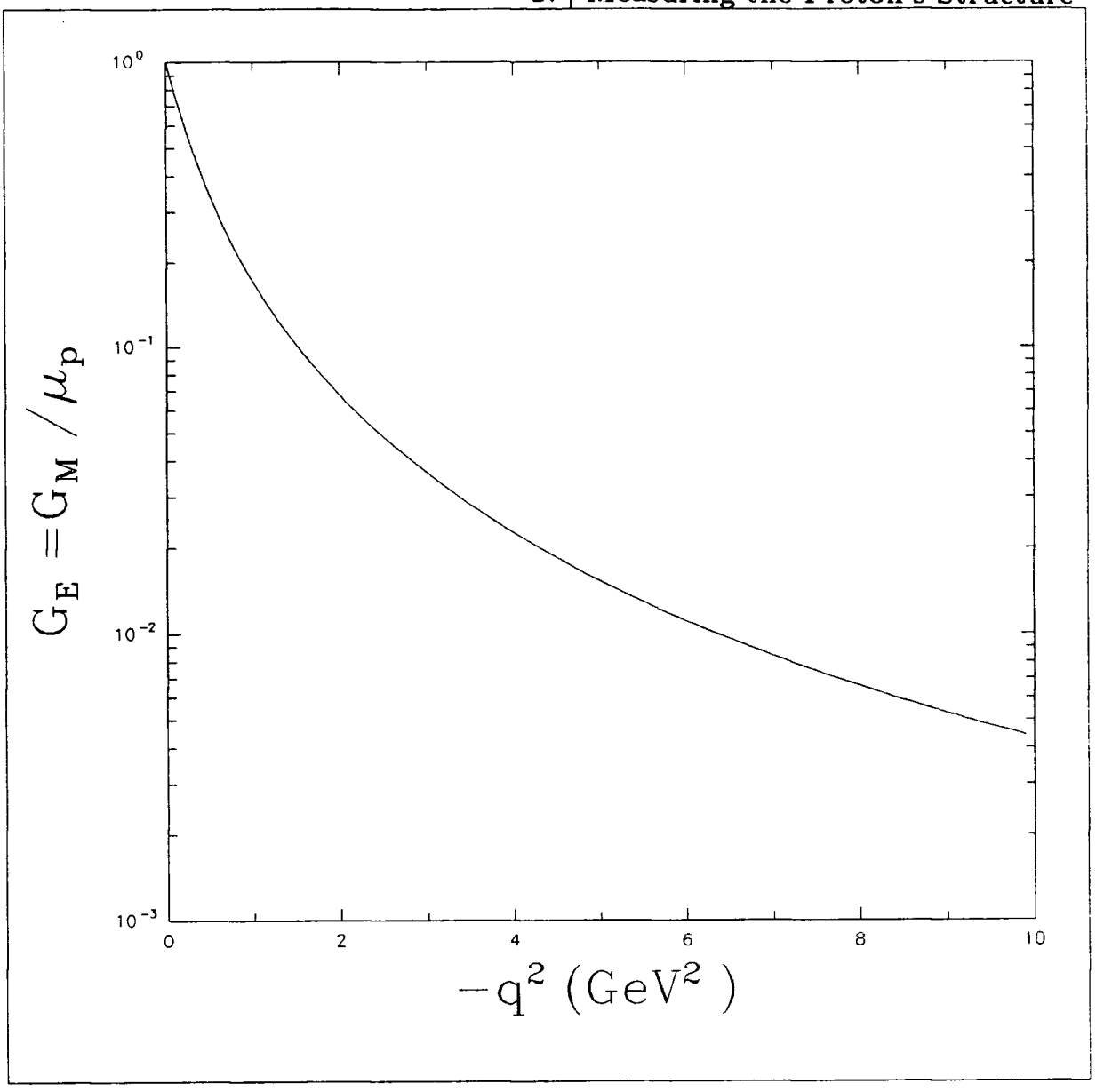

Figure 2.2 The empirical behaviour of the electric (G_E) and magnetic (G_M) form factors of the proton as a function of (the negative of) the square of the four-momentum of the probing virtual photon.

2.2 Inelastic Electron-Proton Scattering

Our notation for inelastic $e^- p$ scattering is given in Figure 2.3 where the invariant mass (sometimes called 'missing mass') of the hadronic fragments of the proton is no longer the constant M_p^2 but the variable W^2. As before, we construct the most general tensor form to represent the blob, introducing arbitrary functions of all the independent Lorentz scalars. As with elastic scattering, we

find two arbitrary functions, but this time, we must make them depend on *two* independent scalars, ν and q^2: $W_1(\nu, q^2)$ and $W_2(\nu, q^2)$. With elastic scattering, $\nu = E - E'$ is not independent of q^2 since $q^2 = -2M_P\nu$ is a consequence of $W^2 = M_P^2$ whereas for inelastic scattering

$$\begin{aligned} W^2 &= (p+q)^2 = M_P^2 + q^2 + 2M_P\nu \\ \Rightarrow q^2 &= W^2 - M_P^2 - 2M_P\nu \ . \end{aligned} \tag{2.12}$$

We thus arrive at a formula analogous to Equation (2.8) :

$$\frac{d^2\sigma}{dE'd\Omega} = \frac{\alpha^2}{4E^2\sin^4(\theta/2)}(W_2(\nu,q^2)\cos^2(\theta/2) + 2W_1(\nu,q^2)\sin^2(\theta/2)) \tag{2.13}$$

or equivalently,

$$\frac{d^2\sigma}{d(-q^2)d\nu} = \frac{\alpha^2}{4E^2\sin^4(\theta/2)}\frac{\pi}{EE'}(W_2(\nu,q^2)\cos^2(\theta/2) + 2W_1(\nu,q^2)\sin^2(\theta/2)) \tag{2.14}$$

(note that the functions $W_{1,2}$ have dimensions $[M]^{-1}$). It is sometimes convenient to replace ν and q^2 by dimensionless variables which range from zero to one, viz.

$$\begin{aligned} x &= \frac{-q^2}{2M_P\nu} \\ y &= \frac{\nu}{E} \end{aligned} \tag{2.15}$$

giving us a third version of Equation (2.13):

$$\frac{d^2\sigma}{dxdy} = \frac{\pi\alpha^2 M_P y}{2EE'\sin^4(\theta/2)}(W_2(x,y)\cos^2(\theta/2) + 2W_1(x,y)\sin^2(\theta/2)) \ . \tag{2.16}$$

The next section will show that x has more significance than that of a convenient variable.

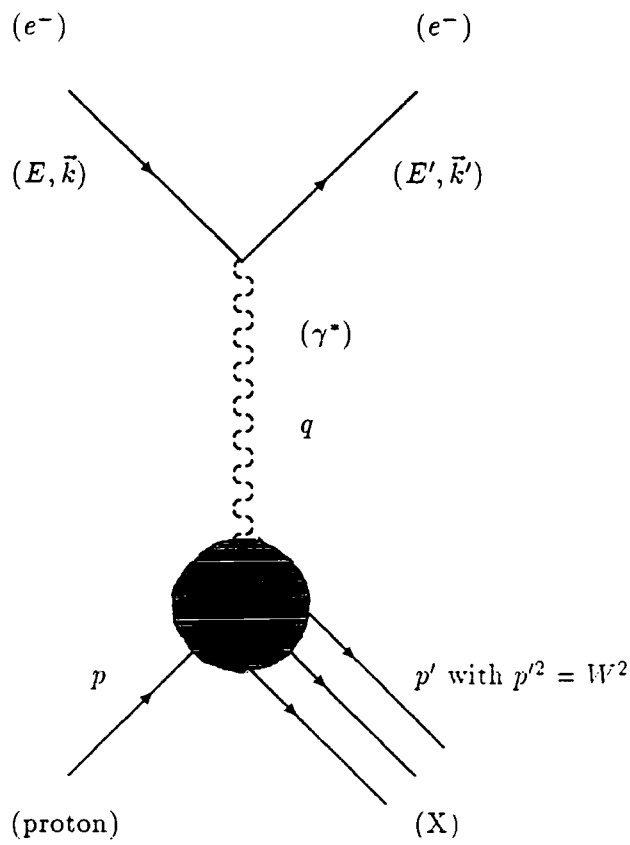

Figure 2.3 Notation for inelastic $e^- p$ scattering.

2.3 The Parton Model

A priori, then, we should expect the functions $W_{1,2}(\nu, q^2)$ to depend on two kinematic variables if the proton were just some arbitrary charge distribution. However, let us see the consequences of imagining the proton to be made up of point-like objects—'partons' [7], [8], [9], [10], [11], [12].

The argument is simplest if we work in a reference frame in which the partons are moving in the same direction as the proton which they compose and that each parton carries a fraction ξ of the proton's four-momentum (usually denoted by 'x' but we do not want to confuse it with the variable defined in §2.2 as $x = -q^2/2M_P\nu$—for the moment, at least) so that

$$p^\mu_{\text{parton}} = \xi p^\mu_{\text{proton}} \cdot \tag{2.17}$$

This is a very odd frame of reference as can be seen by considering what it means for the energy and momentum components under a Lorentz transformation:

$$\begin{aligned} \gamma E - \beta\gamma p &= \xi E \\ -\beta\gamma E + \gamma p &= \xi p \end{aligned} \tag{2.18}$$

(where $p^\mu_{\text{proton}} = (E, 0, 0, p)$). For a non-trivial solution, the determinant of the coefficients of E and p of these homogeneous equations must equal zero giving

$$\begin{aligned} (\xi - \gamma)^2 &= \gamma^2 - 1 \\ \Rightarrow \gamma &= \frac{\xi^2 + 1}{2\xi} \cdot \end{aligned} \tag{2.19}$$

Since ξ is a fraction in the range $0 \leq \xi \leq 1$, we see that the corresponding range in γ is $1 \leq \gamma \leq \infty$ (its entire permitted range). Although γ is formally ξ-dependent, we can see that $\gamma \to \infty$ is an approximate solution of (2.18) for all ξ because in this limit, $E \to p$. This corresponds to the frame in which $(\xi)E \approx (\xi)p$, i.e. the one in which $m = \xi M_P \approx 0$, where m is the mass of the parton. For obvious reasons, this is known as the 'infinite momentum frame'. The advantage of using this frame is that the LAB time required for the proton to absorb the virtual photon is very brief compared with that taken by the proton to disintegrate into the final state, X. Using the Uncertainty Principle, the LAB collision time will be of order $\hbar/\nu$ while the proper time for disintegration will be of order $\hbar/W$ which is $\gamma\hbar/W$ in LAB. A more illuminating way of looking at this situation is to realize that, to the electron, the proton will appear as an infinitesimally-thin (Lorentz-contracted) 'pancake'. Thus, the electron-parton interaction time will be vanishingly small. In contrast, the relative motion of—or 'communication' between—the target parton and the others will appear to

be almost infinitely slow, due to relativistic time dilation. In this frame, then, we can certainly consider the electron as interacting with a *free* parton. This 'impulse approximation' is valid for $-q^2, \nu^2 \gg M_P^2$. Assuming these partons to be spin-1/2 and charge $e_i e$, we can write down the differential cross-section as a Dirac one:

$$\frac{d^2\sigma_i}{d\Omega} = \frac{\alpha^2 e_i^2}{4E^2 \sin^4(\theta/2)} \frac{E'}{E} \left(\cos^2(\theta/2) - \frac{q^2}{2m^2} \sin^2(\theta/2) \right) \tag{2.20}$$

or

$$\frac{d^2\sigma_i}{d(-q^2)d\nu} = \frac{\alpha^2 e_i^2}{4E^2 \sin^4(\theta/2)} \frac{\pi}{EE'} \left(\cos^2(\theta/2) - \frac{q^2}{2m^2} \sin^2(\theta/2) \right) \delta \left(\nu + \frac{q^2}{2m} \right) \tag{2.21}$$

where Equation (2.21) has been written as a double differential cross-section—even though the two variables are not independent—with a 'compensating' δ-function. This is so that it can easily be compared with our inelastic cross-section (2.14) . Summing Equation (2.21) over all partons, i, and performing an integral over all possible ξ values, weighted by the probability $f_i(\xi)$ that the parton has a momentum fraction between ξ and $\xi + d\xi$, we find the correspondence

$$\begin{aligned} W_1(\nu, q^2) &= e_i^2 \sum_i \int_0^1 d\xi f_i(\xi) \frac{-q^2}{4m^2} \delta \left(\nu + \frac{q^2}{2m} \right) \\ W_2(\nu, q^2) &= e_i^2 \sum_i \int_0^1 d\xi f_i(\xi) \delta \left(\nu + \frac{q^2}{2m} \right) \end{aligned} \tag{2.22}$$

and so, using $\delta(z) \equiv a\delta(az)$ with $a = \xi/\nu$ and $m = \xi M_P$, we find

$$\begin{aligned} W_1(\nu, q^2) &= e_i^2 \sum_i \frac{f_i(\xi)}{2M_P} \\ W_2(\nu, q^2) &= e_i^2 \sum_i f_i(\xi) \frac{\xi}{\nu} \end{aligned} \tag{2.23}$$

giving us

$$2\xi M_P W_1(\xi) = \nu W_2(\xi) \tag{2.24}$$

or, defining new dimensionless structure functions $F_{1,2}$ (this is the conventional notation—these F's are not to be confused with the elastic form factors in, for

example, (2.6))

$$F_2(\xi) = \nu W_2(\xi) = \sum_i e_i^2 \xi f_i(\xi) \tag{2.25}$$

and

$$F_1(\xi) = M_P W_1(\xi) = \frac{F_2(\xi)}{2\xi} \tag{2.26}$$

((2.26) is known as the Callan-Gross relation [13] and is a direct consequence of quarks being spin-1/2 particles). ξ is defined via $\delta(\xi + q^2/2M_P\nu)$ to be

$$\xi = \frac{-q^2}{2M_P\nu} \,. \tag{2.27}$$

So we find that this ξ, equal to the fraction of the proton's four-momentum carried by an individual parton in the infinite momentum frame, is indeed equal to the dimensionless variable describing the kinematics of the virtual photon given in (2.15).

This analysis was proposed after Bjorken had predicted [14], [15] that, in the limit

$$\begin{aligned} \nu &\to \infty \\ -q^2 &\to \infty \end{aligned} \tag{2.28}$$

for fixed values of $x = -q^2/2M_P\nu$ (i.e. in the kinematic region in which the impulse approximation is valid), the existence of point-like constituents in the proton would be seen as the degeneration of the two-variable dependence of $M_P W_1(x, q^2)$ and $\nu W_2(x, q^2)$ into dependence on just one dimensionless ratio, viz.

$$\begin{aligned} M_P W_1(\nu, q^2) &\to F_1(x) \\ \nu W_2(\nu, q^2) &\to F_2(x) \,. \end{aligned} \tag{2.29}$$

Now this is not a very remarkable 'prediction' unless the functions $F_{1,2}(x)$ are non-zero and non-infinite since, otherwise, *all* two-variable functions have this behaviour. But, looking at Equation (2.25), and recalling that $f_i(x)$ is a probability and that x ranges from zero to one as well, Bjorken's prediction is that these functions *are* finite.

Do experimental data support this hypothesis? Figure 2.4 shows the most accurate data currently available for $\nu W_2(\nu, Q^2)$ from the BCDMS collaboration: (a) versus x for many different Q^2 values and (b) versus Q^2 for different x values. Bearing in mind that we have no idea how 'close' we are to the limits where the impulse approximation is valid, it is quite impressive that νW_2 does indeed seem to be a function of x with little Q^2 dependence. Although there is obviously *some* Q^2 dependence, this is to be contrasted with that of G_E^2, the square of the elastic form factor, which decreases as the fourth power of Q^2!

2.4 Scattered Partons and Spectroscopic Quarks

Three years before Bjorken made his hypothesis, Gell-Mann [17] and Zweig [18] had postulated the existence of baryon and meson constituents on the basis of the regularities occurring when baryons and mesons of a given J^P were displayed on axes labelled by the z-component of isospin and the quantum number 'strangeness'. It was found that almost all the known mesons and baryons had values of these quantum numbers consistent with their being composed of just three different 'quarks' (plus their corresponding antiparticles) which were named 'up', 'down', and 'strange' (denoted by u, d and s respectively). More recent baryon spectroscopy has shown that a further two quarks are needed to account for additional baryons that have been discovered. These are known as 'charm' (c) and 'bottom' (or, rarely, 'beauty') (b). Given the success of this 'Quark Model' in accounting for the known baryons, it was obvious to try to identify these quarks with the partons found in deep-inelastic scattering.

We might first check that we can account for all the momentum of a proton or a neutron. The Quark Model tells us that a proton is made up of the three quarks uud and the neutron ddu. Denoting the functions $f_i(x)$, introduced in Equation (2.22), by $u(x), d(x), s(x), c(x)$ and $b(x)$ where $xf_i(x)dx$ is understood to be the probability of finding that type ('flavour') of quark with a momentum fraction between x and $x + dx$ *in a proton*, and using the fact that the proton and neutron are members of the same isospin doublet with

$$u(x) \equiv u^{proton}(x) = d^{neutron}(x) \tag{2.30}$$

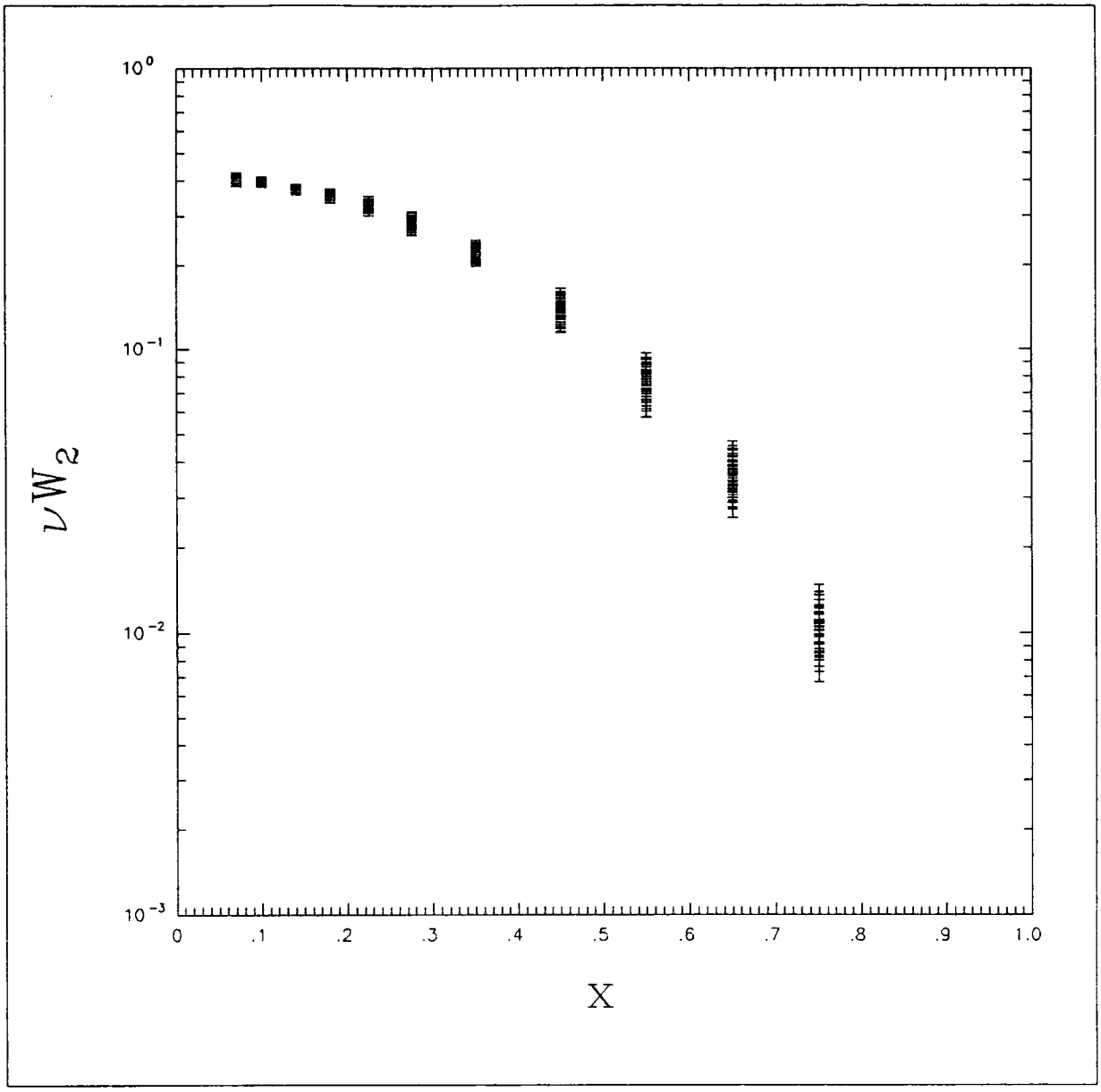

Figure 2.4(a) Data on the νW_2 structure function of the proton obtained from the BCDMS collaboration [16] by scattering muons off a hydrogen target. The data for all the Q^2 values at each value of x have been shown together with the experimental error bars (the statistical and systematic errors added in quadrature). At a given x, the higher Q^2 values are the lower data points. The data shown here are the same as those in Figure 2.4(b) so that the rightmost 'tower' of points at $x = 0.75$ in this Figure corresponds to the lowest, almost horizontal, band of points in Figure 2.4(b).

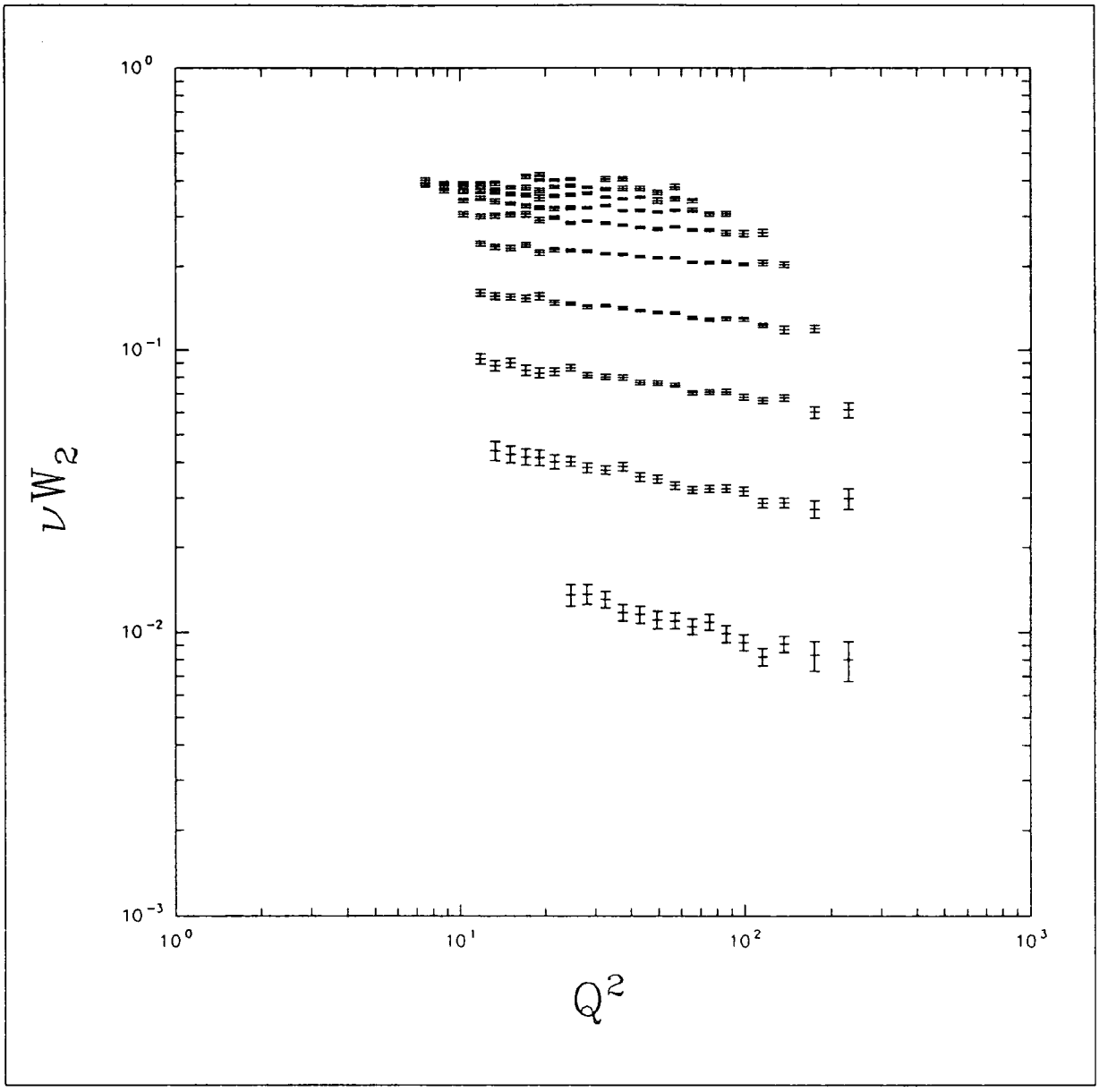

Figure 2.4(b) Data on the νW_2 structure function of the proton obtained from the BCDMS collaboration [16] by scattering muons off a hydrogen target. The data for all the x values at each value of Q^2 have been shown together with the experimental error bars (the statistical and systematic errors added in quadrature). At a given Q^2, the higher x values are the lower data points. The data shown here are the same as those in Figure 2.4(a) so that the lowest, almost horizontal, band of points in this Figure corresponds to the rightmost 'tower' of points at $x = 0.75$ in Figure 2.4(a).

and

$$d(x) \equiv d^{proton}(x) = u^{neutron}(x) \tag{2.31}$$

we can integrate (2.25) to find

$$\begin{aligned}
\int_0^1 dx F_2^p(x) &= \int_0^1 dx x \left(\left(\frac{2}{3}\right)^2 (u+\overline{u}) + \left(-\frac{1}{3}\right)^2 (d+\overline{d}) \right) \\
\int_0^1 dx F_2^n(x) &= \int_0^1 dx x \left(\left(\frac{2}{3}\right)^2 (d+\overline{d}) + \left(-\frac{1}{3}\right)^2 (u+\overline{u}) \right)
\end{aligned} \tag{2.32}$$

where we have used the fact that the charge of a u quark is $\frac{2}{3}e$ and that of a d quark $-\frac{1}{3}e$ and we assume any s quark content is small. From experiment, the integrals of F_2^p and F_2^n in (2.32) are approximately 0.18 and 0.12 respectively. Solving the two equations then gives

$$\int_0^1 x(u+\overline{u}+d+\overline{d})dx = 0.54 \; . \tag{2.33}$$

We seem to have 'lost' almost half of the total momentum. More precisely, this tells us that about half of the proton's momentum is carried by partons with no electromagnetic charge.

The successful predictions of the Quark-Parton Model demonstrate that it is quite close to the truth about the structure of the proton. However, we should like a theory which explains why there are scaling violations and tells us what uncharged particles carry about 46% of the proton's momentum. That theory is discussed in Chapter 3.

2.5 Neutrino-Proton Scattering

The kinematics needed to describe (charged-current) neutrino-proton scattering ($\nu(\overline{\nu})p \to \mu^-(\mu^+)X$) are essentially the same as for e^-p scattering, but differing in one important respect. We can no longer assume parity conservation when deducing the form of the most general tensor to represent the proton 'blob' since weak interactions violate parity conservation. This requires us to have *three*

independent functions of the two independent Lorentz scalars—$W_{1,2,3}^{(\nu,\overline{\nu})}(\nu, q^2)$ — and the differential cross-section*

$$\begin{aligned}\frac{d^2\sigma^{(\nu,\overline{\nu})}}{d(-q^2)d\nu} = \frac{G_F^2}{2\pi}\frac{E'}{E}(W_2^{(\nu,\overline{\nu})}\cos^2(\theta/2) + 2W_1^{(\nu,\overline{\nu})}\sin^2(\theta/2) \\ \mp \frac{E+E'}{M_P}W_3^{(\nu,\overline{\nu})}\sin^2(\theta/2))\end{aligned} \tag{2.34}$$

where $\nu - p$ scattering takes the $-$ sign and $\overline{\nu} - p$ takes the $+$ sign and we are assuming the approximation

$$\frac{\pi^2\alpha^2}{2\sin^4\theta_W(q^2 + M_W^2)^2} \approx G_F^2 \tag{2.35}$$

where G_F is the Fermi constant, θ_W the weak mixing angle and M_W the mass of a W boson. In other words, we are replacing the virtual W propagator by a (dimensionful) four-point coupling (see Figure 2.5). (We note here that the neutrino scattering data we shall be using later—essentially the W_i's—were extracted from the measured differential cross-sections without making this approximation.)

As before, we define dimensionless structure functions which scale in the Bjorken limit (2.28) for fixed values of $x = -q^2/2M_P\nu$:

$$\begin{aligned}M_P W_1^{(\nu,\overline{\nu})} &= F_1^{(\nu,\overline{\nu})} \\ \nu W_{2,3}^{(\nu,\overline{\nu})} &= F_{2,3}^{(\nu,\overline{\nu})}\ .\end{aligned} \tag{2.36}$$

In the Parton Model, we find†

$$\begin{aligned}F_2^{\nu p} &= 2x(d + s + b + \overline{u} + \overline{c}) \\ F_2^{\overline{\nu} p} &= 2x(\overline{d} + \overline{s} + \overline{b} + u + c) \\ xF_3^{\nu p} &= 2x(d + s + b - \overline{u} - \overline{c}) \\ xF_3^{\overline{\nu} p} &= 2x(-\overline{d} - \overline{s} - \overline{b} + u + c)\ .\end{aligned} \tag{2.37}$$

The neutrino-neutron scattering versions of these are obtained simply by making the replacements $d \leftrightarrow u$ and $\overline{d} \leftrightarrow \overline{u}$. Thus, for an isoscalar target (equal numbers

* Equation (13.106a) in [6] is incorrect: dq^2 should be $d(-q^2)$ or $d|q^2|$. Equation (11.101) is correct

† these formulae are for the case of only five flavours of quark. To include a sixth (t) quark, make the replacements $u \to u + t$ and $\overline{u} \to \overline{u} + \overline{t}$

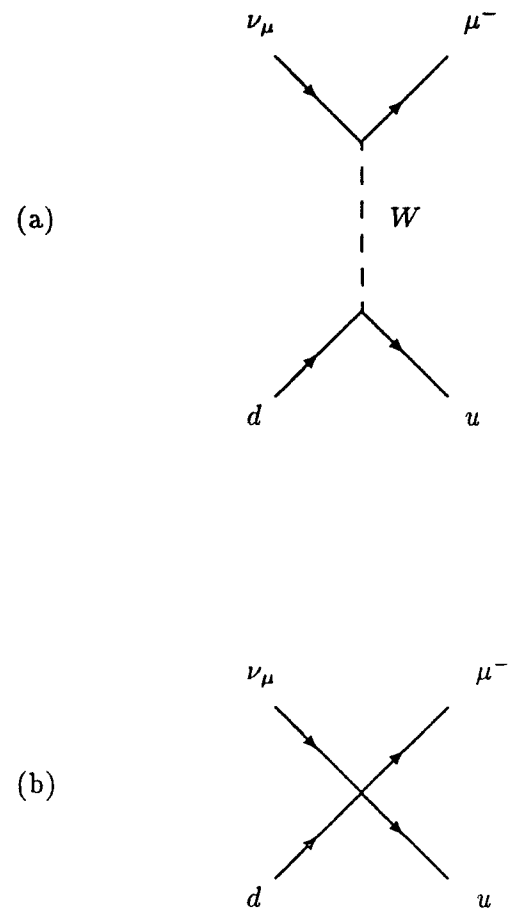

Figure 2.5 (a) shows a neutrino-quark interaction proceeding via a virtual W boson propagator and (b) the same interaction in the low-energy approximation of a four-point interaction.

of protons and neutrons), such as a deuteron, we obtain (by averaging)

$$\begin{aligned} F_2^{\nu d} &= x(d + \overline{d} + u + \overline{u} + 2s + 2\overline{c} + 2b) \\ F_2^{\overline{\nu} d} &= x(d + \overline{d} + u + \overline{u} + 2\overline{s} + 2c + 2\overline{b}) \\ xF_3^{\nu d} &= x(d_V + u_V + 2s - 2\overline{c} + 2b) \\ xF_3^{\overline{\nu} d} &= x(d_V + u_V - 2\overline{s} + 2c - 2\overline{b}) \end{aligned} \tag{2.38}$$

where, for example, $u_V \equiv u - \overline{u}$. Finally, taking the sum of the measured cross-

sections for ν scattering and $\overline{\nu}$ scattering, we can determine the $\nu - \overline{\nu}$-averaged function

$$\tilde{F}_2^{\nu d} = x \sum (q + \overline{q}) \tag{2.39}$$

(where the summation runs over $q = u, d, s, c, b$) and by taking the difference of the measured cross-sections we can determine the corresponding version for xF_3

$$x\tilde{F}_3^{\nu d} = u_V + d_V \tag{2.40}$$

where we have assumed that the non-valence flavour quarks and antiquarks occur in equal numbers, e.g. $s - \overline{s} = 0$. An unfortunate piece of conventional notation dictates that the tildes are not usually written to indicate $\nu - \overline{\nu}$-averaged functions in Equations (2.39) and (2.40) because experimentally-quoted values of these functions are invariably averaged ones. Henceforth, we shall follow this convention.

As for $\mu^- - p$ scattering, the F_1^ν structure function is simply related to the F_2^ν structure function by (2.26) in the Quark-Parton Model.

3. Improving the Quark Parton Model—QCD

The aim of research is the discovery of the equations which subsist between the elements of phenomena.
Ernst Mach, *Popular Scientific Lectures*

3.1 Gluons and Colour

In Chapter 2, we noted the fact that about 46% of the proton's momentum must be carried by uncharged particles. We also know that the force responsible for holding a baryon together cannot be electromagnetic in origin since we know of some baryons which are composed of three like-charge quarks, for example Δ^{++} (uuu), Δ^{-} (ddd), Ω^{-} (sss), and Ξ^{-} (dss). In addition, some baryons appear to have three identical quarks in the same quantum state, in apparent violation of the Pauli exclusion principle—*apparent* violation because we are making the judgement on the basis of the quantum numbers we know about.

In quantum chromodynamics (QCD) [19], [20], [21], the resolution of all these problems is achieved by postulating the existence of an exchange force between quarks, mediated by electrically-neutral particles—'gluons'. These couple to a new quark quantum number known as colour. By having three different colour 'charges' (often denoted by R(ed), B(lue), and G(reen)), we can avoid the problem with fermion statistics mentioned above by postulating that the three, otherwise identical quarks, in fact each carry a different colour charge. Finally, because we have never seen any experimental evidence for this new quantum number, we postulate that all hadrons (baryons and mesons) carry no net colour. In group-theoretical language, we are proposing that quarks are in a triplet representation of an exact SU(3) colour symmetry group and that hadrons are always colour singlets. The symmetry implied by SU(3) is that the laws of physics remain unchanged by 'rotations' in colour space* e.g. if we were to change the colour of all quarks in a system by $R \rightarrow B$, $B \rightarrow G$, $G \rightarrow R$, there would be no physical consequences. The gluons arise if we insist that this symmetry be *local*, i.e. that we can make *independent* 'rotations' in colour space at every space-time point such that physics is unchanged. This local gauge field theory is non-Abelian

* SU(3) is not the same as O(3), which is the group for rotations in 3-space, so we cannot think of R,G and B as being 'the x, y and z axes'.

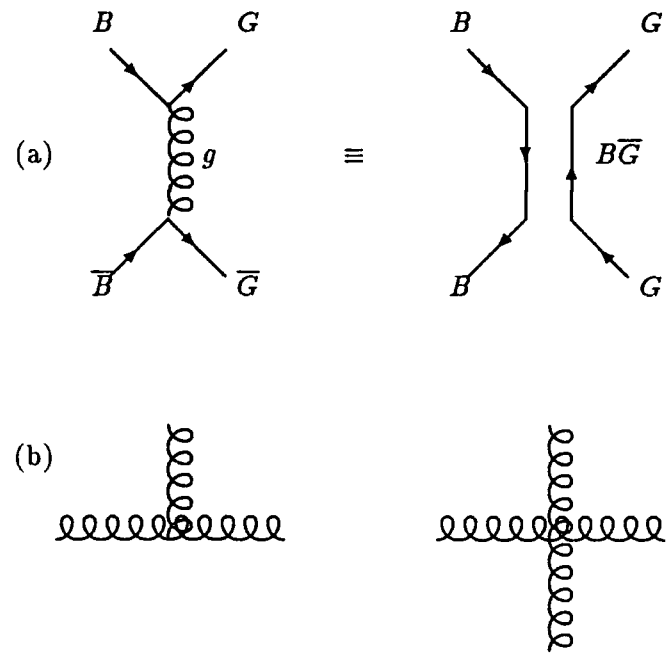

Figure 3.1 (a) The colour content of a gluon and (b) three-gluon and four-gluon vertices.

which means that the gluons themselves also carry the colour charge (unlike in quantum electrodynamics (QED) where photons are uncharged). We can picture the interaction between, say, a B quark and an anti-B quark as in Figure 3.1(a) therefore identifying gluons as particles with colour content $c_1\overline{c_2}$. There are thus nine gluons possible taking all colour-anticolour combinations, but the colour-singlet combination, $(R\overline{R}+B\overline{B}+G\overline{G})/\sqrt{3}$ decouples leaving us with eight which are in the octet representation of SU(3). Since they carry colour charge, gluons can also couple to other gluons as in Figure 3.1(b).

3.2 Gluons in the Parton Model—Scaling Violations

The existence of gluons within the proton will affect the differential cross-sections we derived in Chapter 2 since we must now allow for the possibility of interactions such as those shown in Figure 3.2, where (a) the interacting quark radiates a real gluon before or after interaction with the virtual photon and (b) where a gluon from the proton creates a $q\overline{q}$ pair. An obvious consequence of these diagrams is that the scattered quark is now able to acquire some transverse momentum with respect to the virtual photon whereas, previously, the only transverse momentum it could have was that demanded by the uncertainty principle for a quark confined within the size of a proton ($< p_T^2 > \sim (0.3\ \mathrm{GeV})^2$).

There is another consequence of the presence of gluons in the theory, of great importance to the analysis of physical structure functions, of which we will give a brief derivation. Let us define a single parton version of F_2—the F_2 structure function before it has been convoluted with the probability distribution, $f_i(x)$, and summed over all partons (see (2.22))—denoting it by $\hat{F}_2$. Let the initial and final momentum fractions of the quark be different as in Figure 3.3 to allow for gluon radiation. Then we can recover the structure function F_2 by integrating over all y and z subject to the conservation of momentum condition $x = zy$, and summing over partons

$$F_2(x,Q^2) = \sum_i \int_0^1 dz \int_x^1 dy f_i(y) \hat{F}_2(z,Q^2) \delta(x - zy) \tag{3.1}$$

where the lower limit of $y = x$ is because the incoming parton of momentum yp *loses* some momentum by radiating a gluon. By using $\delta(x - zy) = \delta(x/y - z)/y$, we can do the z integral to obtain

$$F_2(x,Q^2) = \sum_i \int_x^1 \frac{dy}{y} f_i(y) \hat{F}_2(x/y,Q^2) \ . \tag{3.2}$$

In the quark parton model, of course, $\hat{F}_2(x/y) = x e_i^2 \delta(1 - x/y)$ since $y = x$ whereby (3.2) reduces back to

$$F_2(x) = \sum_i e_i^2 x f_i(x) \ . \tag{3.3}$$

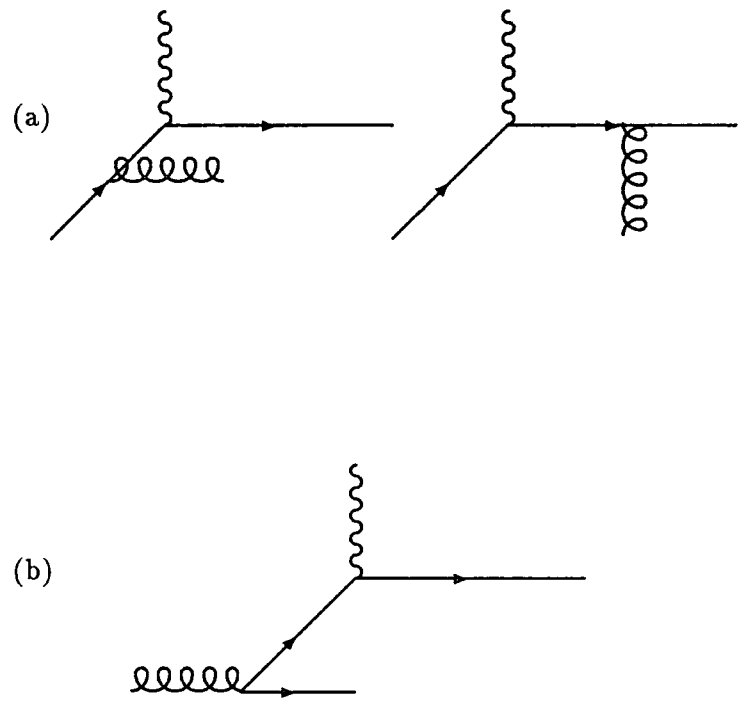

Figure 3.2 (a) New diagrams to allow for gluon radiation and (b) a gluon from the proton 'dissociates' into a quark-antiquark pair.

Now, we can incorporate the parton process $\gamma^* q \rightarrow gq$ into our description of deep-inelastic scattering. It can easily be shown (see, for example, [5]) that, for this process, the differential cross-section can be written as

$$\frac{d\hat{\sigma}}{dp_T^2} = e_i^2 \frac{4\pi\alpha^2}{\hat{s}} \frac{1}{p_T^2} \frac{\alpha_s}{2\pi} P_{qq}(z) \tag{3.4}$$

where p_T is the quark (or gluon) transverse momentum in the COM frame, $\hat{s}$ is the square of the COM energy of $\gamma^* q^{initial}$ or gq^{final}, z is as in Figure 3.3

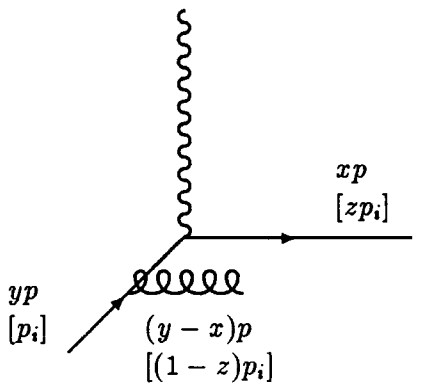

Figure 3.3 Notation for the gluon radiation diagram. p is the momentum of the proton and p_i that of the initial-state quark.

and α_s is the coupling constant of QCD. For simplicity, (3.4) is written in the high-energy limit ($\hat{s}$ large). The function P_{qq} is given by*

$$P_{qq}(z) = \frac{4}{3}\left(\frac{1+z^2}{1-z}\right) \tag{3.5}$$

and is some measure of (see later) the probability that a quark of momentum p_i emits a gluon so becoming a quark with momentum fraction zp_i. Integrating

* but see §3.3

(3.4) over p_T^2, we find

$$\hat{\sigma} = \frac{4\pi\alpha^2}{\hat{s}}\hat{F}_2^{\,rad}(z) \approx e_i^2\frac{4\pi\alpha^2}{\hat{s}}\frac{\alpha_s}{2\pi}P_{qq}(z)\ln(Q^2/\mu^2) \tag{3.6}$$

where an upper limit of $p_T^2 = \hat{s}/4 = Q^2(1-z)/4z$ and a lower limit of μ^2 have been used with $\ln(\hat{s}/4) \approx \ln Q^2$ for large Q^2. $\hat{s}/4$ is the maximum transverse momentum of the gluon or final state quark and μ^2 is used instead of zero to prevent the divergence at $p_T^2 = 0$. The label *rad* reminds us that this contribution is due to gluon radiation.

Since this is a process distinguishable from $\gamma^* q \to q$, we can add probabilities (instead of amplitudes) to obtain

$$\frac{F_2(x)}{x} = \sum_i \int_x^1 \frac{dy}{y} f_i(y) \frac{\hat{F}_2^{\,tot}(x/y)}{x} \tag{3.7}$$

where

$$\frac{\hat{F}_2^{\,tot}(x/y)}{x} \equiv \frac{\hat{F}_2(x/y) + \hat{F}_2^{\,rad}(x/y)}{x} = e_i^2\left(\delta(1-x/y) + \frac{\alpha_s}{2\pi}P_{qq}(x/y)\ln(Q^2/\mu^2)\right) . \tag{3.8}$$

Now we see that the F_2 structure function no longer 'scales'—it has gained a $\ln Q^2$ dependence. A neat way of rewriting (3.7) is to absorb the extra, gluon-induced piece of (3.8) into the probability functions $f_i(y)$:

$$\begin{aligned} F_2/x &= \sum_i \int_x^1 \frac{dy}{y} e_i^2 \delta(1-x/y)[f_i(y) + \Delta f_i(y, Q^2)] \\ &= \sum_i e_i^2 (f_i(x) + \Delta f_i(x, Q^2)) \end{aligned} \tag{3.9}$$

with

$$\Delta f_i(x, Q^2) = \frac{\alpha_s}{2\pi}\ln(Q^2/\mu^2)\int_x^1 \frac{dy}{y} f_i(y) P_{qq}(x/y) . \tag{3.10}$$

Differentiating with respect to $\ln Q^2$, we obtain

$$\frac{\partial(\Delta f_i(x, Q^2))}{\partial \ln Q^2} = \frac{\alpha_s}{2\pi}\int_x^1 \frac{dy}{y} f_i(y) P_{qq}(x/y) \tag{3.11}$$

but we may expand $f_i(y)$

$$\begin{aligned} f_i(y) &= f_i(y,Q^2) - \Delta f_i(y,Q^2) \\ &= f_i(y,Q^2) - O(\alpha_s) \end{aligned} \tag{3.12}$$

and use

$$\frac{\partial(\Delta f_i(x,Q^2))}{\partial \ln Q^2} = \frac{\partial f_i(x,Q^2)}{\partial \ln Q^2} \tag{3.13}$$

to obtain

$$\frac{\partial f_i(x,Q^2)}{\partial \ln Q^2} = \frac{\alpha_s}{2\pi}\int_x^1 \frac{dy}{y} f_i(y,Q^2) P_{qq}(x/y) \ . \tag{3.14}$$

This simply states that, when increasing the resolution of the virtual photon (by increasing its Q^2), an increasing number of quarks are seen at smaller values of x (*smaller* since $y \geq x$) due to the possibility that quarks may degrade their momentum by radiating gluons.

We showed in Figure 3.2b that we have also to consider the case when a gluon from the proton 'dissociates' into a $q\overline{q}$ pair, one of which interacts with the virtual photon. Proceeding in the same way as before, we find that the contribution to F_2/x from this process is

$$\sum_i e_i^2 \int_x^1 \frac{dy}{y} g(y) \frac{\alpha_s}{2\pi} P_{qg}(x/y) \ln(Q^2/\mu^2) \tag{3.15}$$

where

$$P_{qg}(z) = \frac{1}{2}(z^2 + (1-z)^2) \tag{3.16}$$

gives some measure of the probability of a gluon dissociating into a $q\overline{q}$ pair leaving the gluon with a fraction z of its original momentum, and $g(x)$ is the probability distribution for gluons analogous to the $f_i(x)$ for quarks. This is obviously another contribution we must add to (3.14) leading to

$$\frac{\partial q_i(x,Q^2)}{\partial \ln Q^2} = \frac{\alpha_s}{2\pi}\int_x^1 \frac{dy}{y}(q_i(y,Q^2)P_{qq}(x/y) + g(y,Q^2)P_{qg}(x/y)) \tag{3.17}$$

where we have changed notation from f_i to q_i to emphasize the difference between the quark and gluon pieces. Now, clearly, the gluon probability distribution in

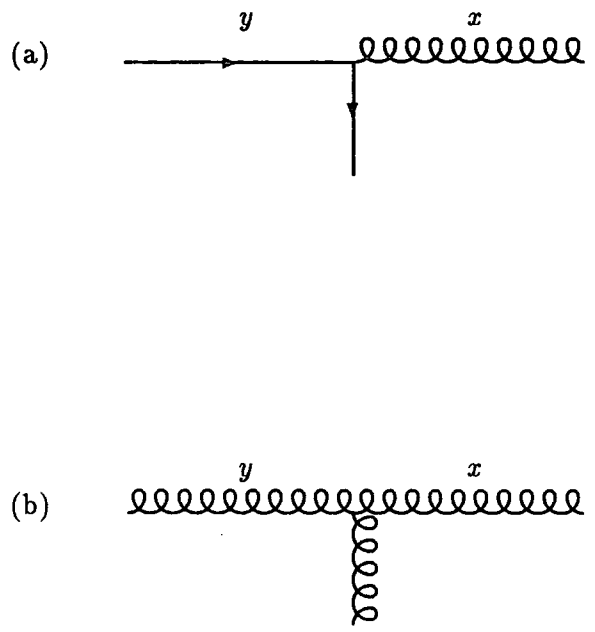

Figure 3.4 The splitting functions (a) P_{gq} and (b) P_{gg}

the proton must also be changing. We obviously have the case shown in Figure 3.4(a) represented by P_{gq}, but due to the allowed three-gluon vertex in QCD, we also have the case shown in Figure 3.4(b) represented by P_{gg}. So, we obtain

$$\frac{\partial g(x,Q^2)}{\partial \ln Q^2} = \frac{\alpha_s}{2\pi}\int_x^1 \frac{dy}{y}\left(\sum_{i=1}^{2N_F} q_i(y,Q^2)P_{gq}(x/y) + g(y,Q^2)P_{gg}(x/y)\right) \tag{3.18}$$

where $2N_F$ implies that the summation is over all quarks *and* antiquarks and where the splitting functions are found to be

$$P_{gq}(z) = \frac{4}{3}\frac{1+(1-z)^2}{z} \tag{3.19}$$

and*

$$P_{gg}(z) = 6\left(\frac{1-z}{z} + \frac{z}{1-z} + z(1-z)\right) . \tag{3.20}$$

Equations (3.17) and (3.18) are known as the Altarelli-Parisi equations [22], [23], [24].

⋆ but see §3.3

3.3 Virtual Gluon Corrections

So far, we have ignored the $z \to 1$ singularities in $P_{qq}(z)$ and $P_{gg}(z)$ when the final parton emerges with the same momentum fraction as the initial parton. Clearly, the probability for this to happen is not infinite, so what have we forgotten? We have, in fact, omitted some diagrams which always have $z = 1$. In addition to Figure 3.2 we must also include the virtual gluon diagrams of Figure 3.5. If we identify the term

$$\delta(1-z) + \frac{\alpha_s}{2\pi} P_{qq}(z) \ln(Q^2/\mu^2) \tag{3.21}$$

(see, for example, (3.8)) as the probability per unit z that a quark of momentum p_i appears to be a quark with momentum zp_i, then the integral of (3.21) over all z must be unity, giving

$$\begin{aligned} \int_0^1 dz(\delta(1-z) + \frac{\alpha_s}{2\pi} P_{qq}(z) \ln(Q^2/\mu^2)) = 1 \\ \Rightarrow \int_0^1 P_{qq}(z) dz = 0 \ . \end{aligned} \tag{3.22}$$

We can therefore add a contribution to our (incomplete) P_{qq} to ensure this condition is satisfied. In fact,

$$\int_0^1 \left[\frac{4}{3} \frac{z^2-1}{1-z} + 2\delta(1-z) \right] dz = 0 \tag{3.23}$$

thus showing that

$$P_{qq}(z) = \frac{4}{3} \frac{z^2-1}{1-z} + 2\delta(1-z) \tag{3.24}$$

is the required function. This is often written using the 'plus-prescription' defined by

$$\int_0^1 dx \frac{h(x)}{(1-x)_+} \equiv \int_0^1 dx \frac{h(x) - h(1)}{(1-x)} = \int_0^1 dx \ln(1-x) \frac{dh(x)}{dx} \tag{3.25}$$

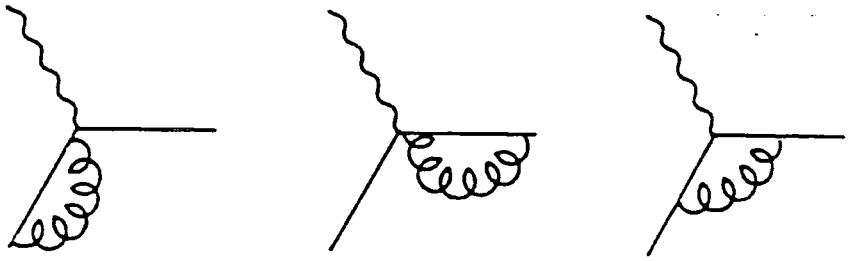

Figure 3.5 Virtual gluon corrections to the process $\gamma^* q \to q$.

as

$$P_{qq}(z) = \frac{4}{3}\frac{1+z^2}{(1-z)_+} + 2\delta(1-z) \; . \tag{3.26}$$

Similarly, the corrected Pgg is given by

$$P_{gg} = 6\left(\frac{1-z}{z} + \frac{z}{(1-z)_+} + z(1-z)\right) + \frac{1}{6}(33 - 2N_F)\delta(1-z) \; . \tag{3.27}$$

3.4 The Strong Coupling, α_s

Another assumption we have made up till this point is that the strong coupling, α_s, is a constant. In fact, there are virtual corrections to the $q-g$ vertex (shown in Figure 3.6) which have the effect of making α_s 'run', that is, it becomes a function of Q^2. In the leading logarithm approximation (see §3.5 and §3.6), $\alpha_s(Q^2)$ turns out to be the solution of the differential equation

$$\frac{d\alpha_s(Q^2)}{d\ln Q^2} = -\frac{\beta_0}{4\pi}\alpha_s(Q^2)^2 \tag{3.28}$$

that is

$$\alpha_s(Q^2) = \frac{4\pi}{\beta_0 \ln(Q^2/\Lambda^2)} \tag{3.29}$$

where the integration has produced an arbitrary constant Λ,to be determined by experiment and where β_0 is a calculable function arising from the evaluation of the virtual correction diagrams:

$$\beta_0 = 11 - \frac{2}{3}N_F \; . \tag{3.30}$$

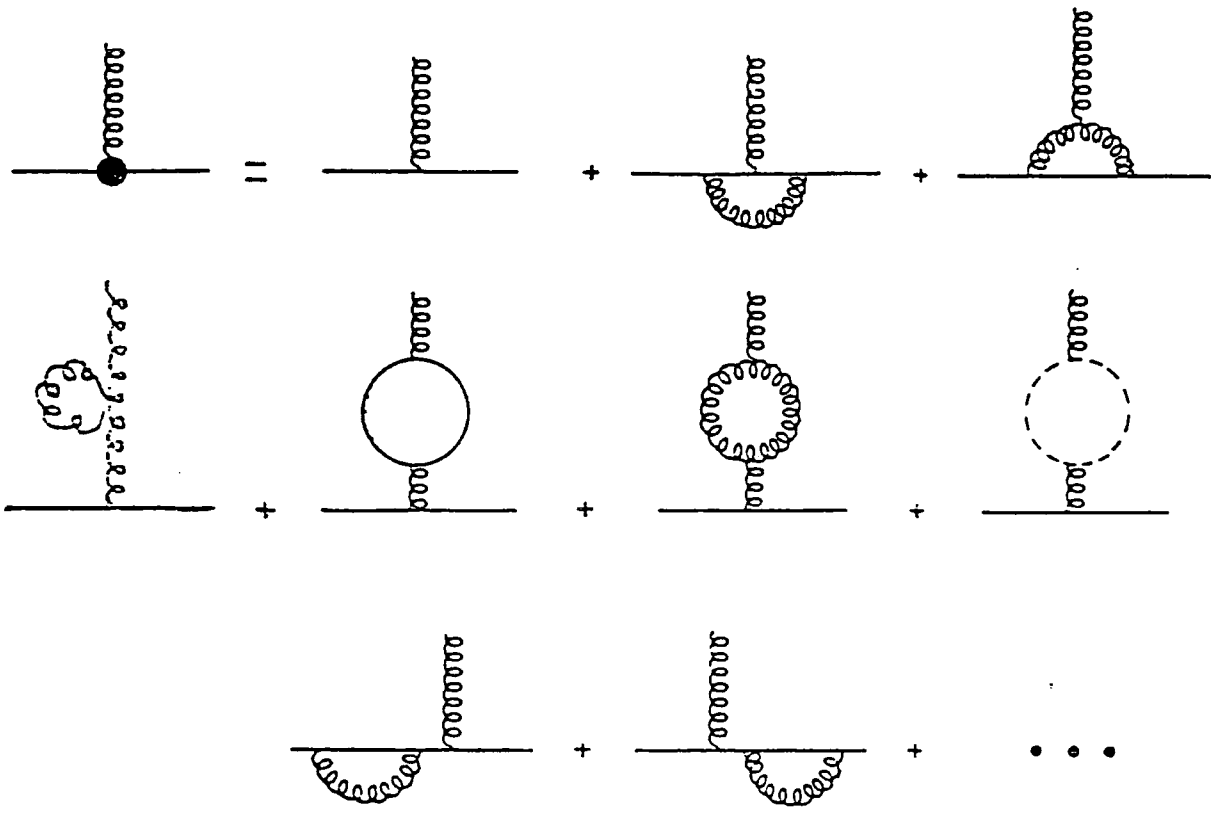

Figure 3.6 The full quark-gluon vertex decomposed into the 'bare' vertex and one-loop virtual-particle corrections (the dashed-line circle is a 'ghost'—a fictitious particle whose diagrams must be included when calculations are done in covariant gauges).

In this leading logarithm approximation, the Altarelli-Parisi equations can be corrected for the dependence of α_s on Q^2 simply by replacing α_s by $\alpha_s(Q^2)$. We thus see that in QCD when there are less than 16 flavours of quark (currently, there are five known flavours of quark and a sixth is postulated in the Standard Model), the coupling goes asymptotically to zero for $Q^2 \to \infty$ and becomes very large as Q^2 approaches Λ^2. These two properties are known respectively as 'asymptotic freedom' [25], and 'infra-red slavery' [11], and are dispayed graphically in Figure 3.7. This is in contrast to QED where the coupling *increases* with Q^2 because β_0^{QED} is negative. Physically, the reason for this is that a bare electric charge tends to get shielded by the cloud of virtual e^+e^- charges it produces, whereas a colour charge is *anti*-shielded due to the presence of gluons in

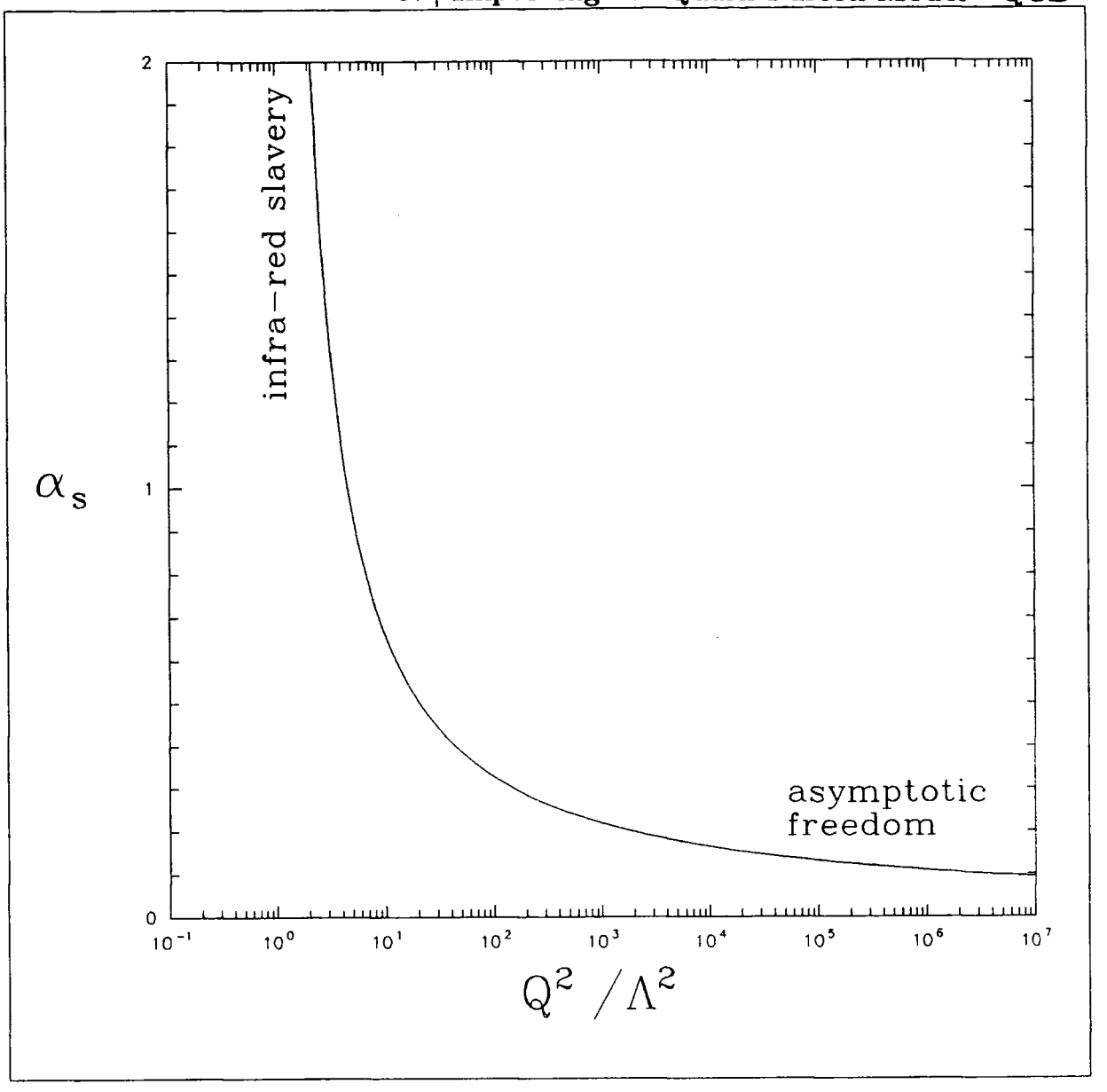

Figure 3.7 The running coupling constant of QCD in the leading logarithm approximation showing the two extreme behaviours at low and high Q^2/Λ^2.

the theory.

A remark should be made about the N_F which appears in the equation for β_0. This is to be interpreted as the number of flavours of quark which can go around the quark loops in Figure 3.6. This number depends on the energy scale and so may be equal to 3,4,5.... . Since, in (3.28), $\alpha_s(Q^2)$ is supposed to be a physical quantity and $\beta_0 \equiv \beta_0(N_F)$, we see that Λ must also depend on N_F. Thus, care must be used when quoting or interpreting values of Λ based on a

measurement of α_s at some Q^2—the number of flavours assumed must also be known (less confusion is caused, of course, if one quotes the value of $\alpha_s(Q^2)$ and Q^2).

3.5 Higher Order Calculations

Let us first briefly recap the ingredients for calculation in the leading order approximation (or, more precisely, *leading logarithm* approximation [23], [26], [27], [28]). Taking the physical structure function $F_2(x, Q^2)$, we have

$$F_2(x, Q^2)/x = \sum e_q^2 q(x, Q^2) \tag{3.31}$$

where the parton momentum distributions, $q(x, Q^2)$, obey the first-order (or one-loop) Altarelli-Parisi equations (3.17) and (3.18) in which the splitting functions are first order (one loop) (3.26),(3.27),(3.19) and the coupling constant obeys the first order (one loop) renormalization group equation (3.28) to give (3.29).

These parton distributions can now be used in the calculation, in the leading logarithm approximation, of some inclusive hadronic process $AB \to CX$. Schematically, we have

$$\sigma_{AB\to CX} = f_A^a|_{LL} \otimes \hat{\sigma}^{Born}_{ab\to cX} \otimes f_B^b|_{LL} \ . \tag{3.32}$$

In a sense, this is a formula which is not consistently 'leading logarithm' since we use just the lowest order sub-process cross-section $\hat{\sigma}^{Born}$. However, this is what is meant by leading logarithm.

Before discussing next-to-leading logarithm corrections, we will briefly discuss different types of expansions in perturbation theory. Consider a physical quantity R—a function of Q^2 and some other variables. This can be expressed as a series

$$\begin{aligned} R =& (R_0 + R_1\alpha_s + R_2\alpha_s^2 + \cdots) \\ &+ \ln\rho^2(R_1'\alpha_s + R_2'\alpha_s^2 + R_3'\alpha_s^3 + \cdots) \\ &+ \ln^2\rho^2(R_2''\alpha_s^2 + R_3''\alpha_s^3 + R_4''\alpha_s^4 + \cdots) \\ &+ \cdots \\ &+ \ln^k\rho^2(\tilde{R}_k\alpha_s^k + \tilde{R}_{k+1}\alpha_s^{k+1} + \tilde{R}_{k+2}\alpha_s^{k+2} + \cdots) \\ &+ \cdots \end{aligned} \tag{3.33}$$

where $\rho^2 = Q^2/\mu^2$. Calculating 'fixed order' corrections means rewriting this series as

$$R^{fixed\ order} = R_0 + \alpha_s(R_1 + R_1' \ln \rho^2) + \alpha_s^2(R_2 + R_2' \ln \rho^2 + R_2'' \ln^2 \rho^2) + \cdots \quad (3.34)$$

and taking the term proportional to α_s^n to be the n^{th} order. Calculating in the leading logarithm approximation means approximating (rather than rewriting) the series by retaining only those terms with the highest power of $\ln \rho^2$ for a given power of α_s viz.

$$R_{LL} \approx R_0 + \alpha_s \ln \rho^2 R_1' + \alpha_s^2 \ln^2 \rho^2 R_2'' + \cdots . \quad (3.35)$$

In this approximation, therefore, the expansion parameter is $\alpha_s \ln \rho^2$ which *is not* necessarily much less than one when $\alpha_s \ll 1$ so that successive terms do not necessarily get smaller. Thus, it is essential to sum this infinite series completely to obtain a meaningful answer. Methods for doing this are discussed in [23], [24].

The next-to-leading logarithm approximation keeps, in addition to (3.35), terms of the form $\alpha_s^n \ln^{n-1} \rho^2$

$$R_{NLL} \approx R_0 + \alpha_s(\ln \rho^2 R_1') + \alpha_s^2(\ln^2 \rho^2 R_2'' + \ln \rho^2 R_2') + \cdots \quad (3.36)$$

where, as before, it is necessary completely to sum the series. Figure 3.8 shows the structure of all these schemes.

Schematically, then, we have

$$\text{Parton Model: } F_2/x \sim q(x) \quad (3.37)$$

$$\text{LLA: } F_2/x \sim q(x, Q^2, \text{AP}[P_{LL}, \alpha_{sLL}]) \quad (3.38)$$

$$\text{NLLA: } F_2/x \sim q(x, Q^2, \text{AP}[P_{NLL}, \alpha_{sNLL}, X]) + \alpha_{sNLL} X \quad (3.39)$$

where, for example, $\text{AP}[P_{NLL}, \alpha_{sNLL}, X]$ means that the Altarelli-Parisi equations are 'functions' of the next-to-leading logarithm splitting functions, the NLL

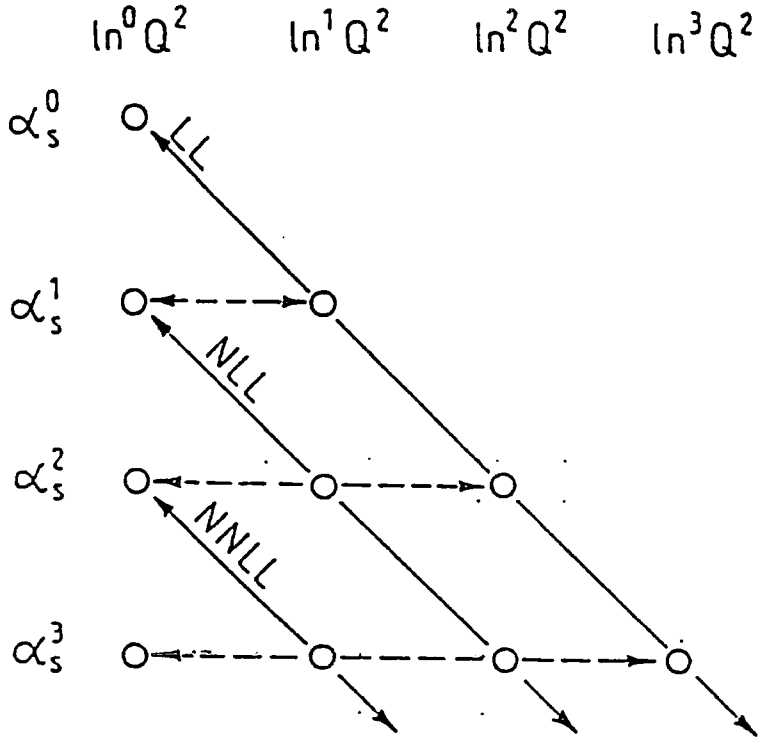

Figure 3.8 Structure of perturbative corrections. The horizontal lines show the fixed order corrections. The leading logarithmic corrections (LL) are represented by the inclined line. Lines showing the next-to-leading (NLL) and the next-to-next-to leading (NNLL) corrections are parallel to the LL line. Arrows indicate that the whole series has to be summed for LL, NLL and NNLL approximations: $\sum \alpha_s^n \ln^n Q^2$, $\sum \alpha_s^n \ln^{n-1} Q^2$, and $\sum \alpha_s^n \ln^{n-2} Q^2$ respectively.

coupling constant and X. The function X arises at NLL because there is some arbitrariness in the renormalization and factorization procedures: different X's characterize different schemes. In the DIS ('deep-inelastic scattering') scheme, X is identically zero, thus retaining the QPM and LLA relationship between F_2—the most commonly measured structure function in deep-inelastic scattering—and the q_i. In the $\overline{\text{MS}}$ ('modified minimal subtraction') scheme, X is not identically zero. (This scheme is defined by the way it subtracts the poles and some other (finite) terms which occur in the calculational method of 'dimensional regularization'). In addition, this scheme has the advantage of being simple to generalize

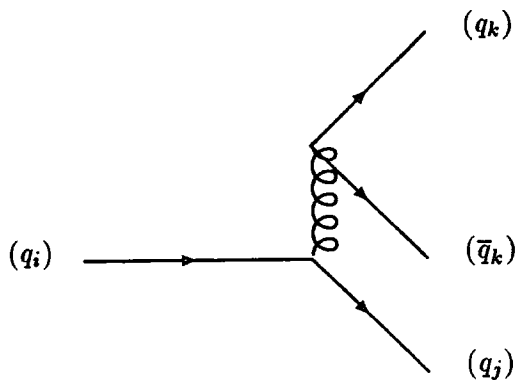

Figure 3.9 A higher-order splitting function.

to all orders of perturbation theory. The relationship between the quark distributions in the two schemes is

$$q^{\overline{\mathrm{MS}}}(x,Q^2) = \int_x^1 \frac{dz}{z}\left[\delta(1-z) - \frac{\alpha_s(\mu^2)}{2\pi} f_q(z) q^{\mathrm{DIS}}(x/z,Q^2) - \frac{\alpha_s(\mu^2)}{2\pi} f_g(z) g^{\mathrm{DIS}}(x/z,Q^2)\right] \tag{3.40}$$

where f_q and f_g are known functions (q.v. [29], [30]).

As an example of the increased complexity of the splitting functions, we take P_{qq} as an example. We find that the transition from leading logarithm to next-to-leading logarithm is

$$q_i P_{qq} \longrightarrow \sum_j [q_j \tilde{P}_{q_i q_j} + \overline{q}_j \tilde{P}_{q_i \overline{q}_j}] \tag{3.41}$$

(where the arguments have been suppressed for clarity). This is because, at leading logarithm, a quark could only split into a quark of the same flavour. At NLL, however, with *two* quark-gluon vertices, a quark can split into a quark or antiquark of any flavour (see Figure 3.9). Full expressions for the splitting functions $\tilde{P}$ are given in [26], [27], [28].

3.6 Approximations to $\alpha_s(Q^2)$

In the leading logarithm (one loop) approximation to $\alpha_s(Q^2)$, we consider *all* one-loop corrections to the quark-gluon coupling (see Figure 3.6) and obtain

$$\alpha_s(Q^2) = \alpha_s(\mu^2)(1 - \frac{\beta_0}{4\pi}\alpha_s(\mu^2)\ln(Q^2/\mu^2) + \cdots + \left[-\frac{\beta_0}{4\pi}\alpha_s(\mu^2)\ln(Q^2/\mu^2)\right]^k \cdots \tag{3.42}$$

which is trivial to sum since it is a geometric progression with successive terms in the ratio $-\beta_0\alpha_s(\mu^2)\ln(Q^2/\mu^2)/4\pi$:

$$\alpha_s(Q^2) = \frac{\alpha_s(\mu^2)}{1 + \frac{\beta_0}{4\pi}\alpha_s(\mu^2)\ln(Q^2/\mu^2)} \tag{3.43}$$

or

$$-\frac{\beta_0}{4\pi}\ln Q^2 + \frac{1}{\alpha_s(Q^2)} = -\frac{\beta_0}{4\pi}\ln\mu^2 + \frac{1}{\alpha_s(\mu^2)} = -\frac{\beta_0}{4\pi}\ln\Lambda^2 \tag{3.44}$$

where both sides have been equated to a constant, $-\beta_0 \ln\Lambda^2/4\pi$, since μ^2 and Q^2 are independent. Hence,

$$\alpha_{sLL}(Q^2) = \frac{4\pi}{\beta_0 \ln(Q^2/\Lambda^2)} \,. \tag{3.45}$$

The extension to next-to-leading logarithm goes along similar lines. In fact, as we have mentioned in (3.28) $\alpha_{sLL}(Q^2)$ is the solution of the ordinary differential equation

$$\frac{d\alpha_s(Q^2)}{d\ln Q^2} = -\alpha_s(Q^2)^2.\frac{\beta_0}{4\pi} \tag{3.46}$$

as can readily be seen by differentiating (3.45) . The summation of the next-to-leading logarithms is effectively done by solving an extension of this

$$\frac{d\alpha_s(Q^2)}{d\ln Q^2} = -\frac{\alpha_s(Q^2)^2}{4\pi}\left(\beta_0 + \beta_1\frac{\alpha_s(Q^2)}{4\pi}\right) \tag{3.47}$$

where β_1 is another calculable loop function to get (approximately)

$$\alpha_{sNLL}(Q^2) = \frac{4\pi}{\beta_0 \ln(Q^2/\Lambda^2)}\left(1 - \frac{\beta_1}{\beta_0^2}\frac{\ln\ln(Q^2/\Lambda^2)}{\ln(Q^2/\Lambda^2}\right) \,. \tag{3.48}$$

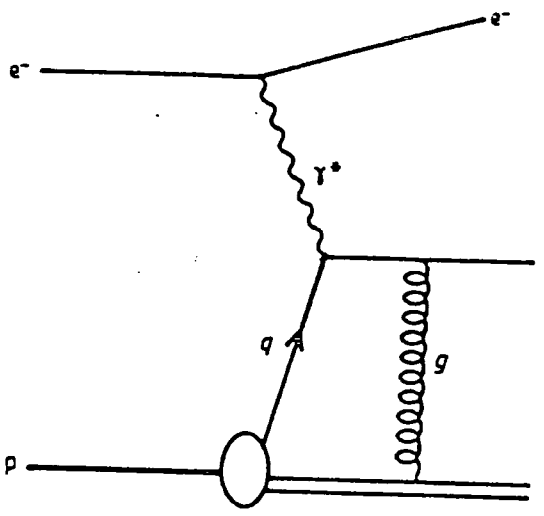

Figure 3.10 An example of an interaction between the scattered quark and the spectator partons responsible for higher-twist corrections to physical structure functions calculated in perturbative QCD.

3.7 Higher Twist Effects

There is another problem with this analysis: that of so-called 'higher-twist' effects (the name coming from the terminology of the operator-product expansion). The theory outlined above does not include Feynman diagrams in which there are interactions between the scattered quark and the spectator partons, an example of which is shown in Figure 3.10. The physical structure functions, F, are really a power series expansion in $1/Q^2$ viz.

$$F_{phys} = F_{(0)} + \frac{F_{(1)}}{Q^2} + \frac{F_{(2)}}{Q^4} + \cdots \tag{3.49}$$

where the higher order terms originate from increasingly convoluted diagrams.

We can lessen the effects of our non-inclusion of the higher-twist terms by using only the structure function data with $Q^2 > Q^2_{cut}$ since at higher values of Q^2 the physical structure function is dominated by the lowest-twist term. The difficulty with this is an obvious one— what is Q^2_{cut} such that $F_{(1)}/Q^2_{cut} \ll F_{(0)}$? To answer this question necessitates the calculation of the higher-twist diagrams to see how big $F_{(1)}$ is. Alternatively, the size of the corrections needed can

be estimated by performing fits to data with the physical structure function parametrized as

$$F_{phys} = F_{(0)}\left(1 + \frac{C(x)}{Q^2}\right) \tag{3.50}$$

where $C(x)$ is fitted as a free parameter in each x bin. Fits of this kind have recently been performed by Milsztajn [31] with the conclusion that the corrections are negligible for $x \lesssim 0.5$ where $C(x) \approx 0$ and that $C(x)$ grows, linearly within the accuracy of the analysis, from approximately zero at $x \approx 0.5$ to around 1 GeV^2 at $x = 0.75$.

3.8 The Longitudinal Structure Function, F_L

In equation (2.26), we saw that the F_1 and F_2 structure functions are simply related in the Parton Model. We rewrite that equation here as

$$F_2(x) - 2xF_1(x) \equiv F_L(x) = 0 \tag{3.51}$$

in order to define the longitudinal structure function, F_L, which is related to the absorption cross-section for longitudinally-polarized virtual photons. Equation (3.51) holds true provided the quark interacting with the virtual photon has no transverse momentum but, as we have seen in §3.2, in QCD there is the possibility of the quark acquiring some by radiating a gluon. In the $\overline{\text{MS}}$ scheme, it can be shown that

$$F_L(x,Q^2) = \frac{\alpha_s(Q^2)}{\pi} \cdot \left[\frac{4}{3}\int_x^1 \frac{dy}{y}\frac{x^2}{y}F_2(y,Q^2) + 2\sum_{q=u,d,s,c,..} e_q^2 \int_x^1 \frac{dy}{y}\frac{x^2}{y}(1-\frac{x}{y})yg(y,Q^2)\right] . \tag{3.52}$$

This structure function is usually discussed in terms of the quantity

$$R(x,Q^2) \equiv \frac{F_2(x,Q^2) - 2xF_1(x,Q^2)}{2xF_1(x,Q^2)} . \tag{3.53}$$

4. The Deep-Inelastic Scattering Data

4.1 Introduction

Here, we discuss the deep-inelastic scattering data that we need. We have used data on $F_2^{\mu p}$, $F_2^{\mu n}/F_2^{\mu p}$, $F_2^{\nu Fe}$, and $xF_3^{\nu Fe}$ where the data produced using an iron target have been corrected to those produced using deuterium. These correspond, in the leading-logarithm approximation,* to the quark combinations (as shown in §2.3 and §2.5):

$$F_2^{\mu p} = (4u_V + d_V + 10\overline{u} + 2\overline{s} + 8\overline{c})/9 \tag{4.1}$$

$$F_2^{\mu n} = (u_V + 4d_V + 10\overline{u} + 2\overline{s} + 8\overline{c})/9 \tag{4.2}$$

$$F_2^{\nu d} = u_V + d_V + 4\overline{u} + 2\overline{s} + 2\overline{c} \tag{4.3}$$

$$xF_3^{\nu d} = u_V + d_V \tag{4.4}$$

(the arguments (x, Q^2) have been omitted for clarity) where we have assumed $\overline{d} \equiv \overline{u}$. Thus, naïvely speaking, we see that at a given (x, Q^2) point within the common kinematic range of the data, we are unable to determine the independent quantities $u_V, d_V, \overline{u}, \overline{s}$ and $\overline{c}$ because we have four equations in five unknowns. We say 'naïvely' because, in our fitting, we do not make a point-by-point determination of $u_V, d_V, \overline{u}, \overline{s}$ and $\overline{c}$—as explained in Chapter 5, we vary the parameters describing these quantities at Q_0^2 and, for each combination of the parameters, we use the Altarelli-Parisi evolution equations to generate their values at higher Q^2 (so the five quantities are not, in fact, independent if we assume QCD). Let us discuss each type of data set in turn:

$\star$ in the next-to-leading logarithm approximation, the quark distributions must be convoluted with the appropriate coefficient functions as shown in §3.5

4.2 $F_2^{\mu p}$ DATA

We use the $F_2^{\mu p}$ data of both the EMC [32] and BCDMS [16] collaborations produced using a hydrogen target. Both of these data sets were produced in experiments using the same muon beam at the same time, the BCDMS experiment being the further 'downstream'. The BCDMS experiment collected 1.8×10^6 events (after cuts) of deep-inelastic scattering of muons on a hydrogen target at four different beam energies (E =100, 120, 200 and 280 GeV). This enabled them to estimate R (see §3.8) by extracting the F_2's of the four beam energies in each x bin from

$$\frac{d^2\sigma}{dxdQ^2} = \frac{4\pi\alpha^2}{Q^4 x}\left(1 - y - \frac{Q^2}{4E^2} + \frac{y^2E^2 + Q^2}{2E^2(R+1)}\right)F_2 \tag{4.5}$$

assuming trial values of R (which was assumed to be independent of Q^2—a reasonable approximation). The value of $R \equiv R(x)$ chosen as the experimental result was then taken to be the trial value which made the extracted F_2's as near independent of E as possible.

The kinematic range of the data is $0.06 \leq x \leq 0.80$ and $7\ \text{GeV}^2 \leq Q^2 \leq 260\ \text{GeV}^2$. The collaboration's own analysis of their results finds that R is compatible with R_{QCD} and so their published values of F_2 assume $R = R_{\text{QCD}}$. Furthermore, the systematic errors are comparable in size to the statistical errors. In using this data set, we impose the x-dependent Q^2 and $y = Q^2/2M_P Ex$ cuts specified in [16] on the data from each beam energy and then merge together the data at the four (consistent) beam energies, finally adding the statistical and systematic errors in quadrature. The overall normalization uncertainty of these data is estimated to be 3%.

The EMC experiment was performed similarly. The four beam energies used were E = 120, 200, 240 and 280 GeV. For these data, though, a value of $R = 0$ (the Parton Model prediction) was assumed to extract the F_2 structure function from the measured differential cross-section. The kinematic range of these data is $0.03 \leq x \leq 0.80$ and $3.5\ \text{GeV}^2 \leq Q^2 \leq 170\ \text{GeV}^2$. A data set consisting of the merged F_2 values from the four beam energies was produced by the collaboration itself and this is the data set that we use. The errors on these F_2 values are significantly larger than those on the corresponding BCDMS values—typically

three times as great. The estimated overall normalization uncertainty on these data is 5%.

To put the EMC and BCDMS $F_2^{\mu p}$ data sets on an equal footing, we should correct one of the sets to the value of R used by the other. Since the BCDMS analysis favoured a value consistent with R_{QCD} over $R = 0$—which the EMC analysis *assumed*—we should correct the EMC data. This is difficult to do because of the complexity of the procedure EMC used to merge the data from the four beam energies. However, the correction is small (compared to the experimental errors) over the whole kinematic range and only becomes non-negligible for $x < 0.20$ at high Q^2 [33]. Therefore, we do not correct the EMC data for this small effect because it is insignificant compared to the experimental errors and the overall normalization uncertainty.

It was obviously hoped that these two experiments would give consistent results, effectively cross-checking one another. Unfortunately, this is not the case. Figure 4.1 shows the disagreement between the data sets in a concise way—displaying the Q^2-averaged ratio $F_2^{\mathrm{EMC}}/F_2^{\mathrm{BCDMS}}$ as a function of x. From this, it is evident that there is no global, relative renormalization of the data sets which would render them consistent. Recently, however, a re-analysis [34] of low-Q^2 F_2^{ep} measurements made at SLAC, which extends them to higher Q^2 (such that there is some overlap with the EMC and BCDMS data), has provided something against which to compare the later measurements. Figure 4.2 (taken from [34]) shows the SLAC, EMC and BCDMS hydrogen ((a) and (b)) and deuterium ((c) and (d)) target data after the most favourable renormalizations of the EMC and BCDMS data have been applied ('favourable' in the sense of minimizing the χ^2 of a parametrization of F_2 to the combined SLAC-EMC or SLAC-BCDMS data). For the hydrogen target data, these renormalizations are of +8% for the EMC data and -2% for the BCDMS data (the corresponding numbers for the deuterium data are +8% and -1%). The EMC data are now consistent with the SLAC data at all x and, in fact, a renormalization of about 8% had been found necessary by the collaboration itself in order to obtain consistency between their $F_2^{\mu d}$ data at low x and low Q^2. It has also been noted by Martin, Roberts and Stirling (MRS) [35] who required a relative renormalization between the EMC $F_2^{\mu p}$ data and the neutrino scattering data of CDHSW [36] and CCFRR [37] of about 10%

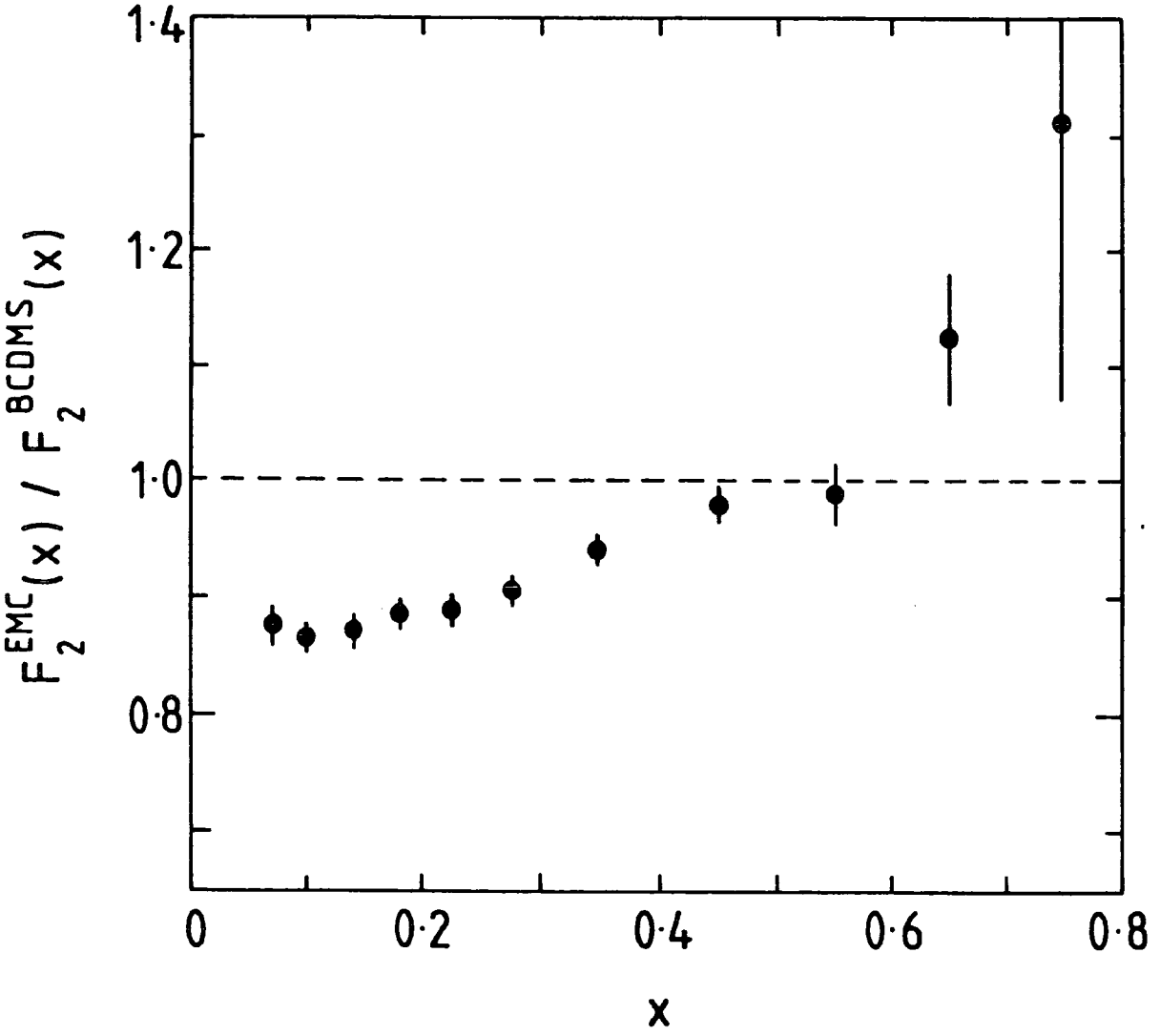

Figure 4.1 The (Q^2-averaged) ratio of the $F_2^{\mu p}$ structure functions measured by EMC [32] and BCDMS [16], from reference [16].

for consistency. Therefore, we perform this renormalization on the data we use in our analysis.

The BCDMS data, however, cannot be globally renormalized to match the SLAC data. Without renormalization, the BCDMS data are a few percent too high at low x whilst at high x, they are too low, although there is good agreement in the intermediate range. We choose to renormalize the BCDMS data down by 2% aiding the agreement at low x. We then attribute the blame for the poor

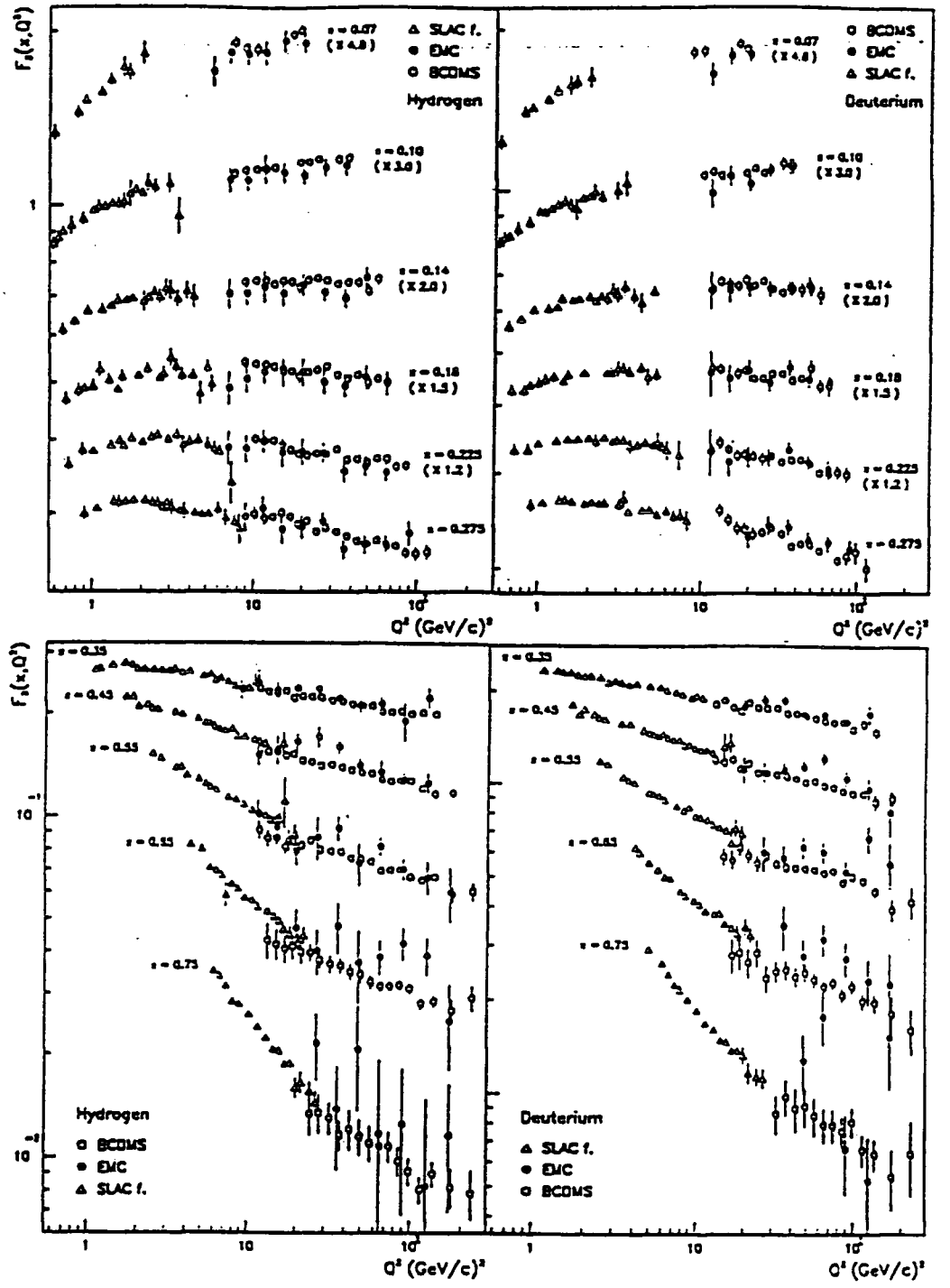

Figure 4.2 Comparison of the re-analysed SLAC [38], BCDMS [16], [39] (with the hydrogen (deuterium) target data renormalized downwards by 2%(1%)), and EMC [32], [40] (hydrogen and deuterium target data both renormalized upwards by 8%) measurements of F_2.

match at high x to the large systematic errors on the high-x, low-Q^2 BCDMS

data. In any case, we do not use this region of the data because of the cuts we make in order to lessen the impact of higher-twist processes (see §4.5).

Thus, we have made a relative renormalization of 10% between the EMC and BCDMS $F_2^{\mu p}$ data sets. As previously mentioned though, this cannot make them consistent with each other. Rather than make an arbitrary choice to use just one 'favoured' data set, we perform our full analyses twice—once with the EMC data and once with the BCDMS data.

4.3 $F_2^{\nu Fe}$ AND $xF_3^{\nu Fe}$ DATA

For these structure functions, we use the high-statistics data of the CDHSW collaboration [36]. These data are based on 4.3×10^6 ν–Fe events and 5.4×10^6 $\overline{\nu}$–Fe events. The structure functions used are the average of $F_i^{\nu Fe}$ and $F_i^{\overline{\nu} Fe}$ and are corrected to remove contributions from higher-order electroweak processes and for the non-isoscalarity of the iron target. CDHSW use a method of extracting F_2 whereby the uncertainty introduced by the unknown R is certainly less than the combined statistical and systematic errors.

The most important correction that we apply to this data is for the so-called EMC effect. This is a phenomenon discovered by that collaboration in a comparison of its F_2 data measured on several different nuclei. They found that there is a significant difference between the values of F_2^N $(= 1/2(F_2^p + F_2^n))$ measured on heavy nuclei and those measured on deuterium. We have taken a compilation of all $F_2^{\text{heavy}}(x)/F_2^d(x)$ data and fitted a functional form (see Figure 4.3):

$$\frac{F_2^{\text{heavy}}}{F_2^d} = \begin{cases} 1.23 + 0.2 \log_{10} x & \text{for } x < 0.11 \\ 1.04 & \text{for } 0.11 \leq x \leq 0.24 \\ 0.79 - 0.4 \log_{10} x & \text{for } x > 0.24 \,. \end{cases} \tag{4.6}$$

We then correct the CDHSW $F_i^{\nu Fe}$ structure functions to equivalent deuterium ones by dividing them by this function (assuming, therefore, that $xF_3^{\nu Fe}$ can be corrected in the same way as $F_2^{\nu Fe}$).

We did not renormalize these data. As has already been mentioned, Martin *et al.* found it necessary to apply a relative renormalization between the EMC F_2^p data and the CDHSW and CCFRR neutrino data of about 10%. As we have

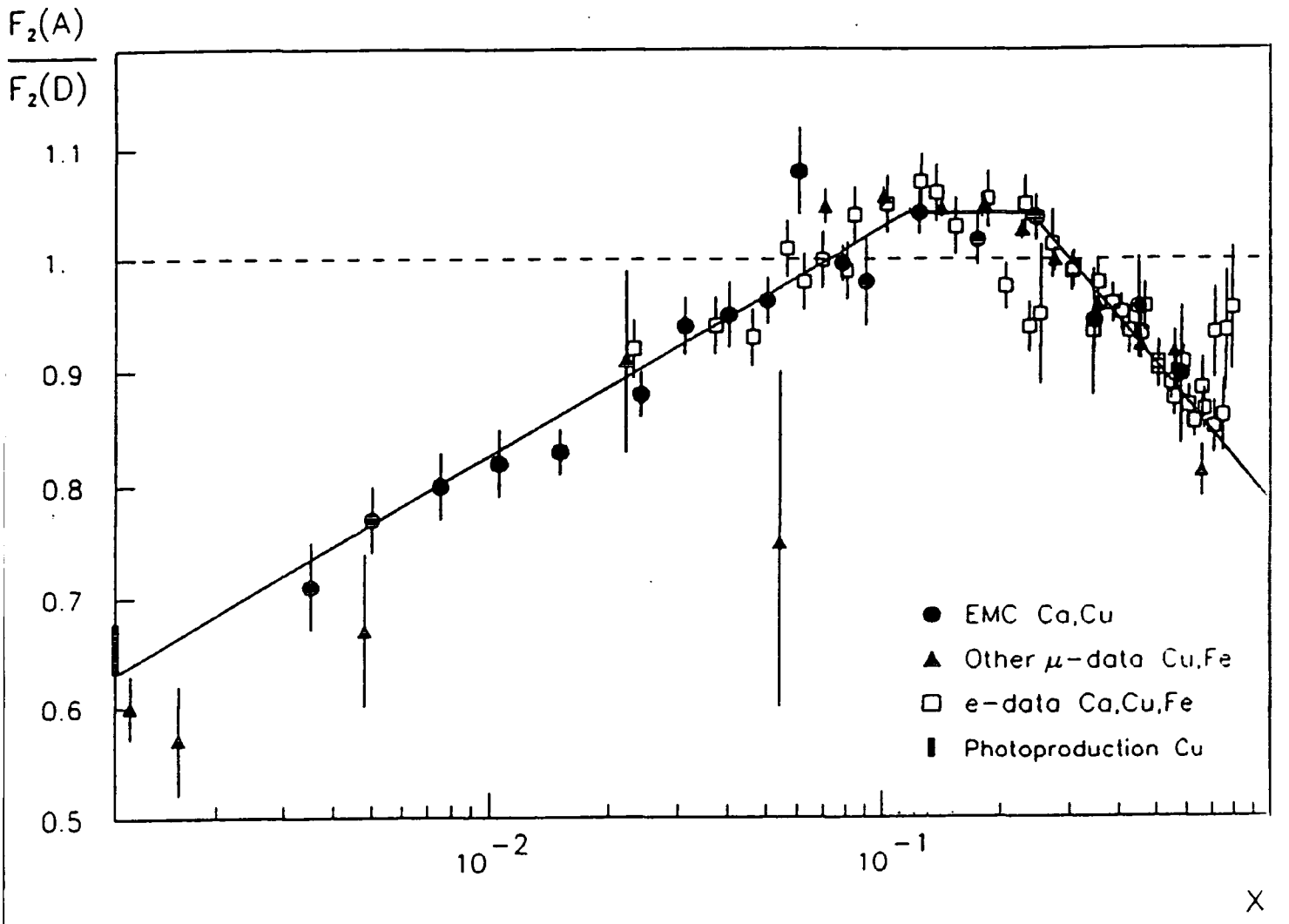

Figure 4.3 Compilation of data showing the discrepancy between F_2^ν as measured using heavy-nucleus targets and that using deuterium. The line drawn through the data is the function given in Equation (4.6).

decided on renormalizing the EMC data upwards by 8%, these neutrino data will be consistent with the EMC data to a large degree. In fact, we find that when we take our final parton distributions (see Chapter 8) and refit all the deep-inelastic

scattering data with the $F_2^{\mu p}$ and CDHSW data normalizations (only) as free parameters, the optimum values of these parameters (with respect to the total χ^2) are within 1/2% of the values we chose. Obviously, part of the reason for this is that the other parameters are 'biased' towards these values, but this fact does lend some support to our choices.

Previous analyses (by MRS [35], [41]) have also used the $F_2^{\nu Fe}$ and $xF_3^{\nu Fe}$ data of the CCFRR collaboration. We have not because these data are largely consistent with those of CDHSW but have much greater errors, giving them little rôle in the determination of the parton momentum distributions.

4.4 $F_2^{\mu n}/F_2^{\mu p}$ DATA

We have used measurements of $F_2^{\mu n}/F_2^{\mu p}$produced by EMC [40], BCDMS [42], and NMC [43]. These data are obtained by placing targets of hydrogen and deuterium in the same muon beam. This substantially reduces many sources of systematic error—in particular, the overall normalization—because these cancel in the ratio. Assuming that R is the same for protons and deuterons, the ratio of the structure functions is given simply by

$$\frac{F_2^n}{F_2^p} = \frac{\sigma^{\mu d}}{\sigma^{\mu p}} - 1 \,. \tag{4.7}$$

Because of the absence of an overall normalization uncertainty for these data, we can have particular confidence in them. Thus, we are especially keen for our parton momentum distributions to fit them well.

From Equations (4.1) and (4.2), we see that (neglecting charm and with $2\overline{s} = \overline{u} = \overline{d}^{\star}$ which is a good approximation at the low Q^2 of these data)

$$\frac{F_2^n}{F_2^p} = \frac{u_V + 4d_V + 11\overline{u}}{4u_V + d_V + 11\overline{u}} \tag{4.8}$$

giving the expected asymptotic behaviour

$$\frac{F_2^n}{F_2^p} \longrightarrow \begin{cases} 1 & \text{as } x \to 0 \\ \frac{1}{4} & \text{as } x \to 1 \end{cases} \tag{4.9}$$

where the first limit assumes that the sea quarks dominate at low x and the

$\star$ This assumption is motivated in §5.2 but is not important for this argument: SU(3) flavour symmetry, $\overline{s} = \overline{u} = \overline{d}$ yields the same results.

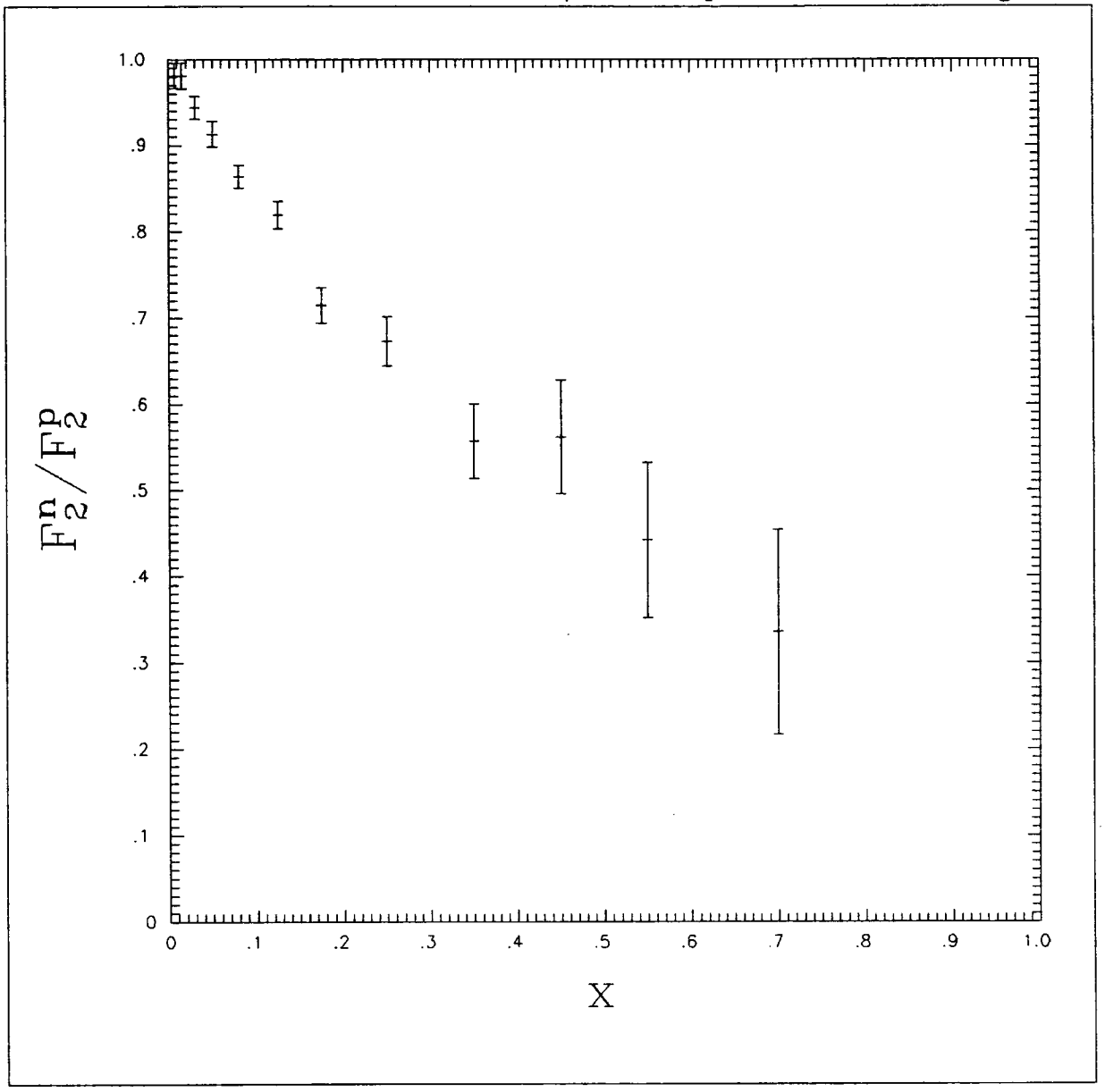

Figure 4.4 Data on the structure function $F_2^{\mu n}/F_2^{\mu p}$ from the NMC [43]. The errors shown are the statistical and systematic errors, added in quadrature.

second limit assumes that $d_V/u_V \to 0$ as $x \to 1$. As can be seen from Figure 4.4, this is well borne out by the data (and the alternative—$F_2^{\mu n}/F_2^{\mu p} \to 4$ as $x \to 1$—is certainly ruled out). Thus, we enforce $d_V/u_V \to 0$ as $x \to 1$ in our fits.

4.5 ALL DATA

To all of these deep-inelastic scattering data we perform some global cuts. Recalling the discussion in §3.7 on higher-twist effects, we can see (for $x > 0.5$) that these might make a contribution of over 5% for $4(x - 0.5)/Q^2 > 0.05$, that is, $Q^2 < 80(x - 0.5)$ (where Q^2 is in GeV^2). Thus, we require Q^2 cuts $Q^2_{min}(x)$ of 4 GeV^2 (0.55), 12 GeV^2 (0.65) and 20 GeV^2 (0.75). For this reason, we impose a cut on the invariant mass of the debris of the inelastic collision, $W^2 = Q^2(1 - x)/x + M_P^2$ (see (2.12)), of $W^2 > 10$ GeV^2 . This gives us x-dependent Q^2 cuts of 11 GeV^2 (0.55), 17 GeV^2 (0.65) and 27 GeV^2 (0.75)—keeping higher-twist effects well below 5% in the kinematic regions where they may occur. We also impose a global Q^2 cut of $Q^2 > 5$ GeV^2 and an x cut of $x > 0.05$. Both of these help to eliminate data in the kinematic region where differences in the values of R (discussed in §3.8) used by the collaborations to extract the physical structure functions are greatest.

5. Parton Distributions from DIS data

5.1 Method for Extracting the Parton Distributions

How are we to determine the parton distribution functions given the experimentally measured physical structure functions? Schematically, from Section 4.1, we have

$$F(x,Q^2) = \sum_p xp(x,Q^2) \tag{5.1}$$

where p represents some parton distribution function. Alternatively, inverting the equations, we have

$$xp(x,Q^2) = \sum_F F(x,Q^2) \; . \tag{5.2}$$

The most direct approach might seem to be to use the latter of these equations at each (experimental) (x^*,Q^{2*}) point and hence determine the parton distribution functions at that point

$$x^*p(x^*,Q^{2*}) = \sum_F F(x^*,Q^{2*}) = A \pm \epsilon_A \tag{5.3}$$

where ϵ_A is the experimental error from statistical and systematic uncertainties and normalization uncertainty. This approach has many difficulties. The physical structure function data exist only at a discrete set of (x,Q^2) points and so the resulting parton distribution functions would only be determined at those points on each parton distribution function surface. Furthermore, there would be an error associated with each point. This would not give a very useful set of parton distribution functions! In addition, we must remember that this analysis is being carried out *using* QCD and that it is not supposed to be a test of it: in QCD the Q^2 evolution of the parton distribution function at some (x_1,Q_1^2) is determined via the Altarelli-Parisi equations by the parton distribution functions at all $x > x_1, Q^2 \leq Q_1^2$ (and by $\Lambda_{\rm QCD}$). This is difficult to incorporate into this method. Another problem is that of using several data sets of physical structure functions. In general, each of these has its own overall normalization uncertainty which would lead to (infinitely!) many alternative parton distribution function surfaces: one for each combination of the normalizations.

Thus we are forced to abandon this method as impractical. Instead, we must use

$$F(x,Q^2) = \sum_p xp(x,Q^2) \tag{5.4}$$

and proceed as follows. We construct trial sets of $xp(x,Q^2)$ covering the whole range of (x,Q^2) of the data, *using* QCD via the Altarelli-Parisi equations . We then use these to construct theoretical (i.e. trial) 'physical' structure functions and compare these, using an appropriate measure of 'goodness of fit', with the experimental physical structure functions. Optimization with respect to the measure of goodness of fit then leads to a set of parton distribution functions which best describes the data. This method has none of the drawbacks of the previous one: the resulting parton distribution functions cover the entire (x,Q^2) range of the data (and beyond); the experimental errors are used in the determination of the goodness of fit by giving more weight to points with smaller errors; QCD is input from the beginning; and the normalization of different data sets can be made parameters of the fit.

This method, however, does have a drawback of its own: to start off the Altarelli-Parisi evolution of the parton distribution functions, these must be parametrized *a priori* at some initial value $Q^2 = Q_0^2$ which inevitably leads to a restriction on their possible forms (note: the Altarelli-Parisi equations describe only the Q^2 evolution of the x-dependence of the parton distribution functions). Nevertheless, we can use QCD to guide us in the asymptotic regions of $x \to 0$ and $x \to 1$, choose suitable functions which mimic this behaviour, and experiment with modified forms of these functions so that we obtain satisfactory fits to the data with the minimum number of parameters.

5.2 Parametrization of the Parton Distributions

Now we are ready to see how precisely a set of parton distribution functions can be determined using all the deep-inelastic scattering data at our disposal. We must first decide on a value of Q_0^2 at which to parametrize the functions. This value ought to be lower than any Q^2 at which we would like to use the functions for two reasons: Q^2 evolution towards higher Q^2 always eliminates fine structure in the functions so it is reasonable to assume that 'backwards

evolution' (i.e. towards lower Q^2 will be inherently unstable, especially under the influence of numerical uncertainties such as rounding errors) perhaps giving rise to spurious features in the functions; and, as a practical consideration, some complex evolution programs may be unable to run 'backwards' for a variety of reasons. A common choice has been $Q_0^2 = 4$ GeV^2 and so, for ease of comparison between our new functions and previous ones, there seems to be no good reason not to use this same value.

Next, we must decide on the parametrization of the functions at Q_0^2. Clearly, the more free parameters we have in our functions, the better will we be able accurately to reproduce the deep-inelastic data. So why should we not use 100-th order polynomials, for example? Apart from the enormous amount of computing time that would be necessary to minimize our 'goodness of fit' criterion with respect to so many free parameters, we do not want so much flexibility in our parametrization that we even fit the statistical fluctuations in the data: our theoretical predictions of the physical structure functions ought to be reasonably smooth curves through the experimental data and not ones that attempt to fit obviously anomalous data points. In practice, we should stop introducing new parameters when the payoff, in terms of a better 'goodness of fit', becomes insignificant. In addition, there are theoretical reasons to suppose that we know the form of these functions in various kinematic regions viz. at high and low x and Q^2. For example: there are 'counting rules' [44], [45], [46], [47] which propose that

$$f_i(x) \underset{x \to 1}{\longrightarrow} (1-x)^{2N_S-1} \tag{5.5}$$

where N_S is the number of 'spectator' valence quarks (i.e. those that do not take part in the scattering); and Regge theory predicts that the small-x behaviour is determined by the intercept, ζ, of the appropriate Regge exchange trajectory,

$$f_i(x) \underset{x \to 0}{\longrightarrow} x^{-\zeta} \tag{5.6}$$

where $\zeta_{gluon} = \zeta_{\overline{q}} = 1$ and $\zeta_{q_V} = 1/2$. Our parametrization reflects these ideas with its incorporation of powers of $(1-x)$ and x although we leave the exponents to be decided by the data: we do not want to be unduly influenced by unnecessary

theoretical prejudices. Thus, at $Q^2 = Q_0^2 = 4$ GeV^2 we take

$$\begin{aligned} x[u_V + d_V] &= A_{ud}\, x^{\eta_1}(1-x)^{\eta_2}\,(1+\gamma_{ud}\, x) \\ x d_V &= A_d\, x^{\eta_3}(1-x)^{\eta_4}\,(1+\gamma_d\, x) \\ x\text{'Sea'} = 2x[\overline{u}+\overline{d}+\overline{s}] &= A_S\, x^{\delta_S}\,(1-x)^{\eta_S} \\ x g &= A_g\,(1-x)^{\eta_g} \\ x c &= 0\ . \end{aligned} \tag{5.7}$$

Points to note in this parametrization are

i) the use of $x(u_V + d_V)$ and $x d_V$ as the two independent functions of the valence quarks. The reason we do this is essentially historical. The computer program we use is set up to work in this manner mainly because it simplifies the analysis of $xF_3^{\nu d}$ which, as we have seen, is simply $x(u_V + d_V)$

ii) A_{ud} and A_d are not variables parameters of the fit but are coefficients calculated so that sum rules which ensure that the sum over all x of $u - \overline{u}$ is 2 and of $d - \overline{d}$ is 1:

$$\begin{aligned} \int_0^1 (u_V + d_V)dx &= 3 \\ \int_0^1 d_V dx &= 1 \end{aligned} \tag{5.8}$$

assuming that, at some Q^2, the proton consists of two u quarks and one d quark, this is simply an enforcement of baryon number conservation. The integrals (5.8) are easily performed analytically in terms of the Beta function, B

$$B(a+1, b+1) \equiv \int_0^1 x^a (1-x)^b dx \equiv \frac{\Gamma(a+1)\Gamma(b+1)}{\Gamma(a+1+b+1)}\ . \tag{5.9}$$

iii) A_g is calculated so that the total momentum sum rule

$$\int_0^1 x(u_V + d_V + \text{'Sea'} + g) = 1 \tag{5.10}$$

is obeyed. This reduces our total number of degrees of freedom by one.

iv) xg has only two free parameters because the deep-inelastic data are fairly insensitive to the form of the gluon distribution (although not *completely* at next-to-leading order in the $\overline{\rm MS}$ scheme)—in fact, even after we have considered prompt photon data, which we consider to be sensitive to the gluon distribution, we are still not justified in having more freedom (see §6.3).

v) the distribution of the charm quarks is set equal to zero at $Q^2 = Q_0^2$. We assume the charm quark to be massless and thus charm quarks are generated by the evolution for $Q^2 > Q_0^2$. The charm structure function, $F_2^{c\bar{c}}$ [48], is well described by using this procedure, as shown by MRS in [49].

vi) We assume the composition of the sea to be

$$\overline{u} = \overline{d} = 2\overline{s} \tag{5.11}$$

at Q_0^2. The justification for this is that a recent experiment by the CCFR collaboration [50] has produced an estimate of the ratio of the momentum carried by s and $\overline{s}$ quarks to that carried by the other sea quarks, $\overline{u}$ and $\overline{d}$. The experiment is based on observations of opposite-sign dimuons in the process $\nu_\mu(\text{or } \overline{\nu}_\mu)N \rightarrow \mu^+\mu^- X$ (Figure 5.1). The s-quark distribution was assumed to be of the form

$$x\overline{s}(x) = xs(x) = S_0(1+\beta)(1-x)^\beta \tag{5.12}$$

where β was fitted to be 4.8 ± 1.0 and they found that

$$\int_0^1 dx x(s(x) + \overline{s}(x)) = [0.44^{+0.11}_{-0.07}] \int_0^1 dx x(\overline{u}(x) + \overline{d}(x)) \; . \tag{5.13}$$

Thus, if we are to make the assumption that $\overline{s}/\overline{u} = \eta$ at Q_0^2, then $\eta = 1/2$ seems reasonable.

vii) γ_{ud} and γ_d must never be allowed to be less than -1 as this would make the valence quark distributions negative for $x > -1/\gamma$.

We thus have 10 degrees of freedom describing the Q_0^2 shape of the parton distributions. In addition, we have another parameter, $\Lambda_{\overline{\rm MS}}$, which is directly

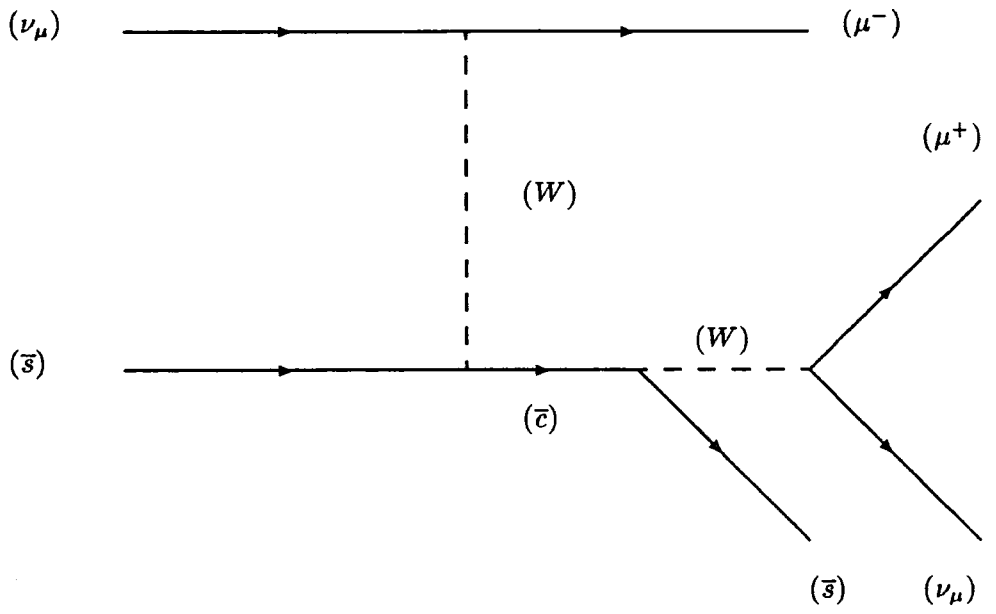

Figure 5.1 Opposite-sign dimuon production.

correlated with the rate of Q^2 evolution, since

$$\frac{\partial(q,g)}{\partial \ln Q^2} \propto \alpha_s(Q^2) \tag{5.14}$$

and

$$\alpha_s(Q^2) \sim \frac{1}{\ln(Q^2/\Lambda^2_{\overline{\rm MS}})}, \tag{5.15}$$

making a total of eleven degrees of freedom in all.

5.3 Minimization Procedure

With such a large dimensional parameter space to search, it is important to start the minimization procedure at a point reasonably close to an acceptable minimum (no algorithm exists which can guarantee to find a global minimum and there will, almost certainly, be numerous local minima). As we are using a parametrization consistent with that of the MRS sets, this allows us to use, as one guess, the parametrizations of the latest of those sets (MRSE′ and MRSB′ [41]) as a starting point (note that we are not merely reproducing that work since most of the data has been revised and we shall eventually be incorporating prompt photon

production data and Drell-Yan process data in a different, more systematic way). Ideally, we should like to allow all 11 parameters to be free in the minimization, whilst endeavouring to stay in roughly the same region of parameter space, thus producing optimum values of all the parameters. With hindsight, and from the results of previous studies, we know that this is not sensible because of the strong correlations between specific subsets of the parameters. In this study, we shall concentrate on the most important of these correlations: that between $\Lambda_{\overline{\rm MS}}$ and η_g. Both of these parameters have the same effect on the rate of evolution of sea quarks as can readily be seen from the Altarelli-Parisi equation:

$$\frac{\partial q}{\partial \ln Q^2} \sim \frac{1}{\ln(Q^2/\Lambda^2_{\overline{\rm MS}})}(P_{qq} \otimes q + P_{qg} \otimes g) \; . \tag{5.16}$$

Increasing the gluon distribution increases the rate of evolution of quarks (the $P_{qg} \otimes g$ term being always positive), as does increasing $\Lambda_{\overline{\rm MS}}$ (of course, this rough qualitative argument doesn't *prove* that the $\Lambda_{\overline{\rm MS}} - \eta_g$ correlation will be particularly marked). Deep-inelastic scattering data may well be satisfied with a whole range of different pairs of $\Lambda_{\overline{\rm MS}}$ and η_g but many other processes will not. Thus, in order to investigate the severity of this correlation, we must perform fits to the data for a whole range of fixed $\Lambda_{\overline{\rm MS}} - \eta_g$ pairs of values.

Next, we come to the question of the 'goodness of fit' criterion. The appropriate measure to use is χ^2 = (Theory-Data)^2/ (Error)^2 for each point. We should like to use $\chi^2_{tot} = \sum_{i=1}^{N_{tot}} \chi^2_i$ so treating every experimental point equally. When looking at the results, however, what we should like to see is that each individual *data set* has been fitted reasonably and *not* that some have been fitted poorly and some fitted exceptionally well to compensate. This would suggest using $\chi^2_{tot} = \sum_{j=1}^{N_{sets}} \chi^2_j/N_{set(j)} = \sum_{j=1}^{N_{sets}} \sum_{k=1}^{N_{set(j)}} \chi^2_{jk}/N_{set(j)}$, i.e. rescaling the χ^2 to each data set by dividing by the number of data points in that set. However, in practice, it is found that a reasonable fit to each set individually can be obtained with the former criterion, so that is what we use. In using this criterion, we might think that we should be hoping to see χ^2_{tot} within the approximate range $(N_{tot} - \sqrt{2N_{tot}}) < \chi^2_{tot} < (N_{tot} + \sqrt{2N_{tot}})$ (corresponding to the one standard deviation limits—see [51]) but we would be abusing statistics if we did. This is because the errors we shall be using are not intrinsic statistical errors but will

be the resultant of the statistical and systematic errors added in quadrature i.e. error= $\sqrt{\epsilon^2_{\rm stat} + \epsilon^2_{\rm sys}}$. Thus, a true statistical interpretation of the χ^2_{tot} is not valid because of our standard "physicists' " treatment of the $\epsilon_{\rm sys}$ whereby χ^2_{tot} will certainly be less than the statistically correct one. As an example, data sets with very large systematic errors may well give $\chi^2 \approx 0$ for virtually any theoretical fit. Thus we should perhaps be expecting, very roughly, $0 < \chi^2_{tot} < (N_{tot} + \sqrt{2N_{tot}})$ and similarly for each data set individually (with abnormally small χ^2 values due to large systematic errors and *not* due to the theoretical fit following every small fluctuation).

In this fitting to deep-inelastic data, the $F_2^{\mu n}/F_2^{\mu p}$ data have been singled out for some special attention. As has been previously mentioned, we can have a higher degree of confidence in these data since there is no overall normalization uncertainty. Therefore, we make a special point of trying to fit these data well. Since there are so few points, we find it useful to perform some weighting. Since we are especially interested in reproducing the low-x shape of the NMC measurement, we find that a large weighting factor applied to the χ^2 value of the $x = 0.03$ point ensures a good reproduction of this shape. We decide on the magnitude of this weighting by performing fits to all the deep-inelastic data with a range of weightings of this data point. We then plot the total χ^2 of the three $F_2^{\mu n}/F_2^{\mu p}$ data sets versus this weighting factor and take the optimum weighting factor to be that near the minimum (*near* and not *at* because we also take into account any adverse effect of this weighting on the χ^2 to the other data sets).

The final subtlety we introduce is based on the fact (see §4.4) that, at high x, $d_V \to 0$ faster than $u_V \to 0$ (see Equations (4.8) and (4.9)). We arrange this by minimizing with respect to a parameter $(\eta_4 - \eta_2)$ in place of η_4. We then perform fits to all the deep-inelastic data for a range of values of $(\eta_4 - \eta_2) > 0$ and choose an optimum value (with respect to $\chi^2(F_2^{\mu n}/F_2^{\mu p})$ since $F_2^{\mu n}/F_2^{\mu p}$ is a function of d_V/u_V only at high x) which is then fixed in all subsequent fits.

The algorithm of the computer program we use [52] is as follows:

i) The experimental data and the initial Q_0^2 parametrization are read into arrays.

ii) The parton momentum distributions are evolved at next-to-leading order

to a value of Q^2 higher than that of any of the data. The integrations (on the right hand side of the Altarelli-Parisi equations and all auxiliary integrations) are performed using a Gaussian quadrature rule. The differential equations (e.g.

$$\frac{\partial q_i(x,Q^2)}{\partial \ln Q^2} = \text{ number)}$$

are solved using a modified predictor-corrector method [53] with a step size $\Delta s = 0.08$ where

$$s = \ln\left(\frac{\ln(Q^2/\Lambda^2)}{\ln(Q_0^2/\Lambda^2)}\right) \tag{5.17}$$

(this is a more convenient variable to use than $\ln Q^2$)

iii) The physical structure functions are calculated at the appropriate (x, Q^2) values.

iv) The χ^2 $(= \sum_{\text{Data}} ((\text{Theory-Data})/\text{Error})^2)$ is calculated.

v) The parameters are altered (see below) and the process is repeated from step (*ii*).

The program incorporates a minimization procedure which decides how best to alter the parameters to minimize the χ^2. This procedure is based on an algorithm by Marquardt [54]. The program stops when the change in χ^2 between sucessive iterations is less than some pre-set value.

Now, we are ready to perform a range of fits to the deep-inelastic data for pairs of fixed $(\Lambda_{\overline{\text{MS}}}\text{-}\eta_g)$. As has been mentioned, the whole procedure has to be duplicated since the $F_2^{\mu p}$data sets of EMC and BCDMS are incompatible. The starting sets we use for every one of the minimizations at a specific $(\Lambda_{\overline{\text{MS}}}\text{-}\eta_g)$ point are shown in Table 5.1 (where an asterisk denotes that that parameter is fixed in the minimization). Throughout this thesis, $\Lambda_{\overline{\text{MS}}}$ denotes that quantity evaluated with *four* flavours of quark.

	EMC-type	BCDMS-type
$\Lambda_{\overline{MS}}$	*	*
η_g	*	*
η_1	0.373	0.337
η_2	4.04	4.07
γ_{ud}	8.86	11.3
η_3	0.620	0.506
$\eta_4 - \eta_2$	0.75*	0.75*
γ_d	0.818	3.23
A_S	1.61	2.16
δ_S	0.0836	0.131
η_S	7.5	7.5

Table 5.1 Starting values of the parameters used in the minimizations.

5.4 Results

The results are shown in Figures 5.2(a)—5.2(h) as contours of equal χ^2 in the $(\Lambda_{\overline{\rm MS}}$-$\eta_g)$ plane. Figure 5.2(g) (5.2(h)) shows the total χ^2 for the fit which included the EMC (BCDMS) $F_2^{\mu p}$ data. The rest of the plots show the components of that total in terms of the combined χ^2 of the three $F_2^{\mu n}/F_2^{\mu p}$ sets (DIS(n/p)), the χ^2 of the relevant $F_2^{\mu p}$ set (DIS($F_2^{\mu p}$)), and the combined χ^2 of the $F_2^{\nu N}$ and $xF_3^{\nu N}$ (DIS(F_2^{ν})) sets. (It is important to realize, therefore, that these component plots show the variation in fit quality of the specified data set *subject to* the constraint of the other data sets. The EMC (BCDMS) results are in the left(right)-hand columns.

First, we discuss the fits using the EMC $F_2^{\mu p}$ data. Figure 5.2(a) shows a very weak dependence on the $F_2^{\mu n}/F_2^{\mu p}$ data over the range of the plot. However, since we have fixed the parameter $(\eta_4 - \eta_2)$ to ensure a good fit to this data, this is not too surprising.

Figure 5.2(c) shows that the dependence on the EMC $F_2^{\mu p}$ data is also quite weak. This is for a different reason—it is due to the relatively large errors on

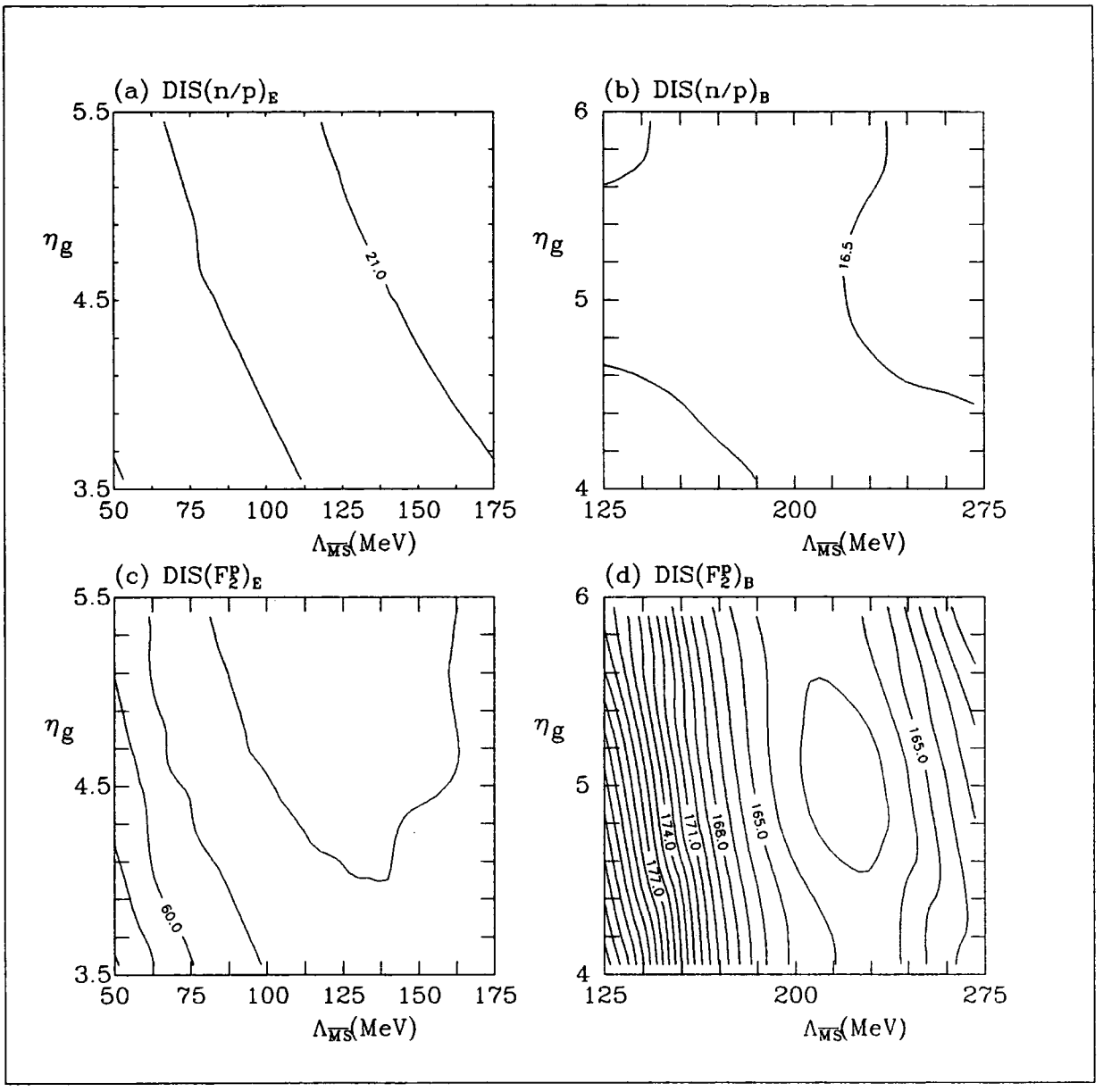

Figure 5.2 Components of the total χ^2 obtained by globally fitting to $F_2^{\mu p}$ [32], [16], $F_2^{\nu N}$ and $xF_3^{\nu N}$ [36], and $F_2^{\mu n}/F_2^{\mu p}$ [40], [42], [43] data over a range of $\Lambda_{\overline{\rm MS}}$ and η_g. The contour interval is one unit of χ^2. The starting parameters for each of the fits are given in Table 5.1. (a) shows the total χ^2 to all three sets of $F_2^{\mu n}/F_2^{\mu p}$ data for the fit which used the EMC $F_2^{\mu p}$ data and (c) shows the χ^2 to that $F_2^{\mu p}$ data. (b) and (d) show the corresponding contours for the fits which used the BCDMS $F_2^{\mu p}$ data. All statistical and systematic errors have been combined in quadrature. The EMC $F_2^{\mu p}$ data were renormalized upwards by 8% and those of BCDMS downwards by 2%. The neutrino data were corrected for the "EMC effect" according to Equation (4.6) (see, also, Figure 4.3).

those data. This is unfortunate since it means that those data do not carry much

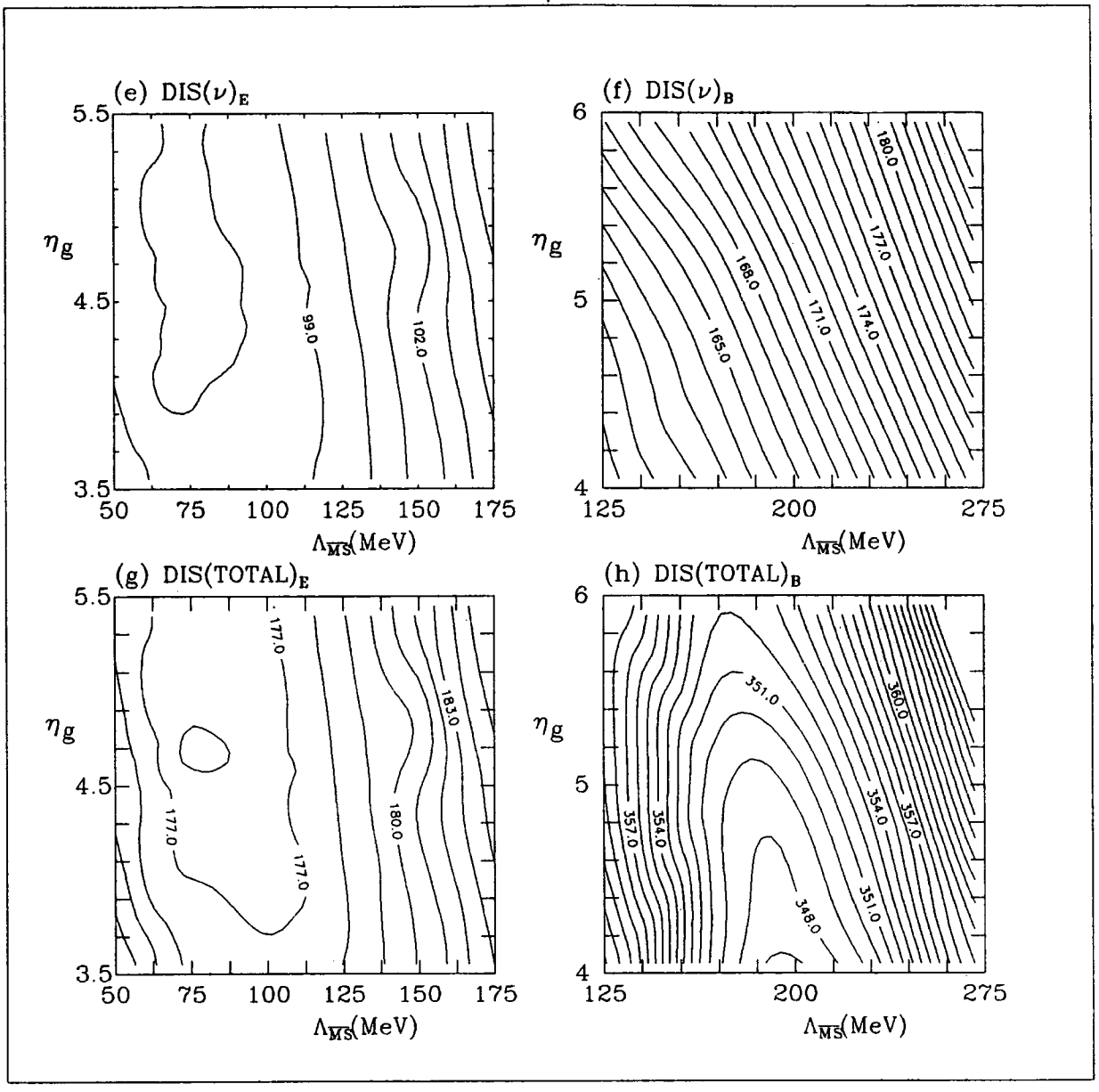

Figure 5.2 (cont.) Components of the total χ^2 obtained by globally fitting to $F_2^{\mu p}$ [32], [16], $F_2^{\nu N}$ and $xF_3^{\nu N}$ [36], and $F_2^{\mu n}/F_2^{\mu p}$ [40], [42], [43] data over a range of $\Lambda_{\overline{\rm MS}}$ and η_g. The contour interval is one unit of χ^2. The starting parameters for each of the fits are given in Table 5.1. (e) shows the total χ^2 to the $F_2^{\nu N}$ and $xF_3^{\nu N}$ data for the fit which used the EMC $F_2^{\mu p}$ data and (g) shows the total χ^2 for that fit. (f) and (h) show the corresponding contours for the fits which used the BCDMS $F_2^{\mu p}$ data. All statistical and systematic errors have been combined in quadrature. The EMC $F_2^{\mu p}$ data were renormalized upwards by 8% and those of BCDMS downwards by 2%. The neutrino data were corrected for the "EMC effect" according to Equation (4.6) (see, also, Figure 4.3).

weight in the joint fit. We could, of course, have weighted them in one of two

ways: either by artificially reducing the errors before the minimization; or by weighting the χ^2 after the minimization. However, having no good reason for increasing the importance of those data, we decided not to weight them. This plot shows, however, that those data do favour a broad range of values of $\Lambda_{\overline{\rm MS}}$ but are fairly tolerant to the range in η_g.

Figure 5.2(e) shows that the neutrino scattering data behave similarly: there is a favoured band of $\Lambda_{\overline{\rm MS}}$ with little dependence on η_g. Notice, however, that the central value of $\Lambda_{\overline{\rm MS}}$ is here somewhat lower than that of the EMC $F_2^{\mu p}$ data.

Figure 5.2(g), then, shows the sum of Figures 5.2(a,c & e). It is clearly dominated by the behaviour of the neutrino scattering data and gives us a broad range of favoured values of $\Lambda_{\overline{\rm MS}}$ centred around 80 MeV but poor resolution in η_g (relative to the range covered in this plot).

Next, we turn to the results of those fits which included the BCDMS $F_2^{\mu p}$ data. Again, we see, in Figure 5.2(b), that there is little dependence on the $F_2^{\mu n}/F_2^{\mu p}$ data. Figure 5.2(d), however, clearly demonstrates the accuracy of the BCDMS $F_2^{\mu p}$ data with its high density of contour lines. Because of this, the favoured range in $\Lambda_{\overline{\rm MS}}$ is more precisely delineated although η_g is once more poorly determined. The neutrino-scattering data in Figure 5.2(f) seem quite at odds with this, seeming to favour low values of both variables (although there is a clear correlation between $\Lambda_{\overline{\rm MS}}$ and η_g so it is possible that a very low value of η_g might give a value of $\Lambda_{\overline{\rm MS}}$ consistent with that of Figure 5.2(d) with a reasonable χ^2). The resultant plot, Figure 5.2(h), shows that the acceptable region for the $F_2^{\mu p}$ data has been pulled down to lower $\Lambda_{\overline{\rm MS}}$ and lower η_g.

We can examine the compatibility between the $F_2^{\mu p}$ data sets and the neutrino scattering data sets in aother way. With a sea composition of $\overline{u} = \overline{d} = 2\overline{s}$, we have the equality

$$\frac{F_2^{\mu n}}{F_2^{\mu p}} = \frac{11F_2^{\nu N} - xF_3^{\nu N}}{18F_2^{\mu p}} - 1 \qquad (5.18)$$

We calculate the fraction on the right-hand side using the neutrino scattering data of CDHSW and the $F_2^{\mu p}$ data of either BCDMS or EMC. We can then compare this derived value with well-determined experimental $F_2^{\mu n}/F_2^{\mu p}$ data. Figure 5.3 shows the outcome: 'the EMC-derived' values are in agreement with the ex-

perimental values while the 'BCDMS-derived' ones clearly are not—even though the experimental values shown are those of BCDMS. It is possible, therefore, that the high-x BCDMS $F_2^{\mu p}$ data are systematically too low. It is also possible, however, that the fault lies in the CDHSW neutrino data (in particular, the $F_2^{\nu N}$ data since those data dominate the numerator of the right-hand side of (5.18)). It is apparent from Figure 5.3, though, that it would be impossible to remedy the situation with a renormalization of any of the data sets.

5.5 Conclusions

We have found broad ranges of $\Lambda_{\overline{\rm MS}}$ for our EMC-type and BCDMS-type fits. These ranges, however, are not in agreement with each other if we are to take a value whose χ^2 is within a few units of the most favoured value (which, for the EMC-type fit is around 75 MeV and, for the BCDMS-type fit, around 200 MeV).

There appears to be inconsistency between the BCDMS $F_2^{\mu p}$ data and the CDHSW $F_2^{\nu N}$ and $xF_3^{\nu N}$ data.

Neither type of fit gives precise information on the value of η_g.

We should note here that the promised $\Lambda_{\overline{\rm MS}} - \eta_g$ correlation does not appear particularly marked in Figures 5.2(g) and 5.2(h) but this is due to the restricted ranges of η_g that we have shown. We chose these ranges because we were concentrating on the region we knew, from preliminary studies, would be relevant after consideration of the prompt photon data and we concentrated our computing efforts on the attainment of an accurate contour picture of that region.

Before we consider the prompt photon data in the next chapter, we will briefly remark on alternative methods for determining $\Lambda_{\overline{\rm MS}}$ which reduce or eliminate any dependence on η_g

There are, in principle, three easy ways of determining $\Lambda_{\overline{\rm MS}}$ according to this criterion.

i) We fit to DIS data as before, but we confine ourselves to considering a region of x, high enough such that the gluon distribution there is negligible. This, of course, begs the question, at what x can we neglect the gluon distribution? Since

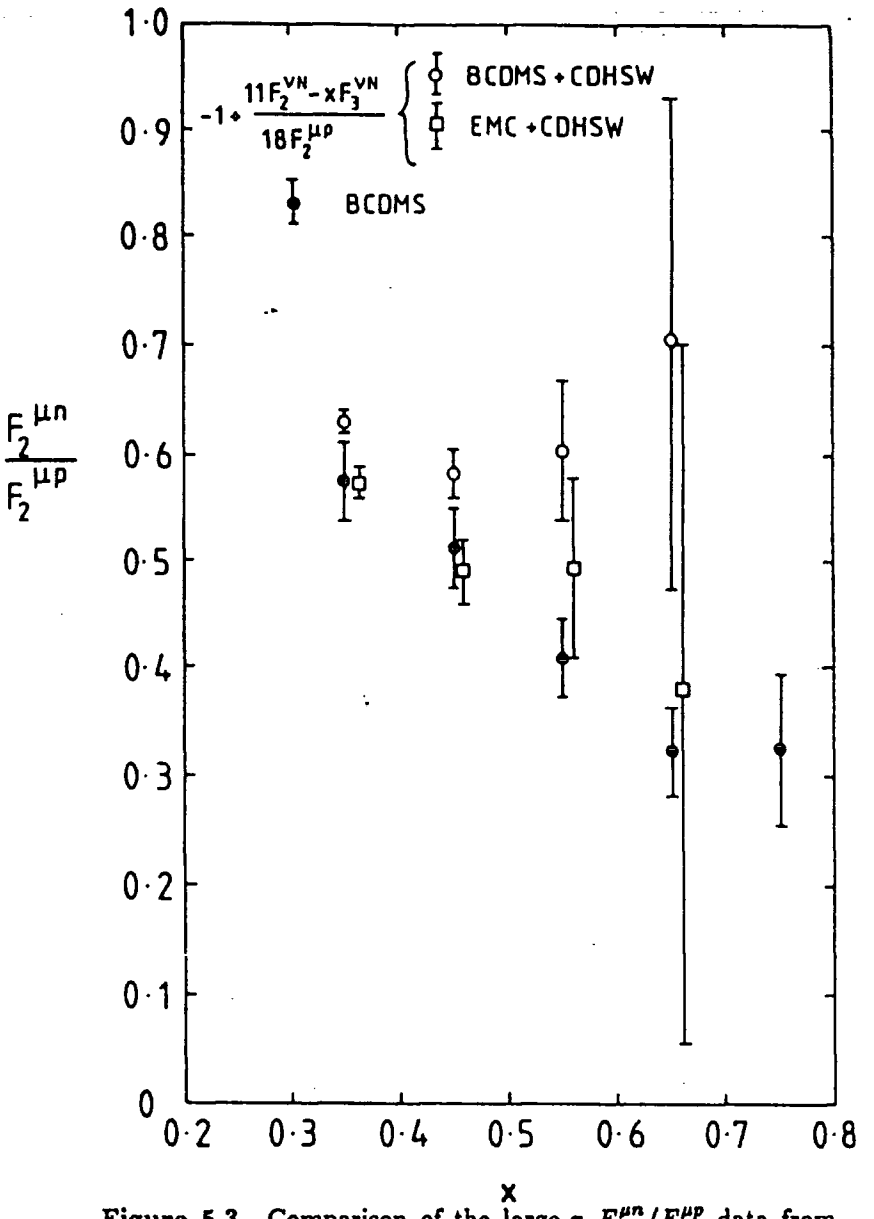

Figure 5.3 Comparison of the large-x $F_2^{\mu n}/F_2^{\mu p}$ data from the BCDMS collaboration [42] (solid circles) with the "effective" ratio derived from the $F_2^{\nu N}$ and $xF_3^{\nu N}$ structure function data (according to Equation (5.18)), using respectively the EMC (open squares) and BCDMS (open circles) $F_2^{\mu p}$ data. Note that the neutrino data are corrected for the "EMC effect".

it is *a priori* unknown, we should have to err on the safe side and choose quite a large value ($x > 0.5$, say). However, by doing this, we have to contend with two problems: we have considerably reduced the amount of data we can use; and the data at high x are the most uncertain. Thus, in this approach, we are likely to

determine a value of $\Lambda_{\overline{\rm MS}}$ with even bigger errors than we have already.

ii) We fit to combinations of physical structure functions that correspond to the sum of differences of quark distributions, $\sum(q_i - q_j)$. Consideration of the Altarelli-Parisi equation for the evolution of such a 'non-singlet' distribution tells us that the gluon distribution cancels out. One such physical structure function is

$$xF_3^{\nu d} = x(u_V + d_V) = x \sum_{q=u,d} (q - \overline{q}) \ . \tag{5.19}$$

However, we again find that, due to the inaccuracy of the data, we obtain rather large errors on $\Lambda_{\overline{\rm MS}}$ (especially if we compound experimental errors by forming a combination of physical structure functions to obtain a non-singlet distribution, such as $3(F_2^{ep} - F_2^{en}) = u_V - d_V$).

iii) Moments analysis of non-singlet distributions can, in principle, tell us $\Lambda_{\overline{\rm MS}}$ through a simple linear plot:

$$M_n(Q^2)^{-1/d_n^{NS}} = const.(\ln Q^2 - \ln \Lambda^2) \tag{5.20}$$

where the nth moment, M_n, is defined by

$$M_n^{\rm NS}(Q^2) = \int_0^1 dx x^{n-1} q^{\rm NS}(x, Q^2) \ . \tag{5.21}$$

The limits here are our problem—we must extrapolate our measured $q^{\rm NS}$ (e.g. $xF_3^{\nu d}$) to $x = 0$ and to $x = 1$ which inevitably introduces errors.

In the next chapter, we turn to consideration of the gluon distribution.

6. Prompt Photon Production

6.1 Introduction

Recently, there has been much interest in the prompt photon (also called 'direct photon') production process as an aid in the determination of parton momentum distributions. This is partly because both theory and experiment are in an advanced state—with full next-to-leading order expressions [55], [56], [57] and high precision data [58] available—but mainly because this process gives very good information on the form of the gluon distribution without having too great a dependence on the value of the mass-scale parameter $\Lambda_{\overline{\rm MS}}$. Thus, it may complement deep-inelastic data—for which the $\Lambda_{\overline{\rm MS}}$ and gluon distribution dependence is the opposite—and allow us to determine both of these unknowns. This idea has also been pointed out by Aurenche *et al.* [59] (see §6.6).

6.2 Theory

The two lowest-order ($O(\alpha\alpha_s)$) diagrams needed to calculate the differential cross-section for this process are given in Figure 6.1 (we might expect the annihilation subprocess to dominate in $p\overline{p}$ collisions where there are valence antiquarks and the Compton subprocess to dominate in pp collisions where the only antiquarks are in the sea). The differential cross-section for the inclusive process $pp \rightarrow \gamma X$ (with A and B representing the parent protons and a and b the respective initial state quarks) is

$$E_\gamma \frac{d^3\sigma}{d^3p_\gamma} = \sum_{abcd} \int dx_a dx_b G_{a/A}(x_a, M^2) G_{b/B}(x_b, M^2) \frac{\hat{s}}{\pi} \frac{d\sigma}{d\hat{t}}(ab \rightarrow cd) \delta(\hat{s} + \hat{t} + \hat{u}) \tag{6.1}$$

where $G = q$ or g (whence, we can see that, for the Compton diagram, there is a direct dependence on the gluon distribution) and

$$\frac{d\sigma}{d\hat{t}} = \begin{cases} \frac{-e_q^2}{3}\left[\frac{\hat{u}}{\hat{s}} + \frac{\hat{s}}{\hat{u}}\right]\frac{1}{\hat{s}^2}\pi\alpha\alpha_s(Q^2) & \text{Compton} \\ \frac{8e_q^2}{9}\left[\frac{\hat{u}}{\hat{t}} + \frac{\hat{t}}{\hat{u}}\right]\frac{1}{\hat{s}^2}\pi\alpha\alpha_s(Q^2) & \text{Annihilation} \end{cases} \tag{6.2}$$

with $\hat{s} = x_a x_b s$, $\hat{t} = -x_a p_T \sqrt{s} e^{-y}$ and $\hat{u} = -x_b p_T \sqrt{s} e^{y}$. y is the rapidity of the

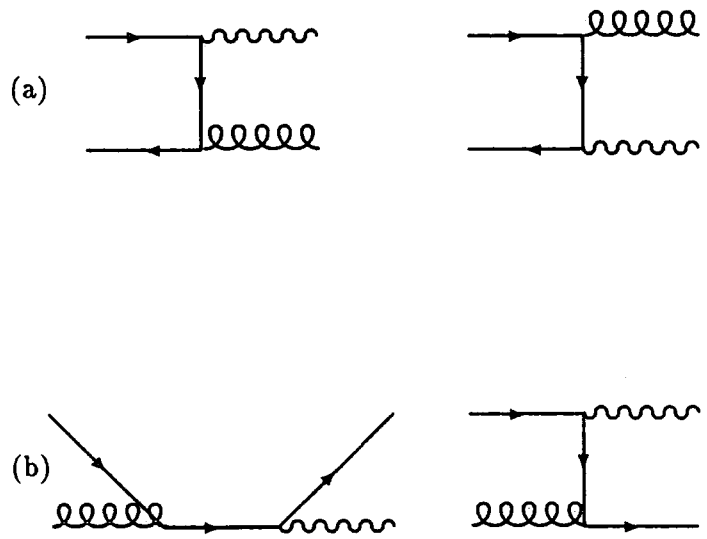

Figure 6.1 Lowest order diagrams for prompt ('direct') photon production: (a) $q-\overline{q}$ annihilation and (b) the Compton process.

photon defined by

$$y = \frac{1}{2}\ln\left(\frac{E+p_L}{E-p_L}\right) \ . \tag{6.3}$$

The scale M^2 in $G(x,M^2)$ is the factorization scale at which radiative corrections to the incoming and outgoing partons are absorbed into the distribution functions. The scale Q^2 in $\alpha_s(Q^2)$ arises when one takes certain vertex and gluon propagator effects into account, as discussed in §3.4 and §3.6. In the leading logarithm approximation, the all-orders cross-section is given by Equation (6.1) with the $d\sigma/d\hat{t}$'s of the Compton and annihilation diagrams and the one-loop approximation for α_s, viz.

$$\alpha_s(Q^2) = \frac{12\pi}{(33-2N_F)\ln(Q^2/\Lambda^2_{\rm LO})} \tag{6.4}$$

(where Q^2 is a large momentum scale characteristic of the process) and parton distributions, $G(x,M^2)$ evolved at leading order.

The next-to-leading logarithm calculation is that of Aurenche *et al.* [55], [56], [57]. Some of the diagrams that have to be considered are shown in Figure 6.2. The full expression for $d^3\sigma/d^3p_\gamma$ is "rather lengthy, when the next-to-leading order QCD corrections ... are all included" [57] and has not been published, although the analytic expressions are available in FORTRAN from the authors.

There are several methods for dealing with the unknown scales Q^2 and M^2. These include: setting $M^2 = Q^2 = p_T^2$, the square of the transverse momentum of the photon; the 'fastest apparent convergence' method (FAC) [60], [61] in which M^2 and Q^2 are taken to be equal and varied until the next-to-leading order contributions vanish; and the 'principle of minimum sensitivity' [62], [63], [64]. The latter determines Q^2 and M^2 by ensuring that the cross-section has no local variation with respect to these scales, just like the all-orders cross-section, i.e. it demands that $\partial\sigma/\partial Q^2(Q^2_{opt}, M^2_{opt}) = 0$ and that $\partial\sigma/\partial M^2(Q^2_{opt}, M^2_{opt}) = 0$. This is the method that we shall be using. The factorization scale is first parametrized by $M^2 = Cp_T^2(1 - x_T)$. Then, for each data point, a range of values of C is tried. For each trial, the value of the running coupling (which is used in place of Q^2 for convenience) is set to be that which *maximizes* the cross-section. The range of cross-sections is then scanned for the minimum value. This method locates the saddle-point in the $\alpha_s - C$ plane at which there is no local variation of the cross-section to either of the scales. It has been shown, though, that the PMS and FAC procedures give very similar results and that the naïve $M^2 = Q^2 = p_T^2$ destroys the agreement between the different sets of experimental prompt photon data and also prevents the existence of a gluon distribution consistent with both prompt photon and deep-inelastic data [57].

Another scheme-dependent problem which occurs beyond the leading order is that of the definition of the quark distributions. There are two commonly used conventions: the $\overline{\text{MS}}$ ('universal') convention and the physical ('non-universal') convention. We shall, of course be using the $\overline{\text{MS}}$ convention as with the deep-inelastic analysis. Aurenche *et al.* [57] have shown that there is little difference between these definitions insofar as the resultant gluon is concerned.

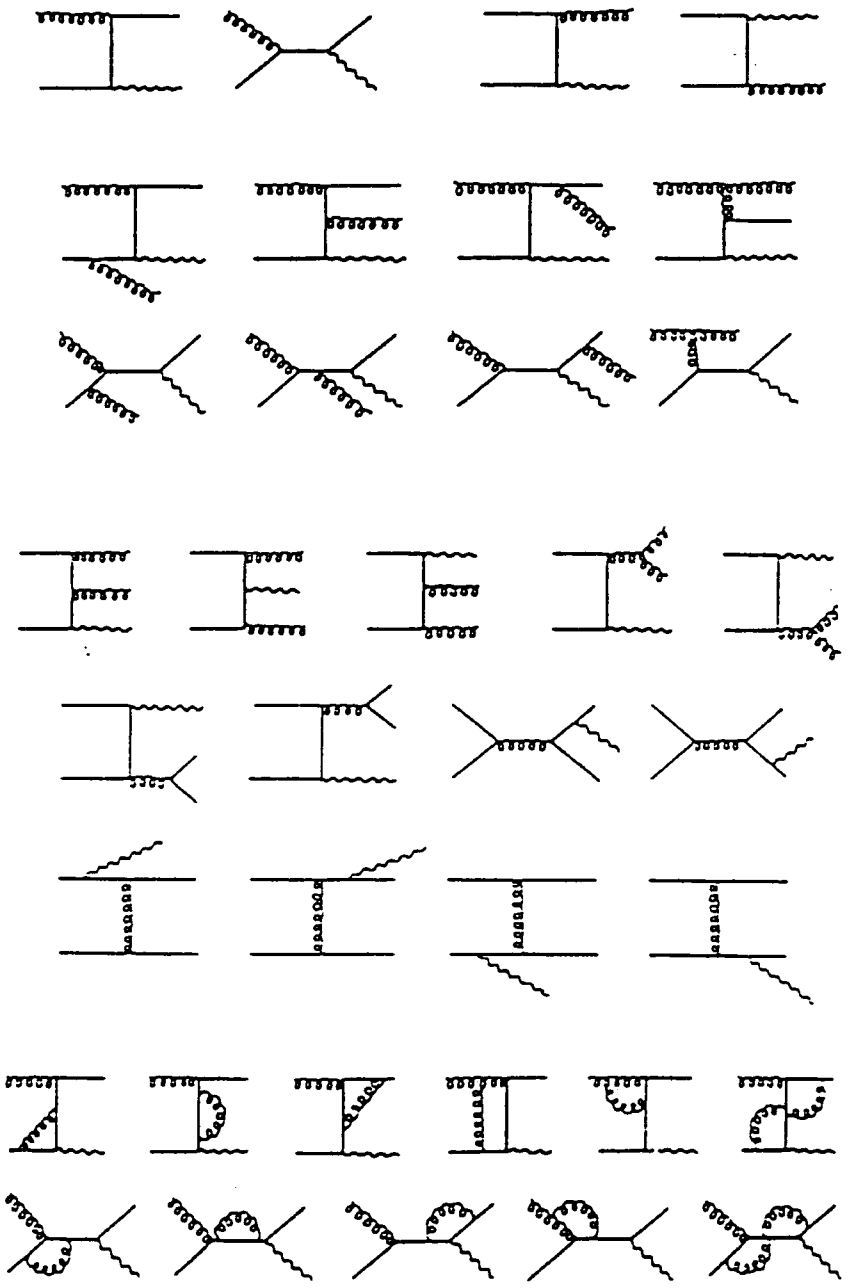

Figure 6.2 Diagrams that contribute to the calculation of the prompt photon cross-section up to order $\alpha\alpha_s^2$.

6.3 Sensitivity to the Gluon Distribution

How well, do we expect prompt photon production data to determine the

gluon? We can rewrite the differential cross-section (Equation (6.1)) as

$$E_\gamma \frac{d^3\sigma}{d^3p_\gamma} = \sum_{abcd} \int_{x_{amin}}^{1} dx_a G_{a/A}(x_a) G_{b/B}(x_b) \frac{2}{\pi} \frac{x_a x_b}{2x_a - x_T e^y} \frac{d\hat{\sigma}}{d\hat{t}}(ab \to cd) \qquad (6.5)$$

where

$$x_b = \frac{x_a x_T e^{-y}}{2x_a - x_T e^y}, \quad x_T = \frac{2p_T}{\sqrt{s}}, \quad x_{a_{min}} = \frac{x_T e^y}{2 - x_T e^{-y}} . \qquad (6.6)$$

Figure 6.3 shows the integrand for $x_T = 0.38$, $\sqrt{s} = 22.96$ GeV, $y = 0$ using the Duke and Owens (Set 1) set of leading-order parton distributions [65]). We see that the integrand is dominated by x_a (and x_b) values in the approximate range $x_T - 0.1 \lesssim x_a, x_b \lesssim x_T + 0.1$. This behaviour is the same for a wide range of x_T and is fairly insensitive to the detailed form of the parton distributions. So, in fact, the sensitivity of the cross-section to the gluon distribution is confined to quite a small region around x_T so we should expect to obtain information on it, mainly between the smallest and largest x_T values of the data. As with our DIS analysis, we take our parametrization to be $xg(x, Q_0^2) = A(1-x)^\eta$.

6.4 Fitting to the WA70 Prompt Photon Data

There is a wealth of data on prompt photon production [58] and we choose to use the subset of the WA70 collaboration's data [66] with $-0.35 < x_F < 0.45$ (the largest range in x_F at $\sqrt{s} = 22.96$ GeV). This provides us with a range in x_T of $0.36 < x_T < 0.55$. As these data are over a range in rapidity, we correct each point for finite bin size to the equivalent cross-section at $y = 0$ for ease of comparison with theoretical cross-sections. The factors we use [67] (and which depend *slightly* on the parton distributions assumed for the proton) are given in Table 6.1: the data are corrected by *dividing* by these factors.

Having selected our prompt photon data, we shall now discuss how it is used in the analysis. As before, for a range of pairs of $\Lambda_{\overline{\rm MS}}$ and η_g, we perform a fit to the DIS data, so we know we have a set of parton distributions consistent with the DIS data, and use each of these sets to calculate the cross-section for prompt photon production at next-to-leading order, using the PMS criterion to find unique renormalization and factorization scales (in practice, the optimum

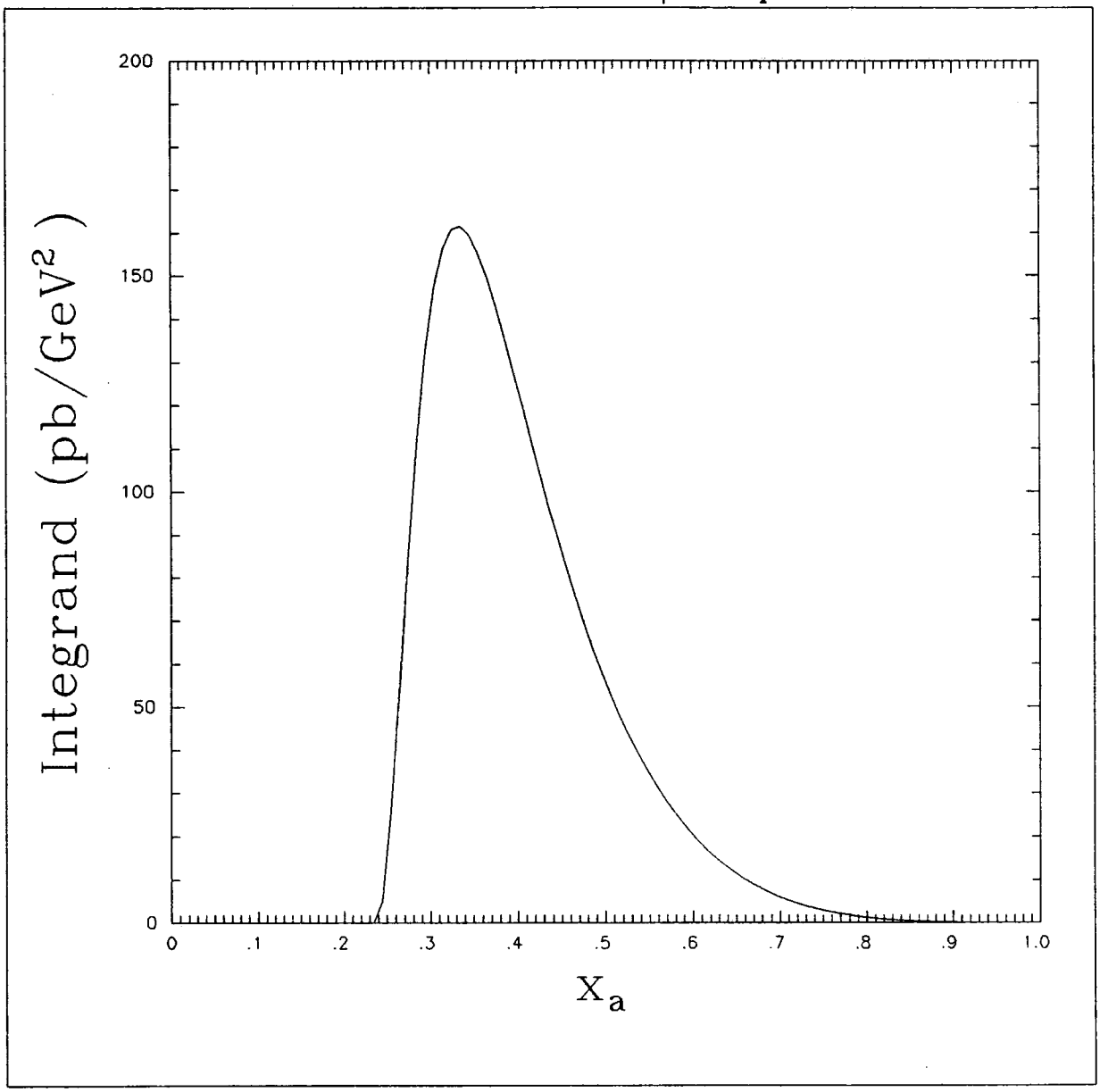

Figure 6.3 The integrand of the lowest order expression for the cross-section for prompt photon production (Equation (6.5)). $x_T = 0.38$, $\sqrt{s} = 22.96$ GeV, and $y = 0$. The leading-order parton distributions used are those of Duke and Owens (Set 1) [65].

factorization scale is often below the $Q_0^2 = 4$ GeV^2 of our parametrization in which case we use $M^2 = 4$ GeV^2 as an approximation which does not introduce any serious error).The results are shown by the contour plots in Figures 6.4((a)—(d)).

First, we discuss the EMC-type results . Figure 6.4(a) is the χ^2 to the WA70

p_T	Factor
4.11	0.670
4.36	0.669
4.61	0.667
4.86	0.663
5.11	0.658
5.36	0.653
5.70	0.644
6.20	0.624

Table 6.1 Factors used to correct the WA70 prompt photon data for $-0.35 < x_F < 0.45$ to their equivalent values at $y = 0$.

data alone. In complete contrast to Figure 5.2(g), we see that here it is η_g that is quite well-determined and $\Lambda_{\overline{\rm MS}}$ that is ill-determined. This is an ideal situation as the respective minimum bands cross almost perpendicularly. In the sum of the two plots, Figure 6.4(c), we see that, despite there being only eight WA70 data points, the resultant is dominated by the form of the fit to the prompt photon data. This is because the variation in the DIS(TOTAL)$_E$ plot is very weak (note that the contour-line spacing in Figure 5.2(g) is one unit whereas, in Figure 6.4(c), it is three units). We choose, as our fit that best describes the deep-inelastic and prompt photon data, the one marked with a triangle, viz. that with $\eta_g = 4.4$ and $\Lambda_{\overline{\rm MS}} = 100$ MeV.

Turning to the BCDMS-type fits, we see a similar story. Figure 6.4(b) again pinpoints a narrow band of values of η_g and, when added to Figure 5.2(h) (which is quite specific about the favoured range of $\Lambda_{\overline{\rm MS}}$) gives, in Figure 6.4(d), a nicely-defined minimum from where we select the point $\eta_g = 5.1$, $\Lambda_{\overline{\rm MS}} = 190$ MeV as our best fit. This is reasonably close to the individual minima of all the components bar the neutrino scattering data.

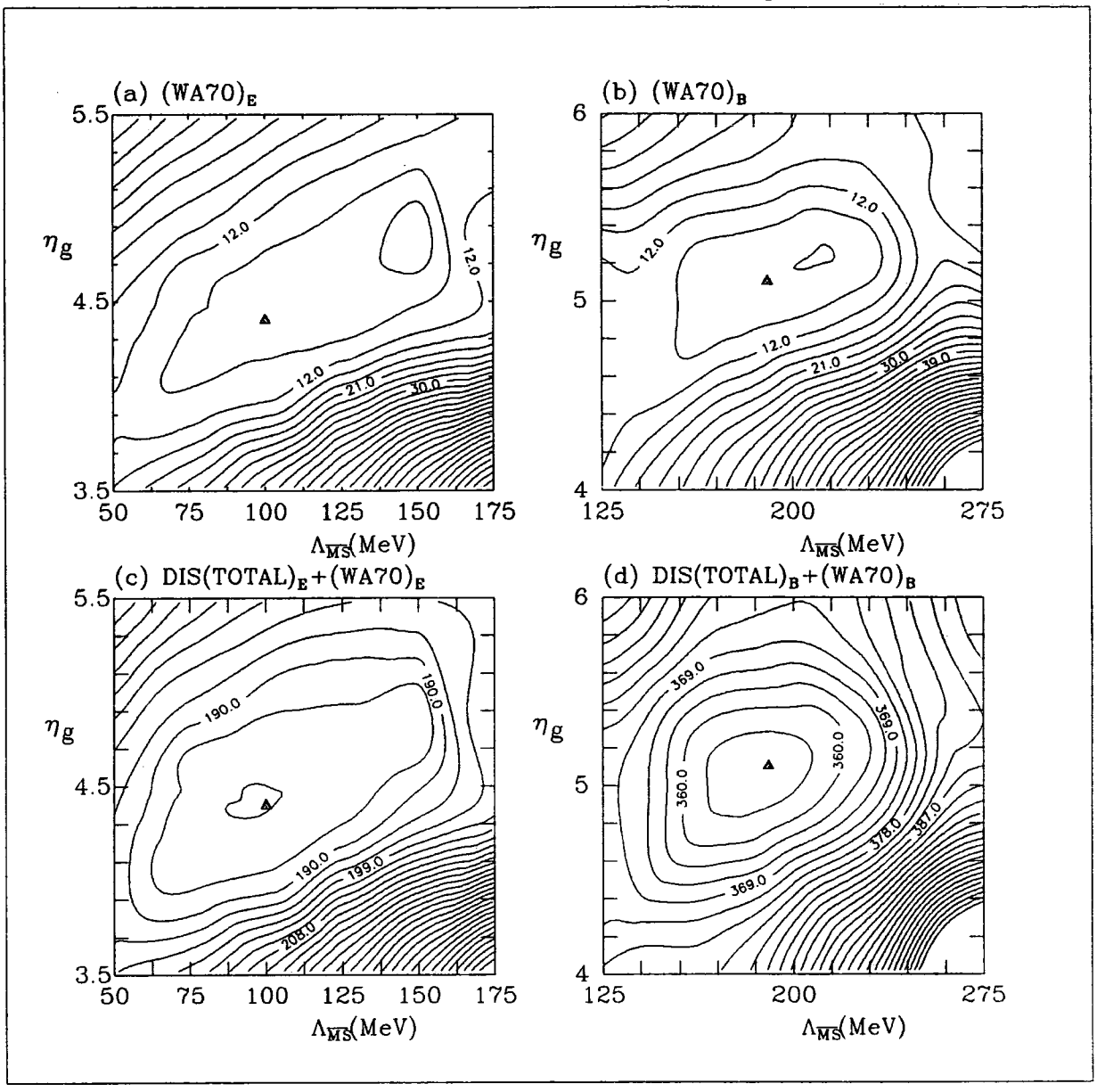

Figure 6.4 (a) and (b) show contours of constant χ^2 (with an interval of three units) in the $\Lambda_{\overline{\rm MS}} - \eta_g$ plane where χ^2 is a measure of the quality of the theoretical prediction for the WA70 prompt photon data [66] in the range $-0.35 < x_F < 0.45$ (corrected to $y = 0$) using the various sets of parton distributions obtained by fitting to the deep-inelastic scattering data of ((a))[32], ((b))[16] ($F_2^{\mu p}$), [36] ($F_2^{\nu N}$ and $xF_3^{\nu N}$) and [40], [42], [43] ($F_2^{\mu n}/F_2^{\mu p}$) The statistical and systematic errors of all data have been combined in quadrature. (c) and (d) show the corresponding total χ^2 when the χ^2 to all the deep-inelastic data is added and indicates the quality of the simultaneous description of the deep-inelastic and prompt photon data. The optimum overall description is obtained for the values of $\Lambda_{\overline{\rm MS}}$ and η_g shown by the triangles.

6.5 Comparison with a Similar Analysis

Aurenche *et al.* [59] have performed a similar joint analysis of prompt photon production data and deep-inelastic scattering data and so here we point out some differences and similarities between that work and this one.

Both analyses are performed with the same computer programs and use the same prompt photon data, but the deep-inelastic scattering data that Aurenche *et al.* use consists of just the $F_2^{\mu p}$ and $F_2^{\mu n}/F_2^{\mu p}$ data of BCDMS. With regard to the DIS data, then, the main difference is our inclusion of neutrino-scattering data and the recent NMC $F_2^{\mu n}/F_2^{\mu p}$ data with its much tighter constraints, especially at low x. The parametrizations used for the parton distributions at $Q^2 = Q_0^2$ are identical apart from that for xSea: our factor of $x^{\delta s}$—introduced to aid the fitting of the low-x NMC data—is absent from that of Aurenche *et al.* In addition, we do not assume an SU(3) symmetric sea, as they do, and we use $Q_0^2 = 4$ GeV^2 compared to their $Q_0^2 = 2$ GeV^2 (this lower value aids their analysis by enabling prompt photon prodection data points with low p_T to be 'PMS-optimized' exactly, i.e. it is lower than any required optimized factorization scale).

7. The Drell-Yan Process

7.1 Introduction

There is at least one more point we ought to consider for our parton distributions: we have no good reason to believe that the quark distributions are apportioned correctly between the valence and sea parts. We should like an accurate determination of one of these things. Fortunately, there exist accurate data on a process which is very sensitive to the antiquark distribution in the sea.

7.2 Theory

The final process we shall make use of in our determination of a set of parton distributions is the Drell-Yan process [68], [69]. This is the process $AB \to l^+l^-X$ where A and B are hadrons and l a lepton. The basic subprocess for this is $q\overline{q} \to \gamma^* \to l^+l^-$ (see Figure 7.1) with a cross-section (the same as the QED $e^+e^- \to \mu^+\mu^-$ apart from the quark charge factor)

$$\hat{\sigma} = e_q^2 \frac{4\pi\alpha^2}{3M^2} \tag{7.1}$$

where M is the (large) invariant mass of the dilepton pair (or $q\overline{q}$ pair)

$$\begin{aligned} M^2 &= (x_1 P_A + x_2 P_B)^2 \\ &= x_1^2 M_A^2 + x_2^2 M_B^2 + 2x_1 x_2 P_A \cdot P_B \\ &\approx x_1 x_2 s \end{aligned} \tag{7.2}$$

where the masses of A and B have been neglected to obtain the last line, and s is the square of the centre-of-mass energy. Since we shall not be considering fixed M^2, we rewrite (7.1) as the differential cross-section

$$\frac{d\hat{\sigma}}{dM^2} = e_q^2 \frac{4\pi\alpha^2}{3M^2} \delta(\hat{s} - M^2) \; . \tag{7.3}$$

Convoluting with the parton momentum distributions and introducing the scaling

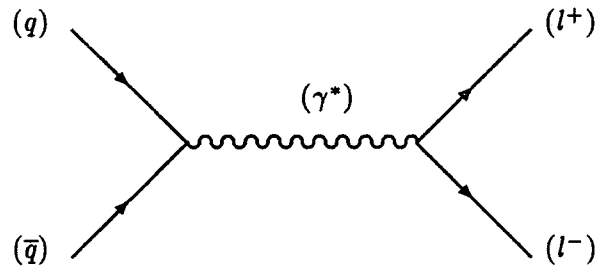

Figure 7.1 Lowest-order diagram for the Drell-Yan process.

variable

$$\tau = M^2/s \leq 1 \tag{7.4}$$

we obtain

$$\frac{d\sigma^{AB\to l^+l^-X}}{dM^2} = \sum_{q=u,d,s,c,b,..} \int_0^1 dx_1 dx_2 \left[G_{q/A}(x_1, M^2)G_{\bar{q}/B}(x_2, M^2) + (q \leftrightarrow \bar{q})\right] \cdot \frac{1}{3} e_q^2 \frac{4\pi\alpha^2}{3M^2} \delta(x_1 x_2 - \tau)\delta(\hat{s} - M^2) \tag{7.5}$$

where (1/3) is the proportion of the nine $q\bar{q}$ states which are colour singlets and where the parton momentum distributions have acquired the same scale dependence as in deep-inelastic scattering after absorbing the mass singularities of the leading logarithm contributions such as

$$qg \to q\gamma^* \to ql^+l^-$$

and

$$q\bar{q} \to g\gamma^* \to gl^+l^- \ .$$

The incorporation of all the $O(\alpha_s)$ corrections (see Figure 7.2) gives us the

next-to-leading formula

$$\begin{aligned}\frac{d\sigma}{dM^2} = \frac{4\pi\alpha^2}{9s}\int_0^1 dx_1 dx_2 dz \delta(x_1 x_2 z - \tau)\cdot \\ \Big[\Big(\sum_q e_q^2 G_{q/A}(x_1, M^2) G_{\overline{q}/B,M^2}(x_2, M^2) + (A \leftrightarrow B)\Big)\cdot \\ (\delta(1-z) + \frac{\alpha_s(M^2)}{2\pi} f_{q\overline{q}}(z)) + \\ \Big(\sum_q e_q^2 (G_{q/A}(x_1, M^2) + G_{\overline{q}/A}(x_1, M^2)) G_{g/B}(x_2, M^2) + (A \leftrightarrow B)\Big)\cdot \\ \frac{\alpha_s(M^2)}{2\pi} f_{qg}(z)\Big]\end{aligned} \tag{7.6}$$

where

$$\begin{aligned} f_{q\overline{q}} &= \frac{4}{3}\Big((1+\frac{4\pi^2}{3})\delta(1-z) + \frac{3}{(1-z)_+} - 6 - 4z + \\ &\quad 2(1+z^2)(\frac{\ln(1-z)}{1-z})_+\Big) \\ f_{qg} &= \frac{1}{2}\Big((z^2 + (1-z)^2\ln(1-z) + \frac{9}{2}z^2 - 5z + \frac{3}{2}\Big)\ . \end{aligned} \tag{7.7}$$

In fact, the data we shall use is the double differential cross-section $sd^2\sigma/d\sqrt{\tau}dy$ where y is the photon rapidity defined by $x_1 = \sqrt{\tau}e^y$, $x_2 = \sqrt{\tau}e^{-y}$. Now, $d\sqrt{\tau}$ is simply $dM/\sqrt{s}$ (see Equation (7.4)) but the additional y differential makes the corresponding formula fairly unwieldy: it is given in Appendix A in the $\overline{\text{MS}}$ scheme, but we can write it here in abbreviated form as

$$\frac{d^2\sigma}{dM^2 dy} = \frac{4\pi\alpha^2}{9Ms} K(y, M^2)\Big(\sum_q e_q^2 q(x_1, M^2)\overline{q}(x_2, M^2) + (q \leftrightarrow \overline{q})\Big) \tag{7.8}$$

where $K \equiv K_0 K'$ with $K_0(y, M^2)$ accounting for the first-order QCD corrections. The Drell-Yan process is interesting in that the higher order corrections are particularly large with $K \equiv \sigma^{\text{exp}}/\sigma^{\text{LO}} \sim 1.7$. Thus, when we compare our theoretical cross-sections with the experimental data, we use the next-to-leading order expressions and attempt to accomodate even higher-order corrections (which could make a substantial contribution) by allowing ourselves to multiply our next-to-leading order result by another factor, K', which we take

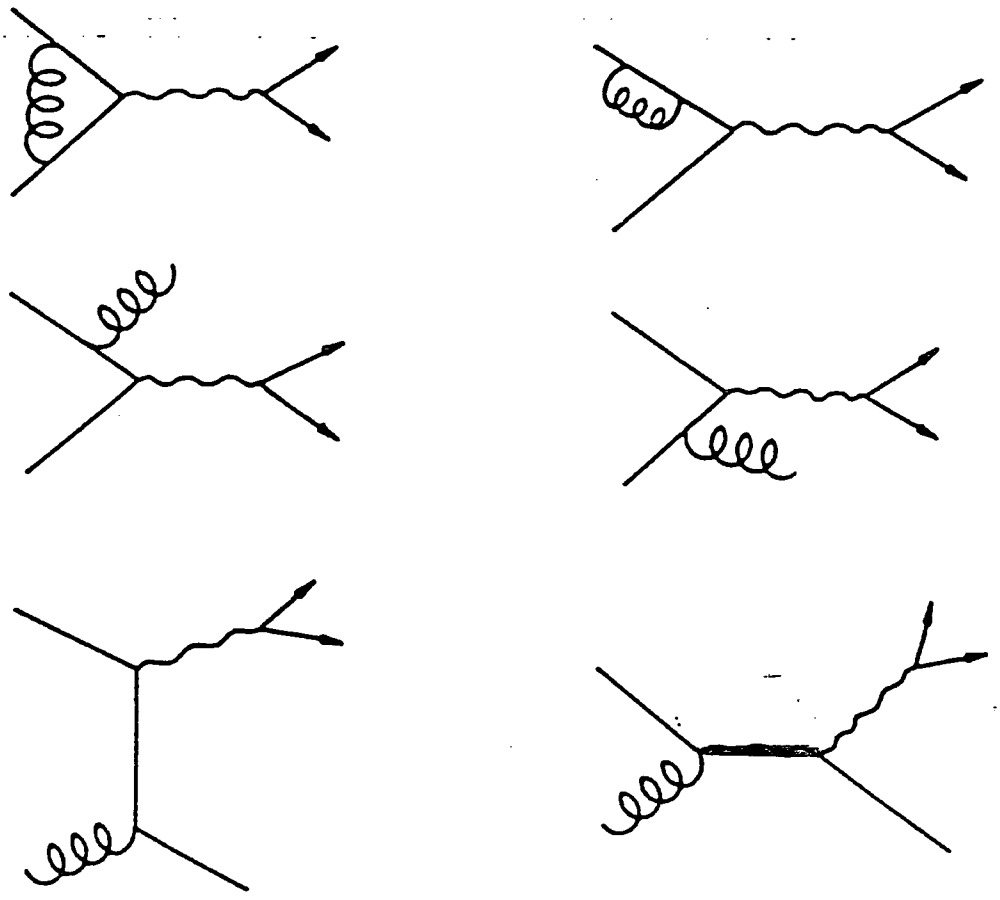

Figure 7.2 Lowest-order QCD corrections to the Drell-Yan process.

to be constant, and which we optimize to obtain the best possible fit. That is to say, we will allow ourselves a free normalization and fit solely to the *shape* of the data.

7.3 Fitting to the E605 Drell-Yan Data

The data we use is that of the E605 collaboration [70]

Our procedure for examining the variation of the χ^2 to the data with respect to the shape of the sea quark distribution will be similar to that employed in the $\Lambda_{\overline{\rm MS}} - \eta_g$ dependence of the prompt photon data. In this case, we shall explore variations in both the shape and magnitude of xSea by producing contour plots

versus the parameters A_S and η_S in

$$x\text{Sea} = A_S x^{\delta_S}(1-x)^{\eta_S} \ , \tag{7.9}$$

i.e. for each (A_S, η_S) pair, we produce a next-to-leading order theoretical prediction (with the subtlety previously mentioned—that we optimize the quality of the fit with respect to a free normalization factor, K').

For each of the two (E- and B-type) sets, we can show the results as eight contour plots in the $A_S - \eta_S$ plane showing the χ^2 components to (see Figures 7.3(a–h) and 7.4(a–h)):

(a) the $F_2^{\mu p}$ data

(b) all the $F_2^{\mu n}/F_2^{\mu p}$ data

(c) the sum of the $F_2^{\nu N}$ and the $xF_3^{\nu N}$ data

(d) the sum of (a)–(c)

(e) (same as (d))

(f) the E605 Drell-Yan data

(g) the grand total: the sum of the Drell-Yan data and the DIS data χ^2's

(h) this plot shows the variation in K'_{opt}—the 'normalization' which minimizes the χ^2 to the E605 Drell-Yan data

The star on each plot shows the position of the fit that we decided gave the optimal description of all the data.

Starting with the E-type contour plots (Figure 7.3), we see that the optimal fit gives an excellent decription of *all* the individual sets of data. There is a pronounced positive $A_S - \eta_S$ correlation for all the DIS components. The form of the total of all the DIS components is dominated by the form of the DIS(ν) component (because of its large number of points and because the other components are broadly in agreement). The plot of the E605 χ^2, somewhat surprisingly at first, has an almost 'vertical' valley showing very little dependence through more than a fourfold increase in A_S at a constant η_S of about 11. We will discuss this later on in this section. We also see that the value of K'_{opt} is close to unity as we

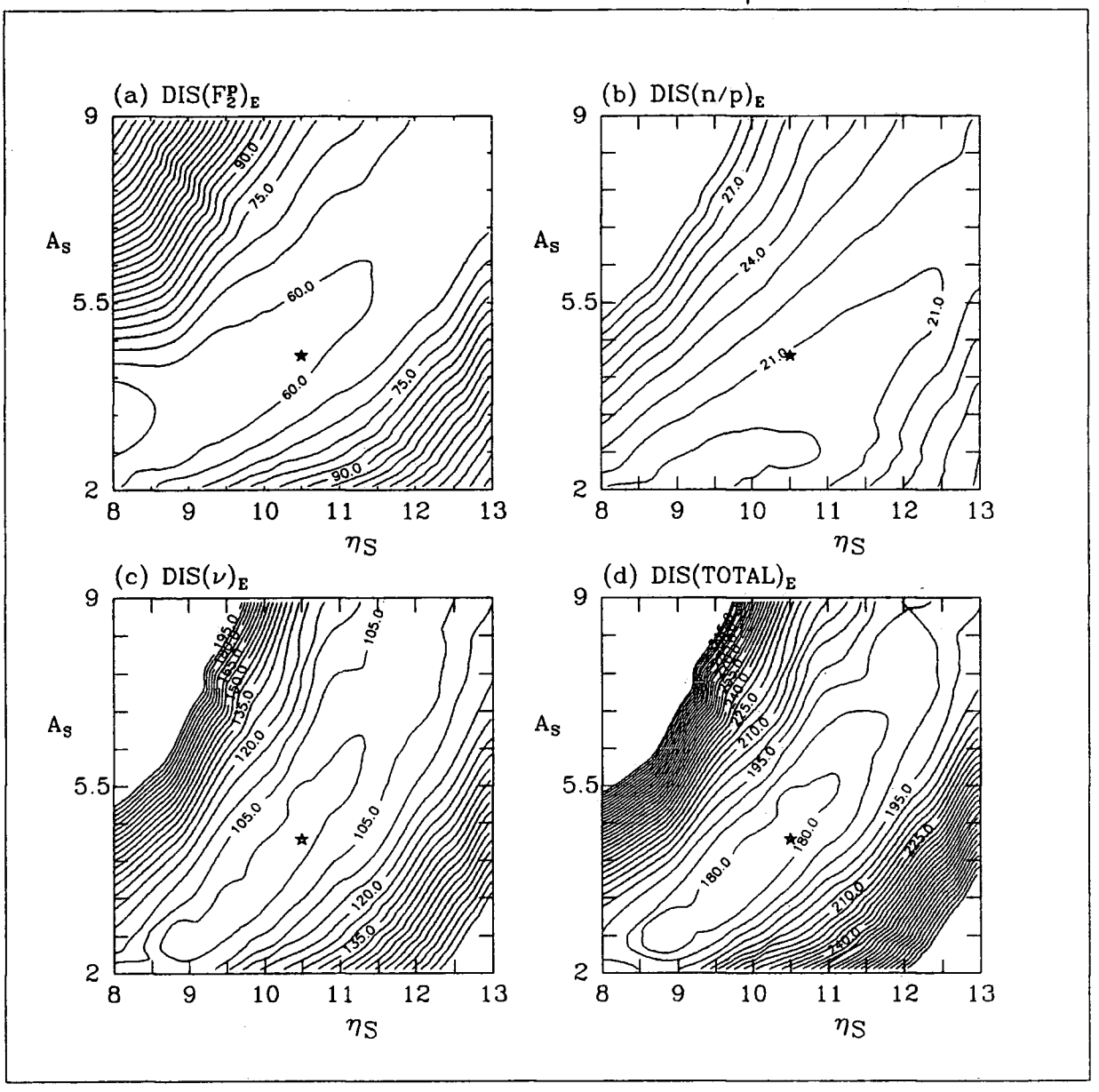

Figure 7.3 Components of the total χ^2 obtained by globally fitting to EMC $F_2^{\mu p}$ [32], $F_2^{\nu N}$ and $xF_3^{\nu N}$ [36], and $F_2^{\mu n}/F_2^{\mu p}$ [40], [42], [43] data over a range of A_S and η_S. The contour interval is five units in (a), (c) and (d) and one unit in (b). (a) shows the χ^2 to the $F_2^{\mu p}$ data, (b) shows the total χ^2 to all three sets of $F_2^{\mu n}/F_2^{\mu p}$ data, (c) shows the χ^2 to the $F_2^{\nu N}$ and $xF_3^{\nu N}$ data and (d) shows the total χ^2 to all the deep-inelastic scattering data (the sum of (a), (b) and (c). All statistical and systematic errors have been combined in quadrature. The EMC $F_2^{\mu p}$ data were renormalized upwards by 8% and those of BCDMS downwards by 2%. The neutrino data were corrected for the "EMC effect" according to Equation (4.6) (see, also, Figure 4.3). The significance of the stars is explained overleaf.

would have expected. The mean value of K_0 for this fit is 1.51, increasing slowly with $\sqrt{\tau}$.

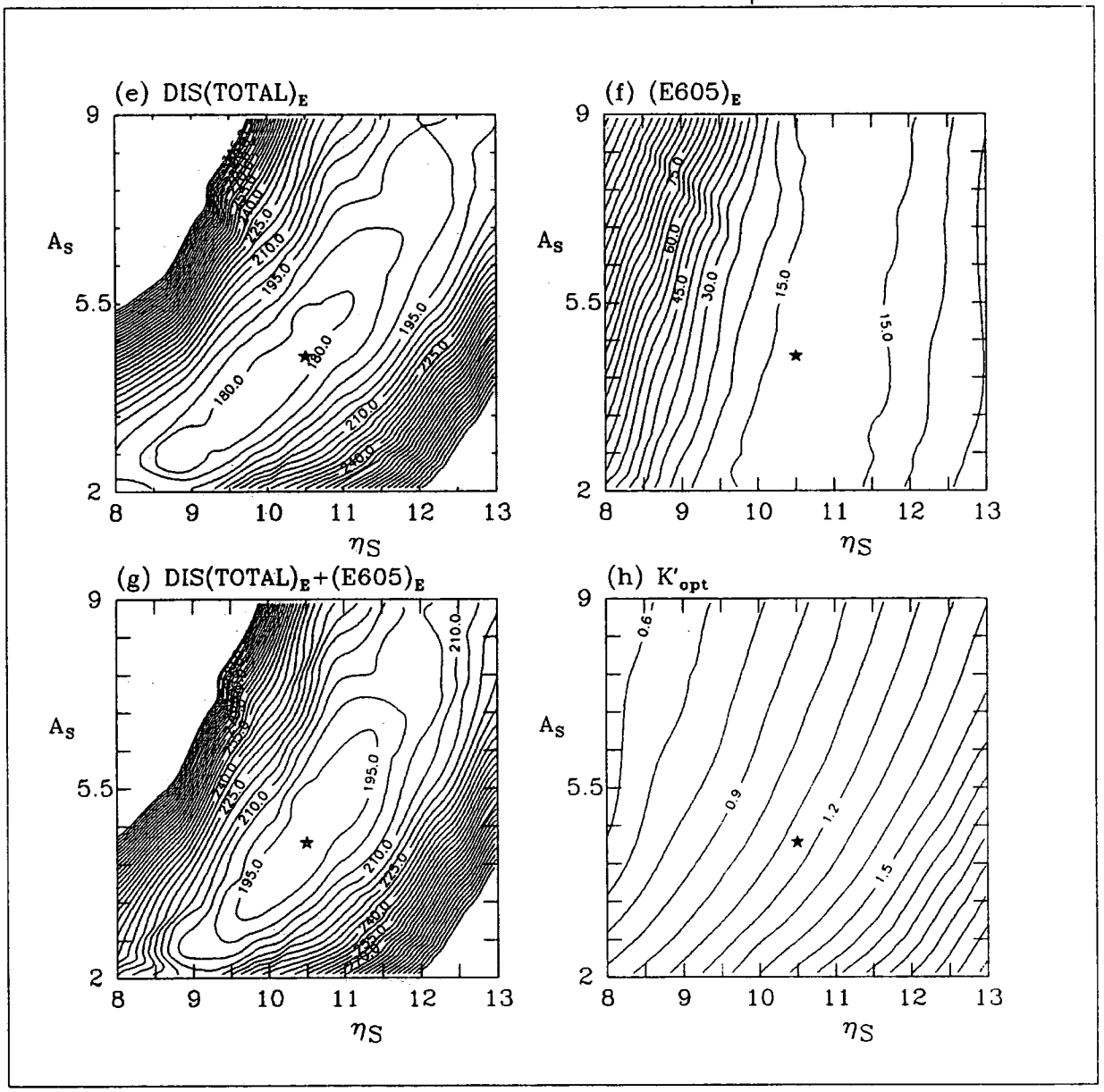

Figure 7.3 (continued) (e) is the total χ^2 obtained by globally fitting to EMC $F_2^{\mu p}$ [32], $F_2^{\nu N}$ and $xF_3^{\nu N}$ [36], and $F_2^{\mu n}/F_2^{\mu p}$ [40], [42], [43] data over a range of A_S and η_S and is the same as Figure 7.3(d). (f) shows contours of constant χ^2 where χ^2 is a measure of the quality of the theoretical prediction for the E605 Drell-Yan data [70] using the various sets of parton distributions obtained by fitting to the deep-inelastic scattering data. Each prediction was optimized by multiplication by a factor, K'. (g) shows the sum of (e) and (f) and demonstrates the quality of the overall description of the deep-inelastic and Drell-Yan data. (h) indicates the values of K' which minimized the χ^2 of the theoretical prediction to the E605 Drell-Yan data. The stars in these Figures and Figures 7.3(a–d) indicate the A_S and η_S values of the optimum overall fit.

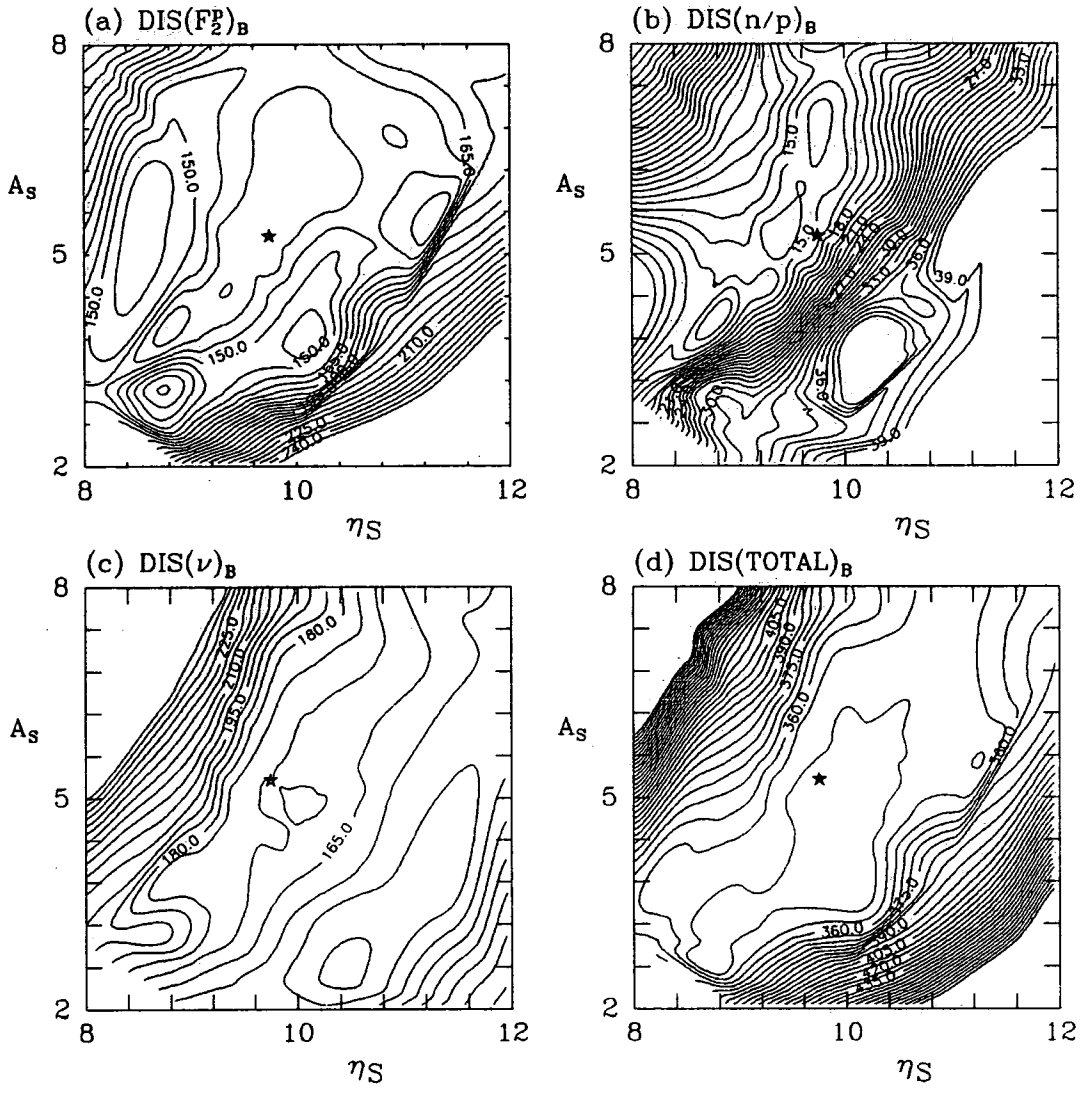

Figure 7.4 Components of the total χ^2 obtained by globally fitting to BCDMS $F_2^{\mu p}$ [16], $F_2^{\nu N}$ and $xF_3^{\nu N}$ [36], and $F_2^{\mu n}/F_2^{\mu p}$ [40], [42], [43] data over a range of A_S and η_S. The contour interval is five units in (a), (c) and (d) and one unit in (b). (a) shows the χ^2 to the $F_2^{\mu p}$ data, (b) shows the total χ^2 to all three sets of $F_2^{\mu n}/F_2^{\mu p}$ data, (c) shows the χ^2 to the $F_2^{\nu N}$ and $xF_3^{\nu N}$ data and (d) shows the total χ^2 to all the deep-inelastic scattering data (the sum of (a), (b) and (c). All statistical and systematic errors have been combined in quadrature. The EMC $F_2^{\mu p}$ data were renormalized upwards by 8% and those of BCDMS downwards by 2%. The neutrino data were corrected for the "EMC effect" according to Equation (4.6) (see, also, Figure 4.3). The significance of the stars is explained overleaf.

The situation for the B-type fit looks much less straightforward and one may wonder how the messy plots 7.4(a–c) could arise. The fitting program, however,

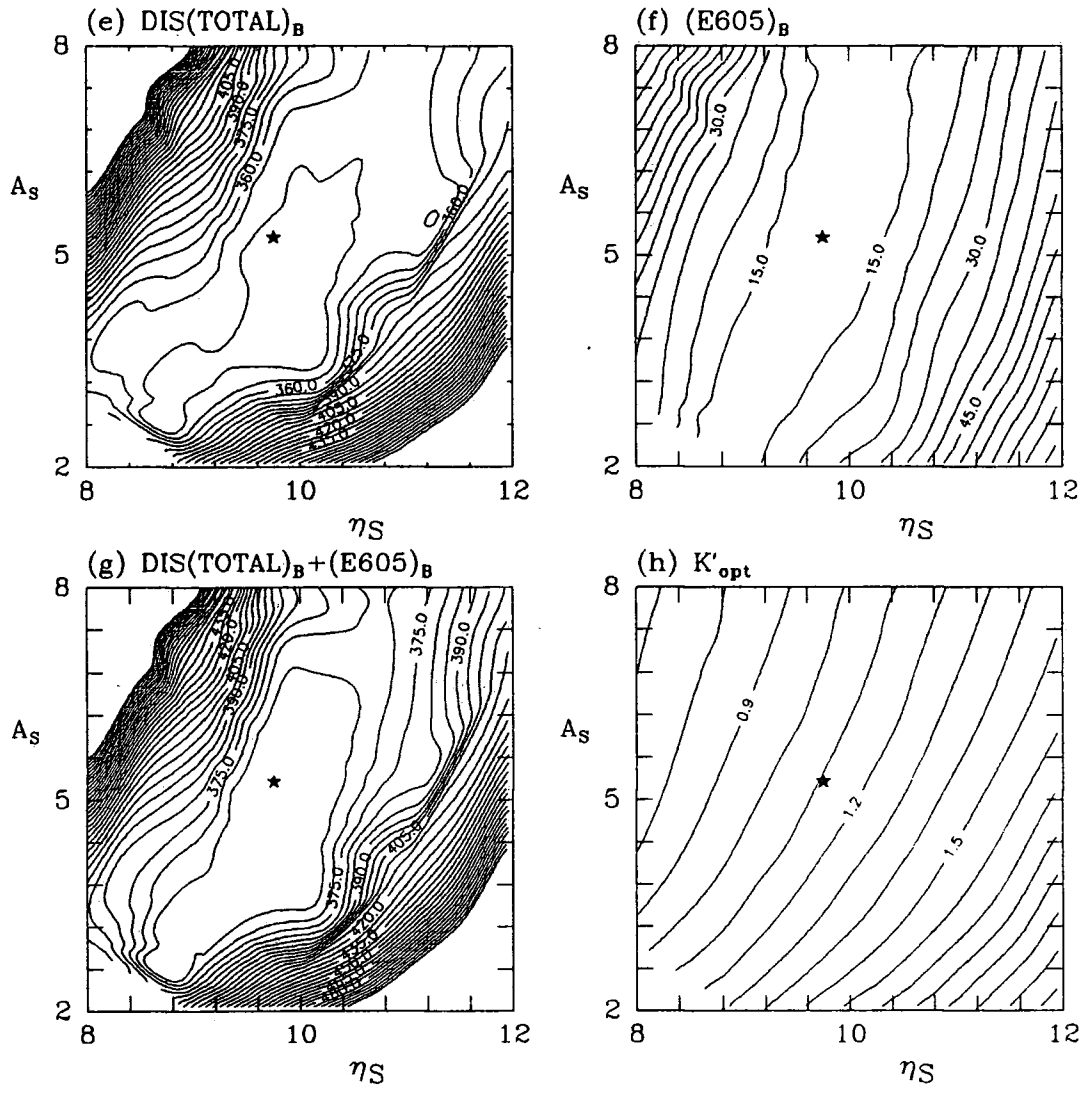

Figure 7.4 (continued) (e) is the total χ^2 obtained by globally fitting to BCDMS $F_2^{\mu p}$ [16], $F_2^{\nu N}$ and $xF_3^{\nu N}$ [36], and $F_2^{\mu n}/F_2^{\mu p}$ [40], [42], [43] data over a range of A_S and η_S and is the same as Figure 7.4(d). (f) shows contours of constant χ^2 where χ^2 is a measure of the quality of the theoretical prediction for the E605 Drell-Yan data [70] using the various sets of parton distributions obtained by fitting to the deep-inelastic scattering data. Each prediction was optimized by multiplication by a factor, K'. (g) shows the sum of (e) and (f) and demonstrates the quality of the overall description of the deep-inelastic and Drell-Yan data. (h) indicates the values of K' which minimized the χ^2 of the theoretical prediction to the E605 Drell-Yan data. The stars in these Figures and Figures 7.4(a–d) indicate the A_S and η_S values of the optimum overall fit. The statistical and systematic errors of all data have been combined in quadrature.

only 'knows' about the total DIS χ^2 shown in Figure 7.4(d) which is relatively

tidy. Again, this shows a positive $A_S - \eta_S$ correlation. The χ^2 to the E605 Drell-Yan data in Figure 7.4(f) doesn't have quite such a vertical valley as the E-fit and the minimum overlaps that of the DIS total. The resultant χ^2 in Figure 7.4(g) shows quite a large area of minimum but, in this case, there is no one point which is an approximate minimum of all the components. We therefore choose an optimal point with a degree of subjectivity. Our choice, marked with a star, is influenced by our desire to fit well the $F_2^{\mu n}/F_2^{\mu p}$ data. In Figure 7.4(h), we again see a reassuringly reasonable value of $K'_{\rm opt}$, close to unity. The mean value of K_0 for this optimum fit is 1.62.

In Figure 7.5(a), we show a range of seas of the E-type fits at some DIS average of $Q^2 = 40$ GeV^2 . We have taken the fits at the four corners of the $A_S - \eta_S$ space, shown in Figure 7.3, plus the optimal fit. The lines are labelled 'TR' for the top-right hand corner of the plot, 'BL' for the bottom-left etc. The optimal fit is labelled 'HE'. Note that this spread in shapes is perhaps not as great as might have been expected due to two factors: the Q_0^2 differences tend to get 'washed out' as Q^2 increases; and we still have one xSea parameter, δ_S, which is free in the fitting to the DIS data. Here, we see the reason for the observed $A_S - \eta_S$ correlation in, for example, Figure 7.3(e). If we look at the BL–HE–TR diagonal, we see that the evolved xSea lines are very similar, thus explaining the correlation. In Figure 7.5(b), we show a range of seas at some E605 average $\overline{M^2} = s\overline{\tau} = 0.1s \approx 150$ GeV^2. Figure 7.3(f) might lead us to expect that the seas of BR and TR are not too different in the range of x relevant to the Drell-Yan data, but we must remember to take the K'_{opt} factors into account: although A_S(TR)/A_S(BR)= 4.5, we also have K'_{opt}(BR)/K'_{opt}(TR)= 1.7. In addition, the parameter δ_S—left free in the minimization—is very different for the two fits and gives a factor x^{δ_S}(BR)/x^{δ_S}(TR)= $x^{-0.49}$ which varies between 3.1 and 1.4 as x goes from 0.1 to 0.5.

The full parametrization of the optimum fits (alongside the previous optimum fits to the DIS and prompt photon data) are given in Table 7.1 together with the breakdowns of the the total χ^2. We see that the inclusion of the Drell-Yan data changes the distributions very little. In fact, the B-type fit, which we denote HMRS(B), is scarcely changed from the best fit for the prompt photon and DIS data. It seems, therefore, that we have good consistency between the various

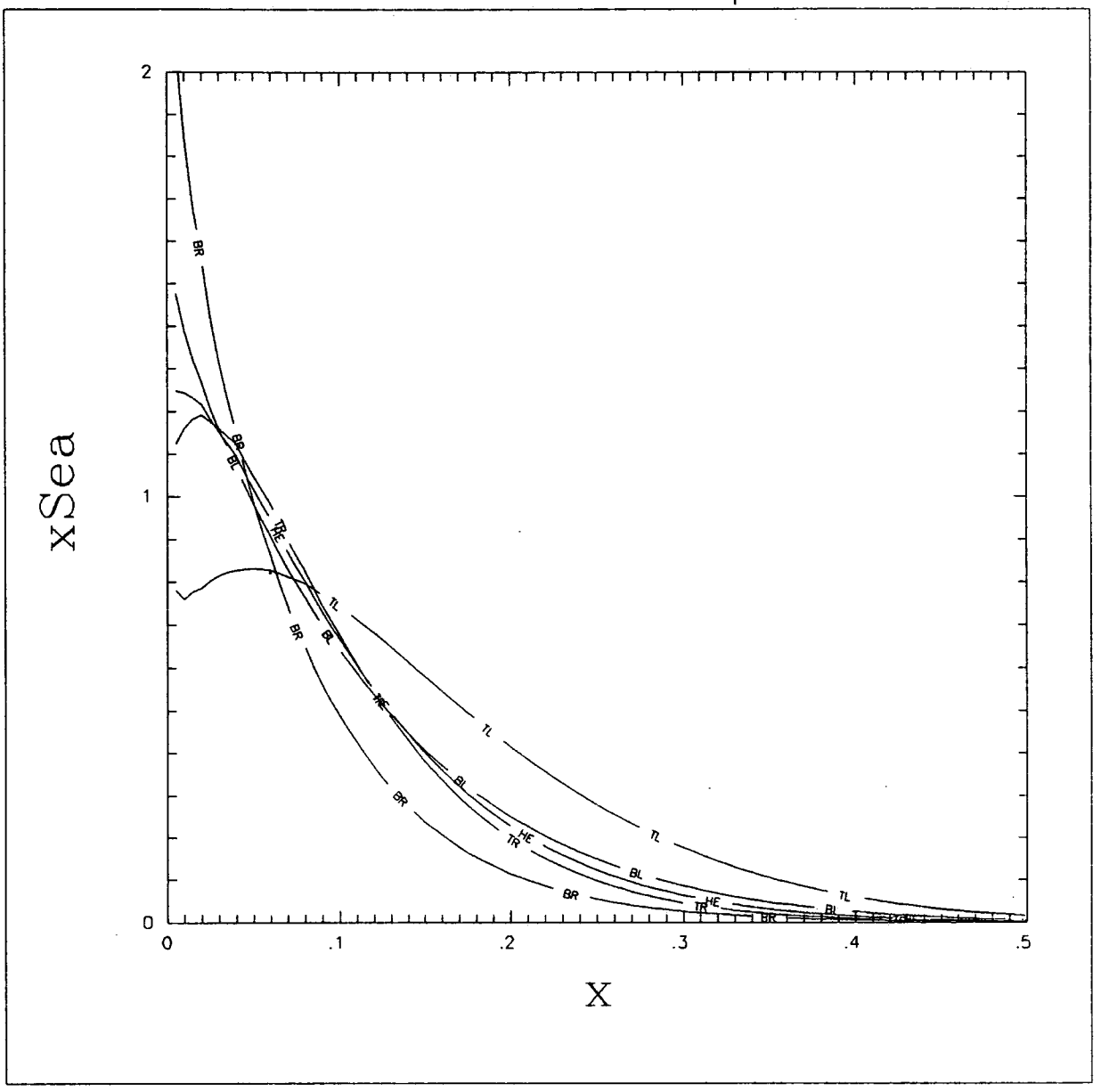

Figure 7.5(a) A range of seas of the fits to all the deep-inelastic scattering that included the EMC $F_2^{\mu p}$ data [32] evolved to $Q^2 = 40$ GeV^2 —typical of the deep-inelastic data. Sea is defined by xSea$= 2x(\overline{u} + \overline{d} + \overline{s})$. We show the seas of the fits at the four corners of the $A_S - \eta_S$ space, shown in Figure 7.3, plus the optimal fit. The lines are labelled 'TR' for the top-right hand corner of the plot, 'TL' for the top-left, 'BR' for the bottom-right, and 'BL' for the bottom-left. 'Top' corresponds to high A_S and 'right' to high η_S. The optimal fit is labelled 'HE'.

data sets.

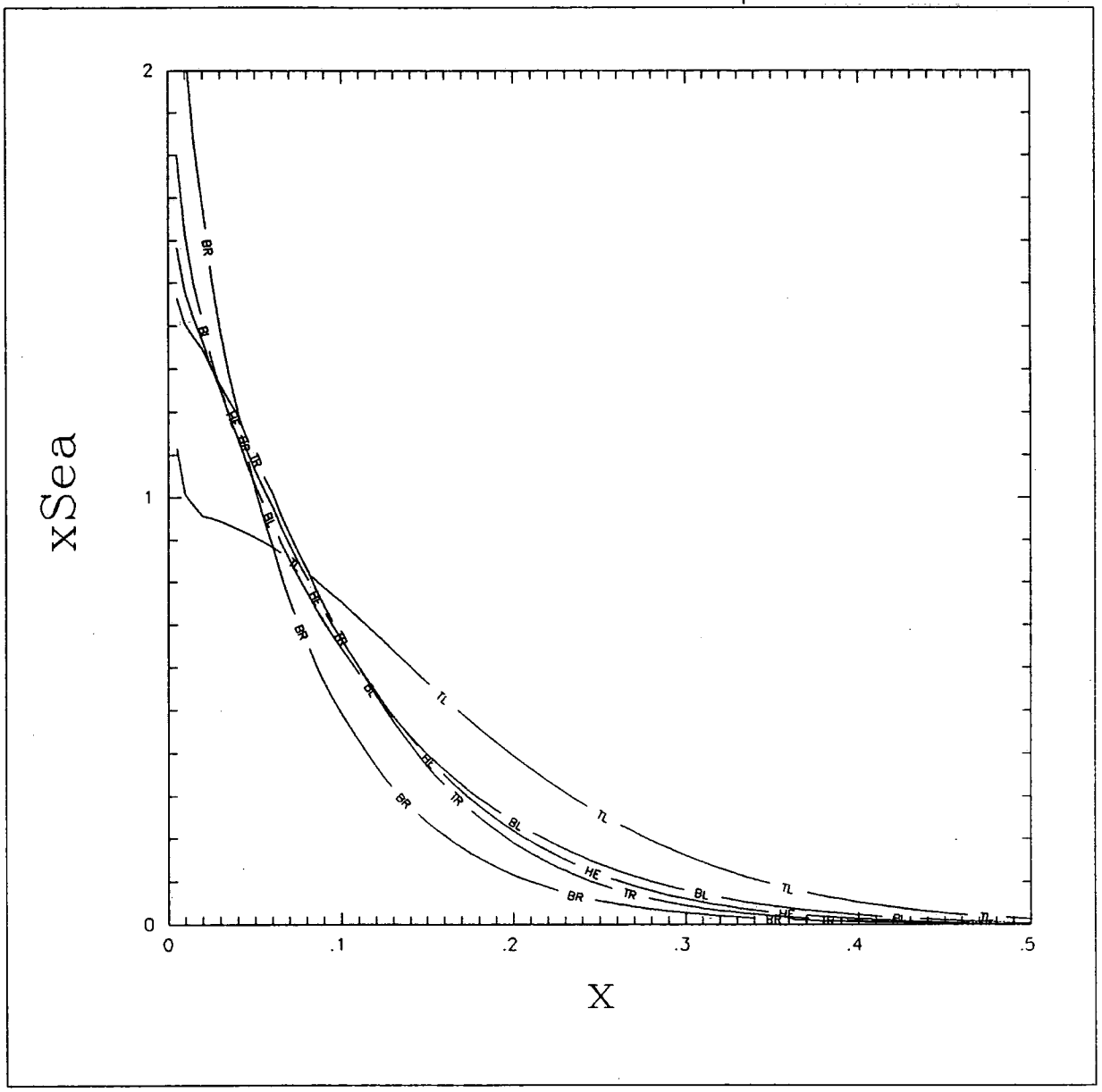

Figure 7.5(b) A range of seas of the fits to all the deep-inelastic scattering that included the EMC $F_2^{\mu p}$ data [32] evolved to an M^2 typical of the E605 Drell-Yan data: $\overline{M^2} = s\overline{\tau} = 0.1s \approx$ 150 GeV^2. Sea is defined by xSea$= 2x(\overline{u}+\overline{d}+\overline{s})$. We show the seas of the fits at the four corners of the $A_S - \eta_S$ space, shown in Figure 7.3, plus the optimal fit. The lines are labelled 'TR' for the top-right hand corner of the plot, 'TL' for the top-left, 'BR' for the bottom-right, and 'BL' for the bottom-left. 'Top' corresponds to high A_S and 'right' to high η_S. The optimal fit is labelled 'HE'.

	with EMC		with BCDMS	
	+PP	+PP+DY	+PP	+PP+DY
$\Lambda_{\overline{MS}}$ (MeV)	100	100	190	190
η_g	4.4	4.4	5.1	5.1
η_1	0.357	0.352	0.224	0.237
η_2	4.07	4.08	4.06	4.07
γ_{ud}	10.0	10.6	26.6	23.8
η_3	0.608	0.607	0.411	0.426
η_4	4.82	4.83	4.81	4.82
γ_d	1.13	1.26	7.05	6.32
A_S	3.22	4.50	5.35	5.25
δ_S	0.270	0.359	0.404	0.401
η_S	9.45	10.5	9.87	9.75
N_{ud}	1.264	1.216	0.4893	0.5469
N_d	1.754	1.735	0.6384	0.6957
A_g	2.614	2.622	2.856	2.855
P(u_V)	26.4%	26.5%	26.2%	26.2%
P(d_V)	10.6%	10.7%	10.7%	10.7%
P(S)	14.5%	14.2%	16.2%	16.3%
P(g)	48.4%	48.5%	46.8%	46.8%
Data [# Points]	χ^2 values			
$F_2^{\mu p}$ (EMC,BCDMS)[88,142]	58.1	58.6	163.8	163.8
F_2^{ν} (CDHSW) [84]	27.0	25.8	52.9	54.6
xF_3^{ν} (CDHSW) [94]	71.3	73.0	116.3	115.4
$F_2^{\mu n}/F_2^{\mu p}$ (BCDMS) [11]	5.9	6.2	9.2	8.7
$F_2^{\mu n}/F_2^{\mu p}$ (EMC) [10]	4.1	4.1	2.9	2.8
$F_2^{\mu n}/F_2^{\mu p}$ (NMC) [11]	10.3	10.6	4.3	4.1
DIS(total) [298,352]	**176.7**	**178.3**	**349.3**	**349.3**
Prompt Photon (WA70) [8]	7.2	7.2	7.3	7.3
Drell-Yan (E605) [8]	(19.2)	12.4	(12.0)	11.8
Total [314,368]	**203.1**	**197.9**	**368.6**	**368.4**

Table 7.1 The upper portion of the table lists the parameter values of the $Q_0^2 = 4$ GeV^2 parametrization of the optimum fits to the deep-inelastic and prompt photon data (columns headed '+PP') and the overall optimum fits after the consideration of the Drell-Yan data (columns headed '+PP+DY'). The headings 'with EMC' and 'with BCDMS' refer to the collaboration whose $F_2^{\mu p}$ data was used in the fits. We also list the values of the quark distributions' pre-factors N_{ud} and N_d, which are determined by the condition that there are two valence u quarks and one valence d quark in the proton, and the gluon pre-factor A_g which is determined by total momentum conservation. In addition, we give the percentage of the total proton momentum carried by each parton distribution at $Q^2 = 4$ GeV^2 . The lower part of the table shows the contribution to the total χ^2 coming from each data set. The figures in brackets in the Drell-Yan row are given for information since the fits in these columns did not involve the Drell-Yan data. The values of K'_{opt} for these fits are 1.06 ('with EMC') and 0.96 ('with BCDMS').

8. The Final Parton Distributions

8.1 Graphical Comparison with the Data

We denote our final parton distributions HMRS(E) (for those determined using the EMC $F_2^{\mu p}$ data) and HMRS(B) (determined using the BCDMS $F_2^{\mu p}$ data). In Figures 8.1—8.6, we show, graphically, the agreement between the predictions of our distributions and the experimental data that we used. HMRS(E) is shown by the continuous lines and HMRS(B) by the dashed ones. In both cases, we see that there is a very good description of the data.

In Figure 8.1(a), we see an exceptionally impressive fit to the BCDMS $F_2^{\mu p}$ data, in view of the very small errors on those data. However, the theory lines do systematically undershoot the data at $x = 0.65$ and $x = 0.75$. This is probably because all the data sets tend to have larger errors at high x and so this region is the one which inevitably bears the brunt of any ill-fitting. Figure 8.1(b) shows the comparison between the predicted and measured 'scaling violations' $\partial \ln F_2 / \partial \ln Q^2$.

This same feature is seen in the HMRS(E) fit to the EMC $F_2^{\mu p}$ data in Figure 8.1(c) which, otherwise, is a very satisfactory fit (as was to be expected with the relatively large errors on the data). Figure 8.1(d) shows the scaling violations.

Both sets give χ^2 values per point of less than unity in the fits to the CDHSW $F_2^{\nu N}$ data in Figure 8.2(a) although HMRS(E) gives a χ^2 less than half that of HMRS(B). It is apparent that the magnitude of the slope of the HMRS(B) fit (and we use the word 'slope' here because all the fits are essentially linear, i.e. $\partial \ln F_2(x, Q^2) / \partial \ln Q^2 = const.(x)$). is greater than that of the HMRS(E) fit at all values of x. This is a reflection of the higher value of $\Lambda_{\overline{\rm MS}}$ which implies a higher α_s (to which $\partial \ln F_2(x, Q^2) / \partial \ln Q^2 = const.(x)$ is proportional). This is seen more clearly in Figure 8.2(b).

This is also seen in the fits to the CDHSW $xF_3^{\nu N}$ data (Figure 8.3(a)). This figure is an indication of the accuracy of our theoretical values of $x(u_V + d_V)$. The agreement between theory and data is not particularly good for $x \lesssim 0.125$ for either theoretical fit although HMRS(E) fares significantly better (as we might have foreseen since HMRS(E) is constrained much less by its $F_2^{\mu p}$ data). We have

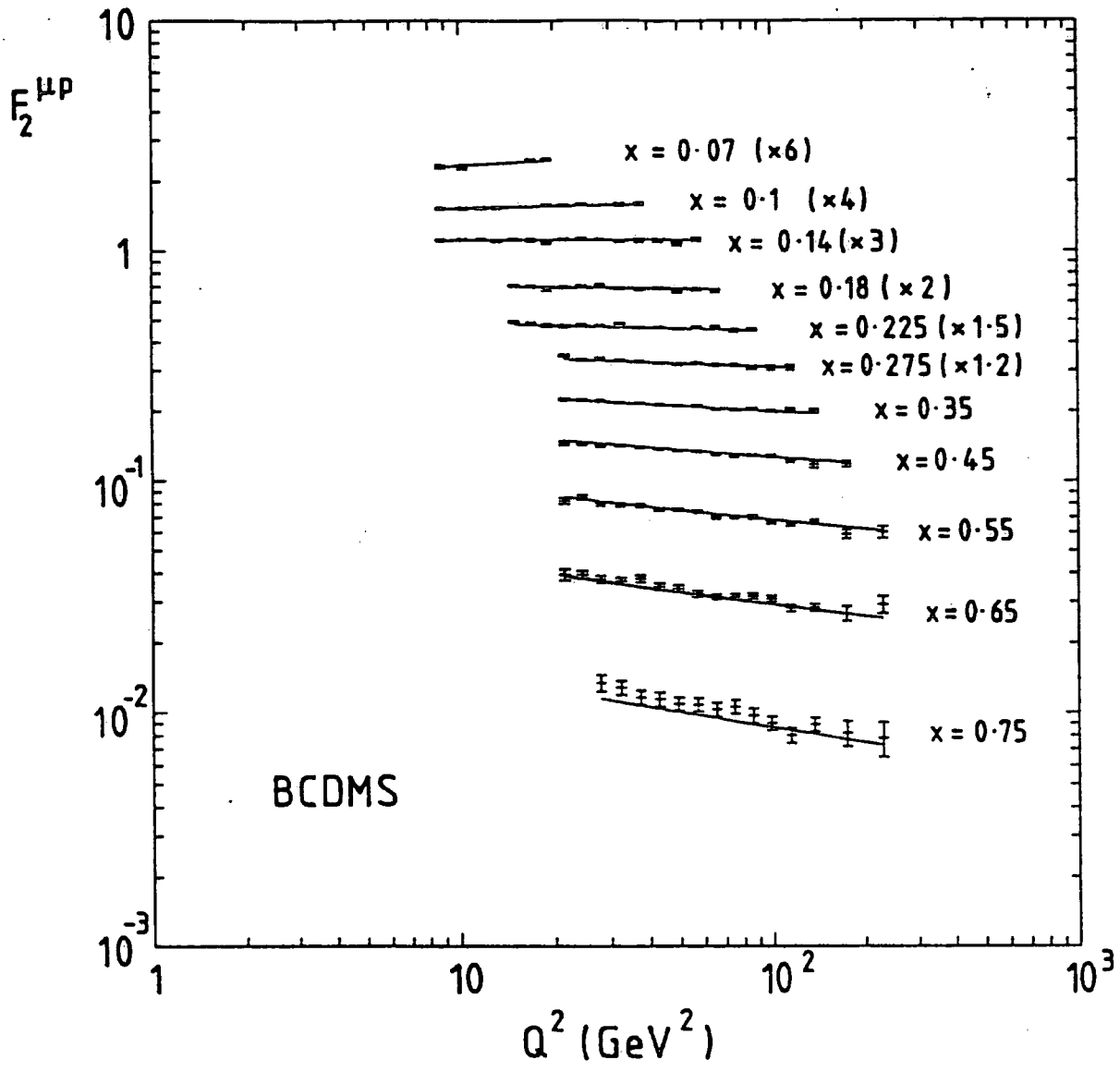

Figure 8.1(a) Data on the structure function $F_2^{\mu p}(x, Q^2)$ from the BCDMS collaboration [16] with the HMRS(B) fit. The data are renormalized downwards by 2%.

already seen, though, in §5.4, that we have reason to doubt the compatibility of the CDHSW neutrino data and the BCDMS $F_2^{\mu p}$ data. The scaling violations are shown in Figure 8.3(b).

Both HMRS(E) and HMRS(B) are, needless to say, excellent fits to the $F_2^{\mu n}/F_2^{\mu p}$ data (Figure 8.4a) since this was a 'design feature' of the analysis. Figure 8.4b, however, shows the even more impressive *disagreement* between some other, widely used, parton distributions and the new measurements of NMC.

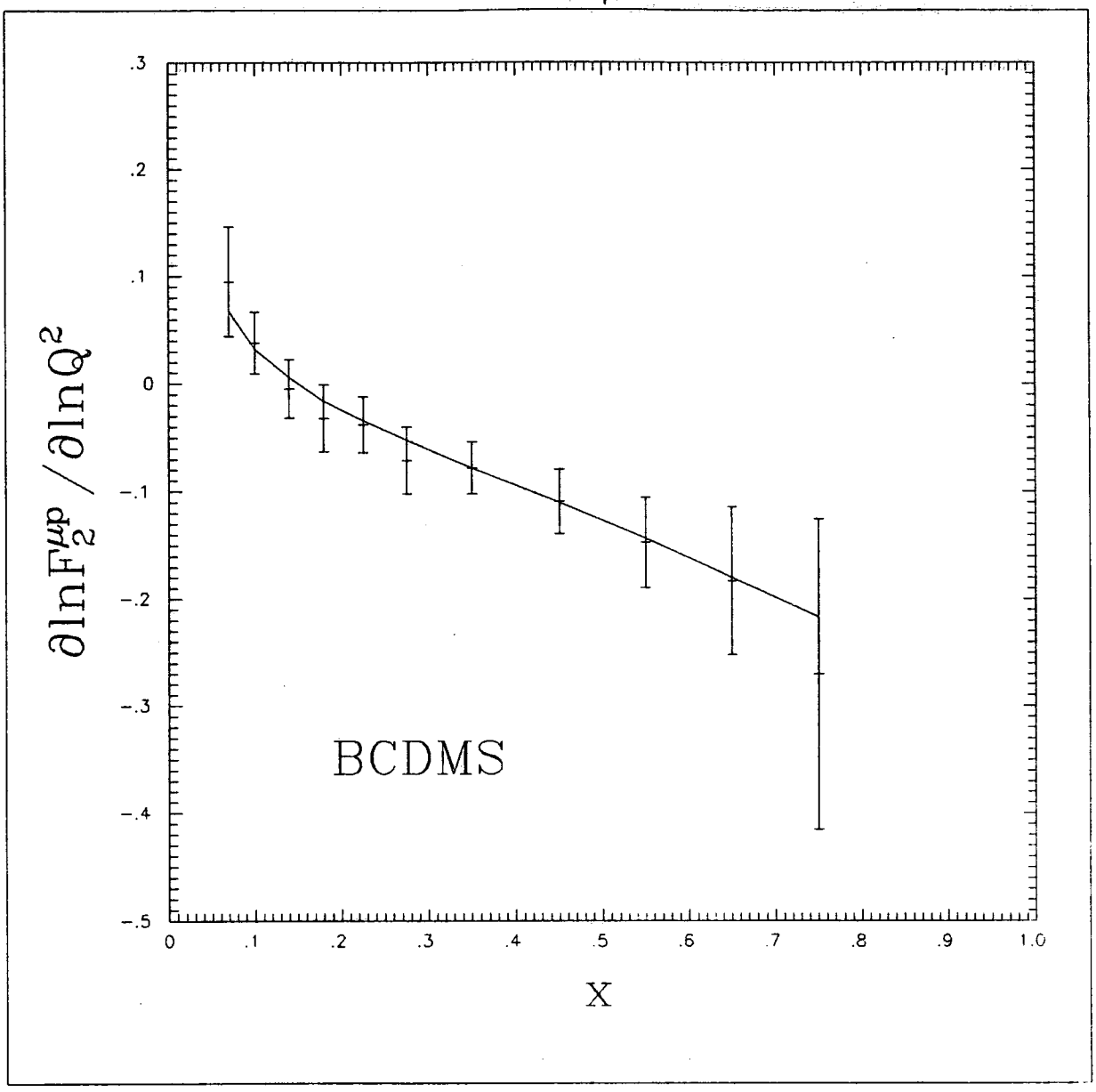

Figure 8.1(b) The 'scaling violations' of the $F_2^{\mu p}$ data of the BCDMS collaboration [16] compared with those predicted by the HMRS(B) solution. The experimental value at each x value was determined by performing a linear fit to $\ln F_2^{\mu p}$ versus $\ln Q^2$ with the gradient and intercept as free parameters and χ^2 as the value minimized (using the statistical and systematic errors added in quadrature). The errors were calculated by allowing the gradient to vary (with the intercept free) higher and lower than its optimum value such that the total χ^2 increased by one unit. The theoretical values were calculated by a least-squares fit to the theoretical prediction over the same range in Q^2.

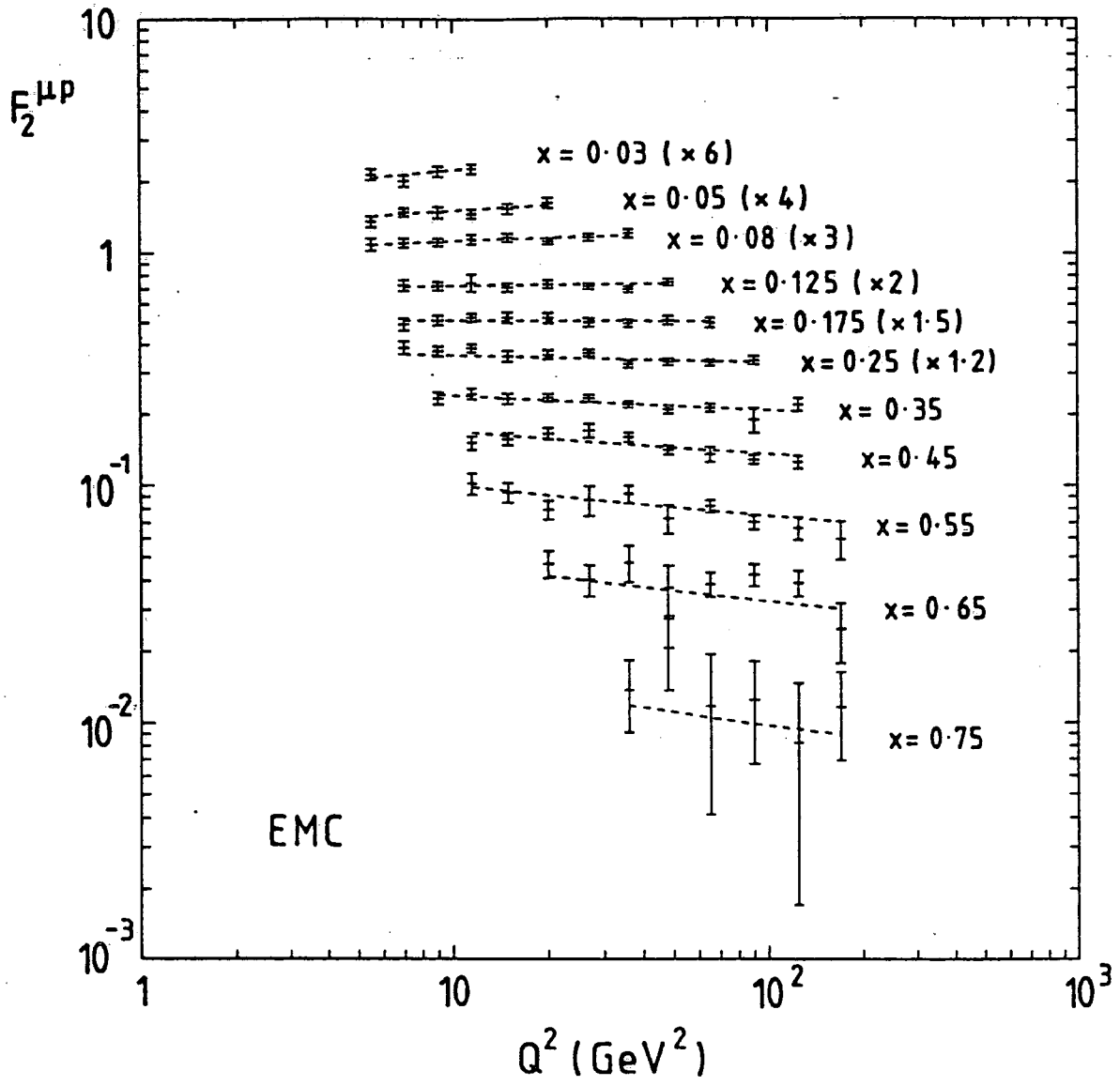

Figure 8.1(c) Data on the structure function $F_2^{\mu p}(x, Q^2)$ from the EMC collaboration [32] with the HMRS(E) fit. The data are renormalized upwards by 8%.

Clearly, these other distributions are obsolete in the light of these new data.

Figure 8.5 displays the agreement of the two fits with the WA70 prompt photon data (the fine-tuning of the sea distribution has hardly affected this as can be seen by the χ^2 values in Table 7.1). The theory lines are equally good but are quite different as a result of the softer gluon and larger $\Lambda_{\overline{\rm MS}}$ of the HMRS(B) set.

Finally, Figure 8.6 shows the excellent fit of both sets to the very accurate

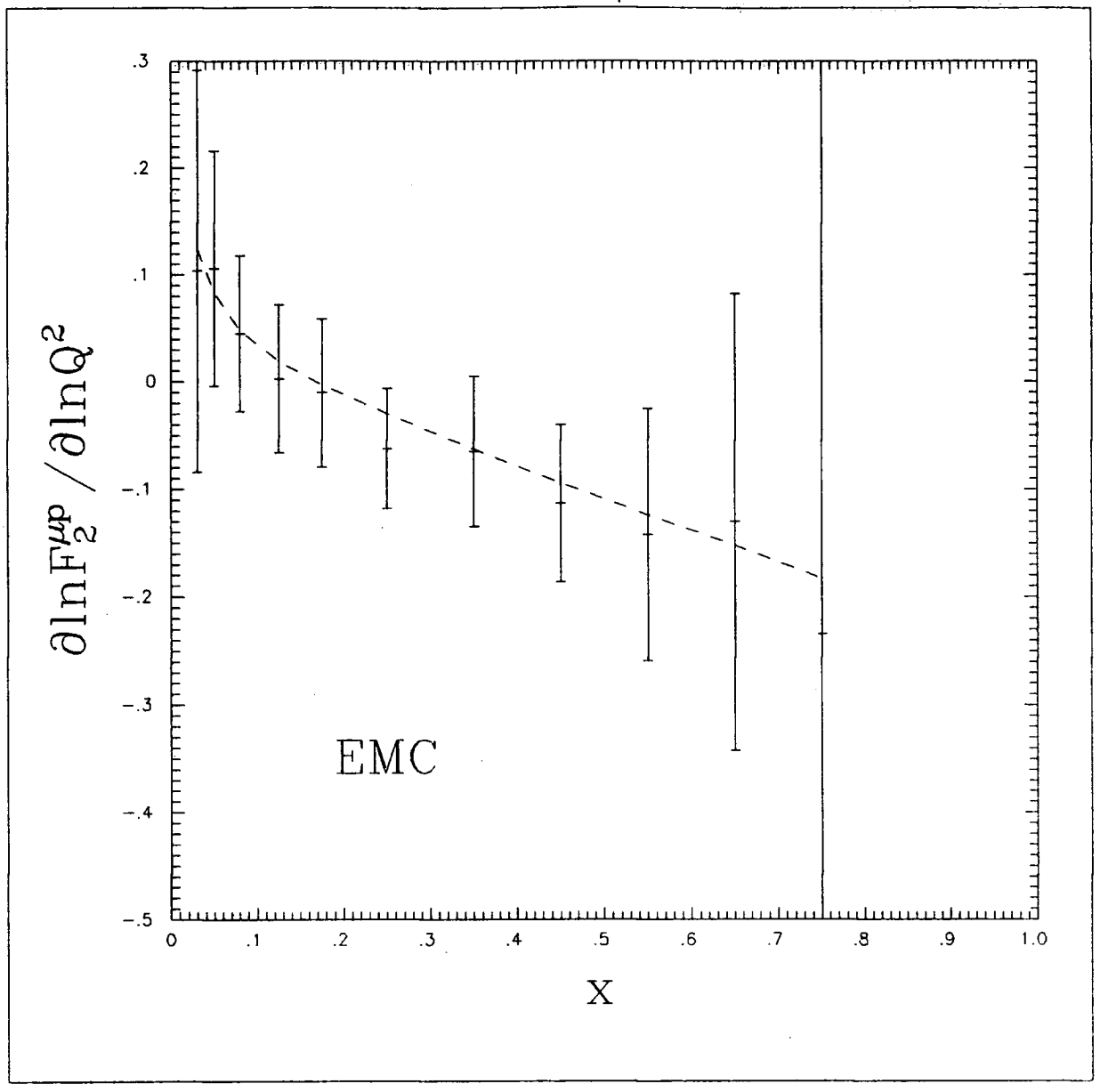

Figure 8.1(d) The 'scaling violations' of the $F_2^{\mu p}$ data of the EMC collaboration [32] compared with those predicted by the HMRS(E) solution. The experimental value at each x value was determined by performing a linear fit to $\ln F_2^{\mu p}$ versus $\ln Q^2$ with the gradient and intercept as free parameters and χ^2 as the value minimized (using the statistical and systematic errors added in quadrature). The errors were calculated by allowing the gradient to vary (with the intercept free) higher and lower than its optimum value such that the total χ^2 increased by one unit. The theoretical values were calculated by a least-squares fit to the theoretical prediction over the same range in Q^2.

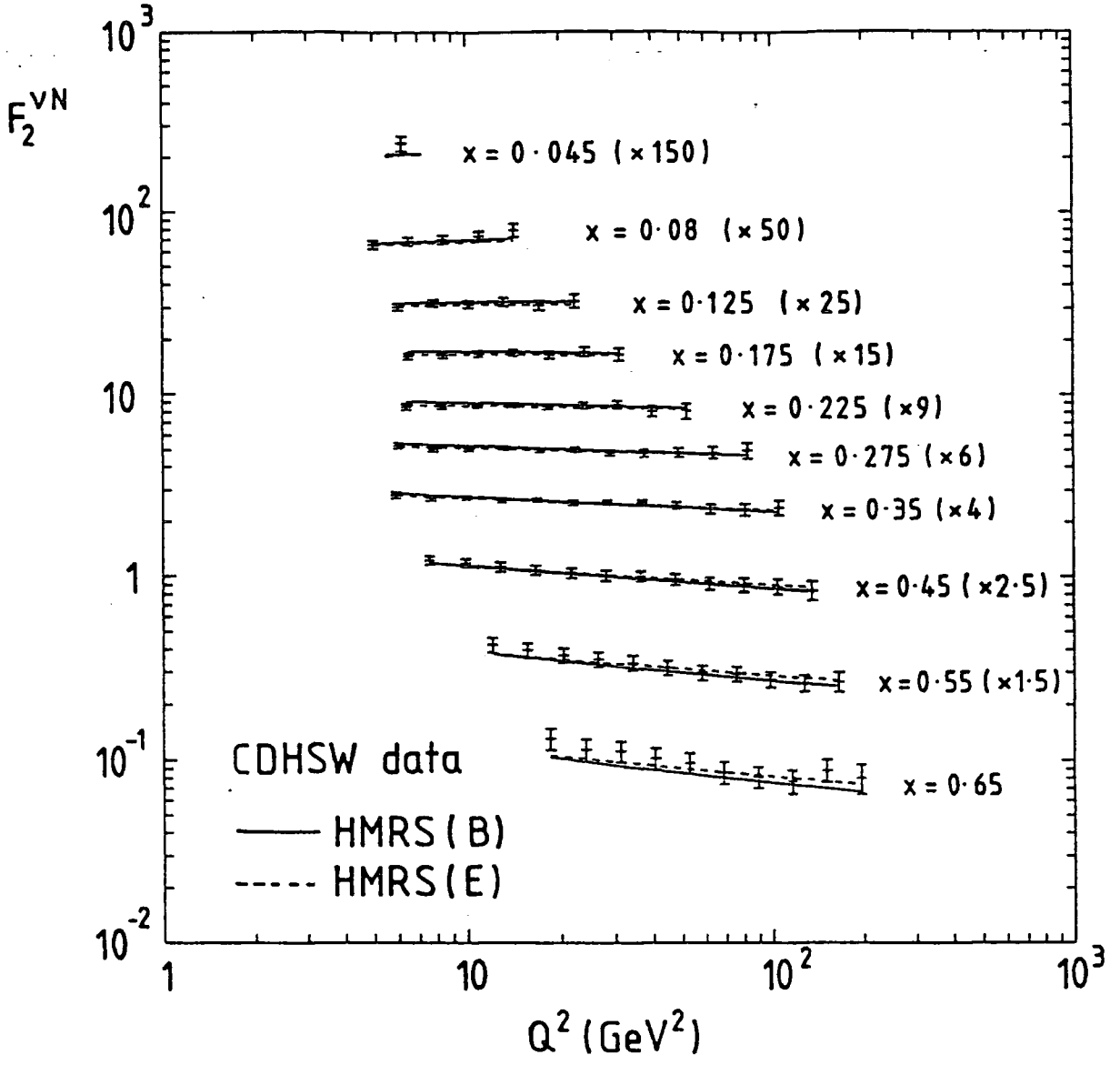

Figure 8.2(a) Data on the structure function $F_2^{\nu N}(x, Q^2)$ from the CDHSW collaboration [36], together with the HMRS(B) (continuous lines) and HMRS(E) (dashed lines) fits. The data have been corrected for the "EMC effect".

Drell-Yan data of E605.

8.2 Comparison with other Parton Distributions

Here, we compare the HMRS parton distributions with the previous best (in our opinion) next-to-leading order ones—the MRS′ distributions of [41] and also with the *leading order* ones of Duke and Owens' DO1 (Set 1, $\Lambda_{LO} = 200$ MeV) [65]. However odd the idea of this comparison of parton distributions evolved at

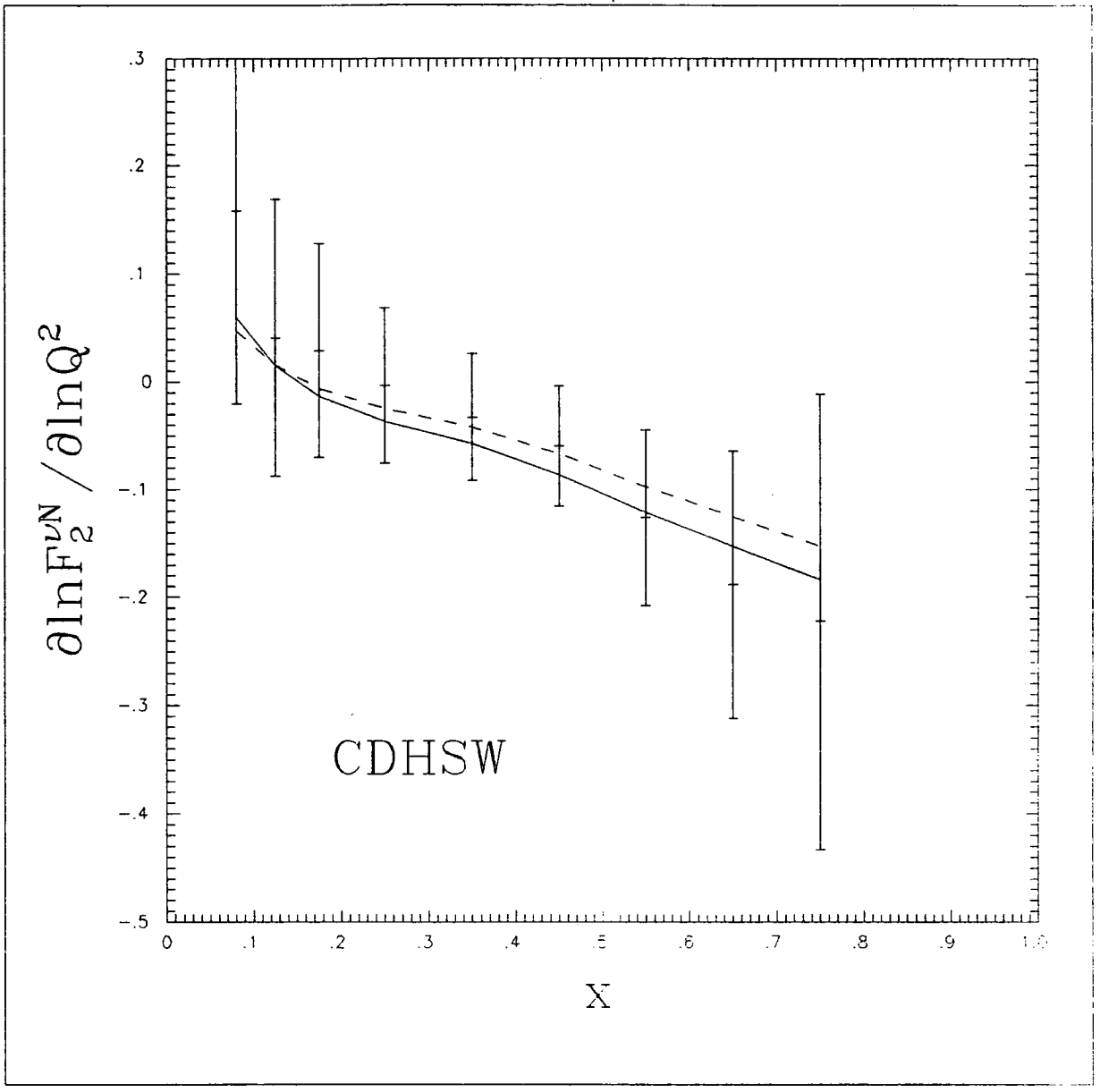

Figure 8.2(b) The 'scaling violations' of the $F_2^{\nu N}$ data of the CDHSW collaboration [36], compared with those predicted by the HMRS solutions. The experimental value at each x value was determined by performing a linear fit to $\ln F_2^{\nu N}$ versus $\ln Q^2$ with the gradient and intercept as free parameters and χ^2 as the value minimized (using the statistical and systematic errors added in quadrature). The errors were calculated by allowing the gradient to vary (with the intercept free) higher and lower than its optimum value such that the total χ^2 increased by one unit. The theoretical values were calculated by a least-squares fit to the theoretical prediction over the same range in Q^2.

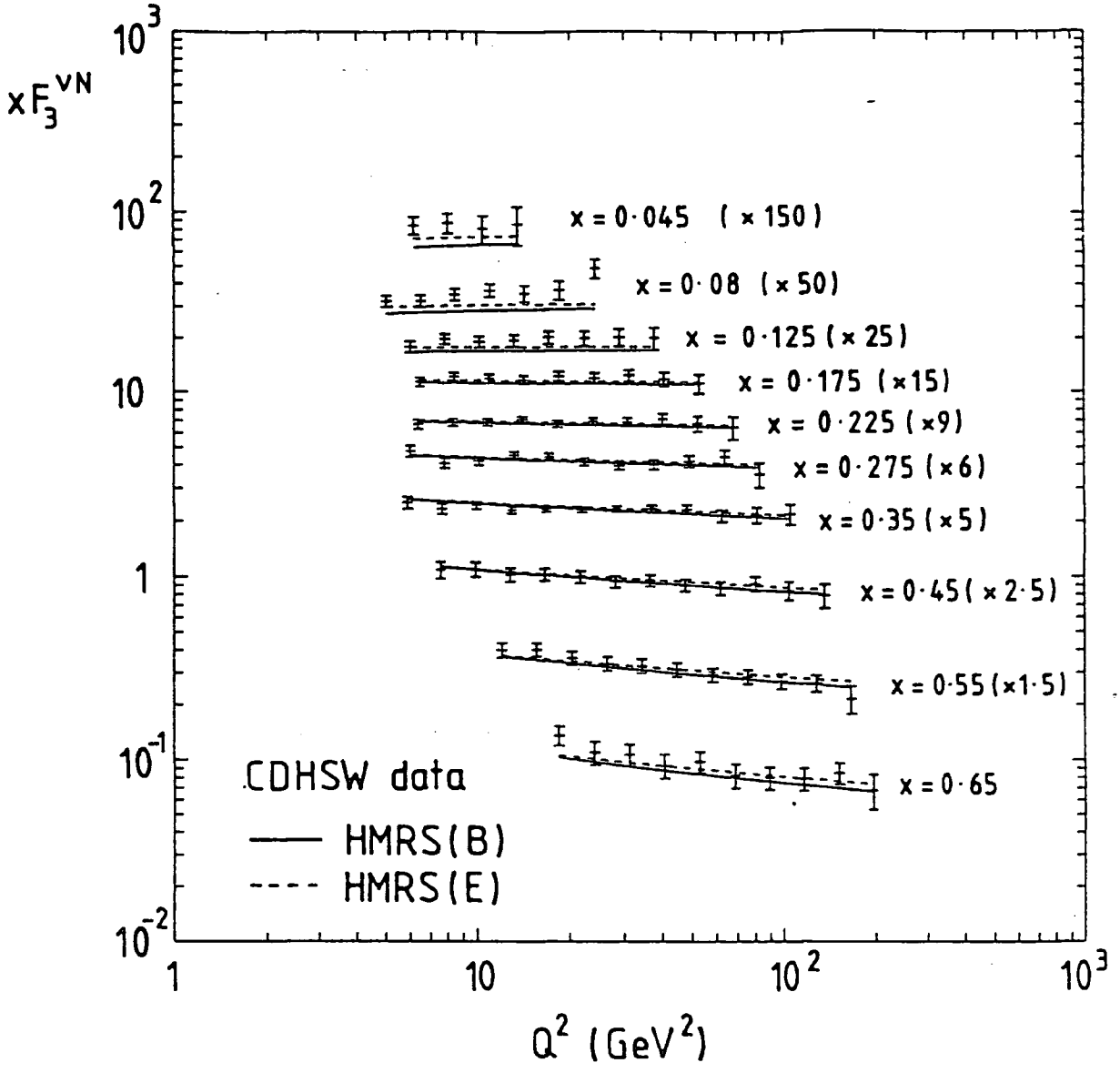

Figure 8.3(a) Data on the structure function $xF_3^{\nu N}(x, Q^2)$ from the CDHSW collaboration [36], together with the HMRS(B) (continuous lines) and HMRS(E) (dashed lines) fits. The data have been corrected for the "EMC effect".

different orders may seem, we do it because those of Duke and Owens are very widely used, regardless of the order of parton distributions that are required (and a major reason for this may be that there exists a convenient parametrization of them over all x and a wide range of Q^2—we hope, shortly, to have such a parametrization of the HMRS distributions [73]).

Figure 8.7 shows plots of xu, xd, xg, and xSea for these parton distributions

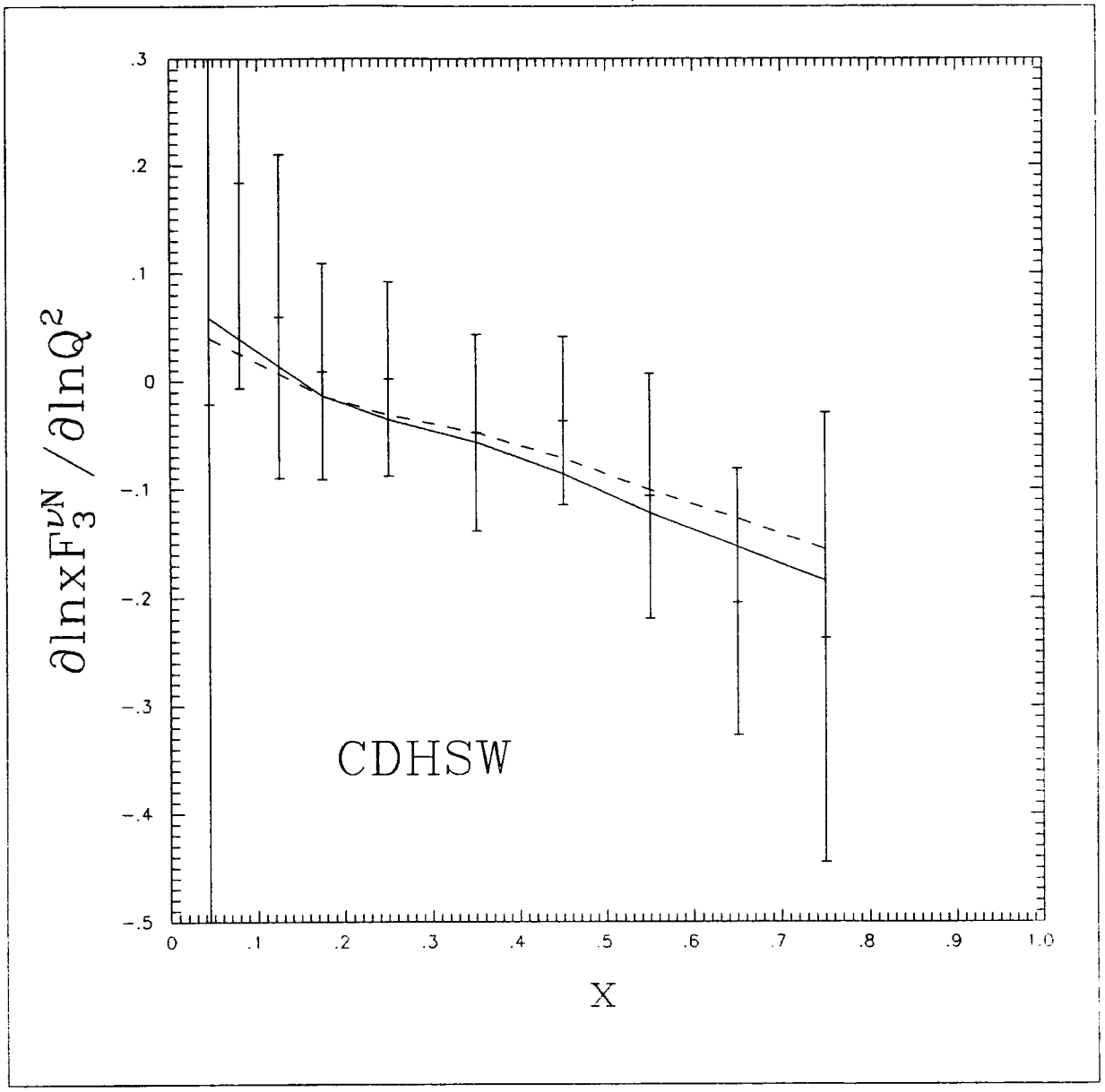

Figure 8.3(b) The 'scaling violations' of the $xF_3^{\nu N}$ data of the CDHSW collaboration [36], compared with those predicted by the HMRS solutions. The experimental value at each x value was determined by performing a linear fit to $\ln xF_3^{\nu N}$ versus $\ln Q^2$ with the gradient and intercept as free parameters and χ^2 as the value minimized (using the statistical and systematic errors added in quadrature). The errors were calculated by allowing the gradient to vary (with the intercept free) higher and lower than its optimum value such that the total χ^2 increased by one unit. The theoretical values were calculated by a least-squares fit to the theoretical prediction over the same range in Q^2.

at $Q^2 = 20$ GeV^2 . The HMRS xu and xd are dramatically different from those of Duke and Owens and it is not necessary to draw the comparisons of DO1 with

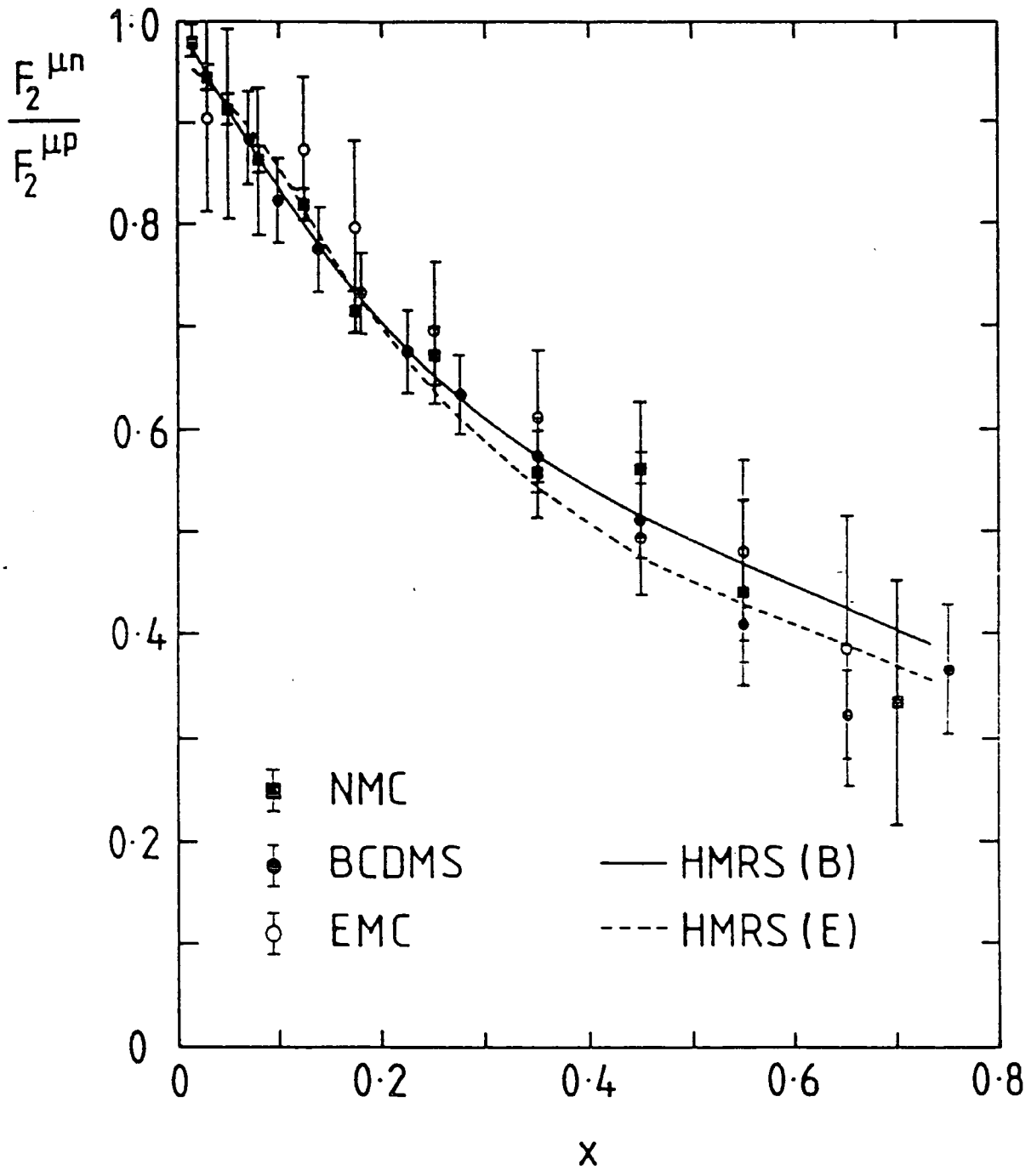

Figure 8.4(a) Data on the structure function ratio $F_2^{\mu n}/F_2^{\mu p}$ from EMC [40] (open circles), BCDMS [42] (solid circles), and NMC [43] (solid squares), together with the HMRS(B) (continuous line) and HMRS(E) (dashed line) fits.

the latest experimental data to realize that there would be a severe discrepancy. There are two main reasons for the differences between the MRS′ and HMRS

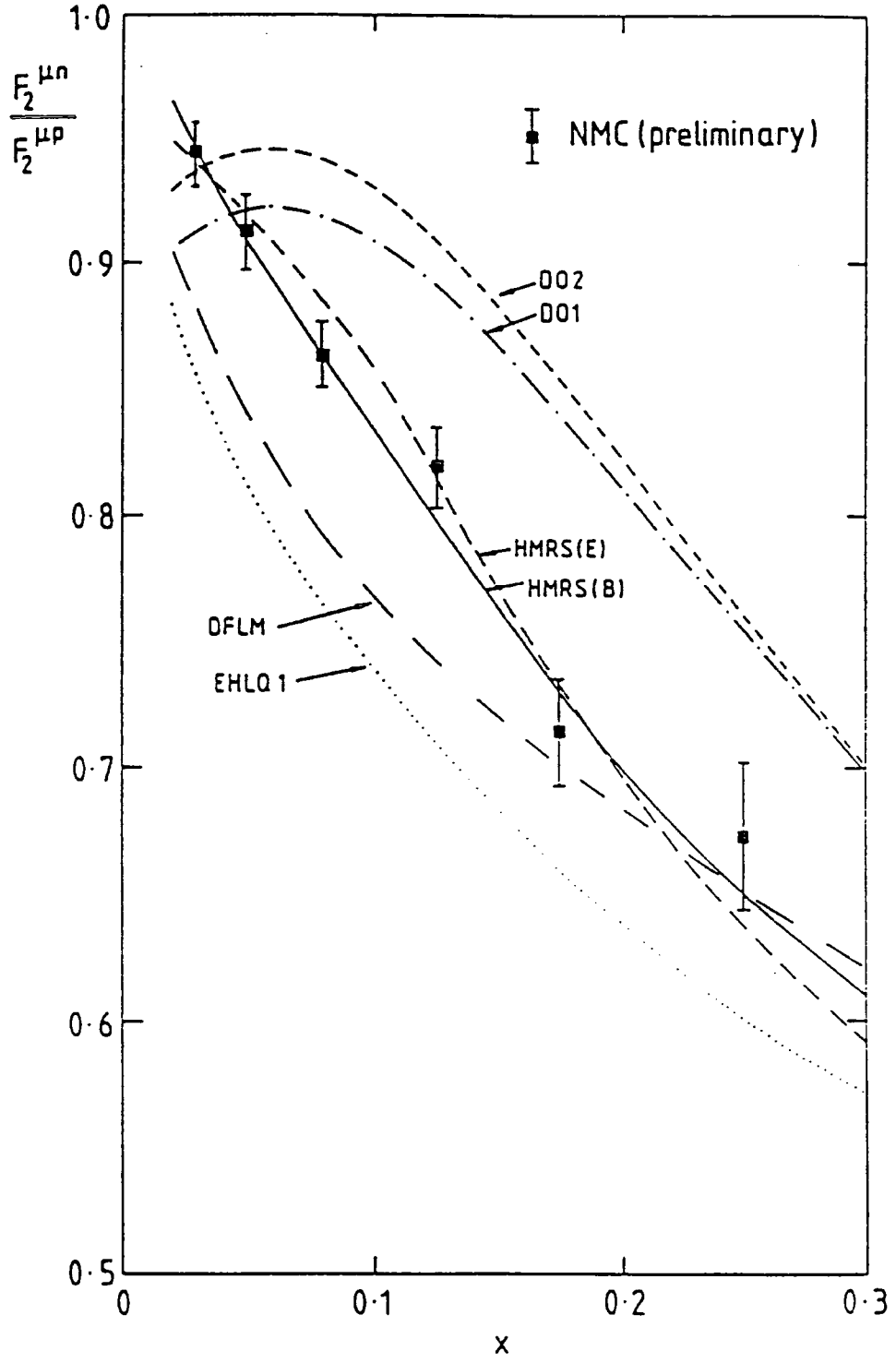

Figure 8.4(b) Comparison of the predictions for the ratio $F_2^{\mu n}/F_2^{\mu p}$ using various parton distributions (HMRS(E), HMRS(B), DO1, DO2 [65], EHLQ1 [71], and DFLM [72]) with data from the NMC collaboration [43] (solid squares).

distributions. One is the adherence of the latter to the new, precise $F_2^{\mu n}/F_2^{\mu p}$ data

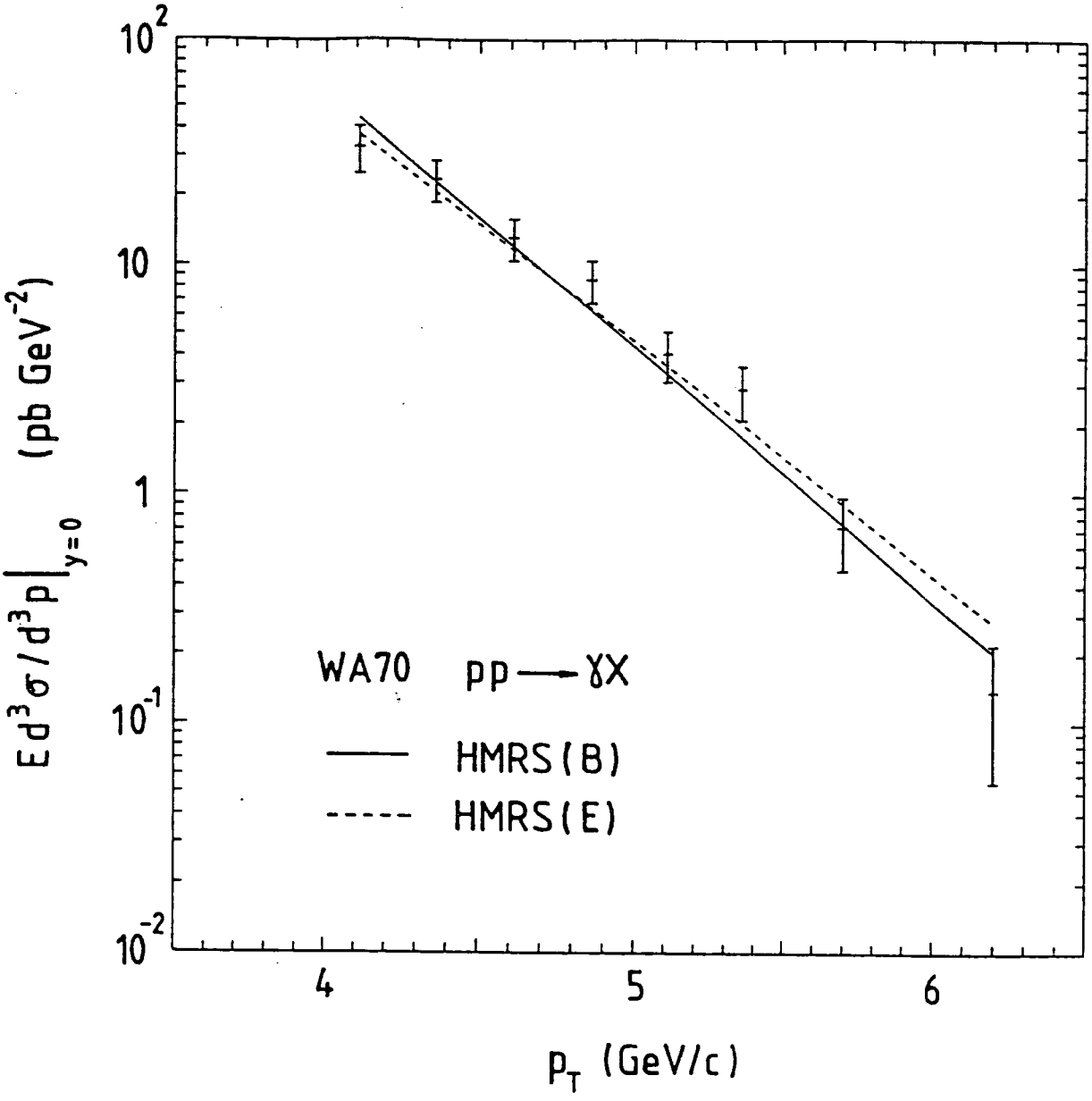

Figure 8.5 Data on the prompt photon transverse momentum distribution in pp collisions at $\sqrt{s} = 23$ GeV from the WA70 collaboration [66] (corrected to $y = 0$), together with the predictions using the HMRS(B) (continuous line) and HMRS(E) (dashed line) parton distributions.

of the NMC while the other, which can be seen in the xu and xd distributions, is due to the renormalization of the $F_2^{\mu p}$ data we performed (that of EMC upwards by 8% and that of BCDMS downwards by 2%). The xg and xSea distributions appear to be broadly similar (although the steepness of the graphs makes it difficult to tell) apart from the fact that the HMRS xSea distributions, being evolved from starting parametrizations with a factor x^{δ_S} (where δ_S is positive)

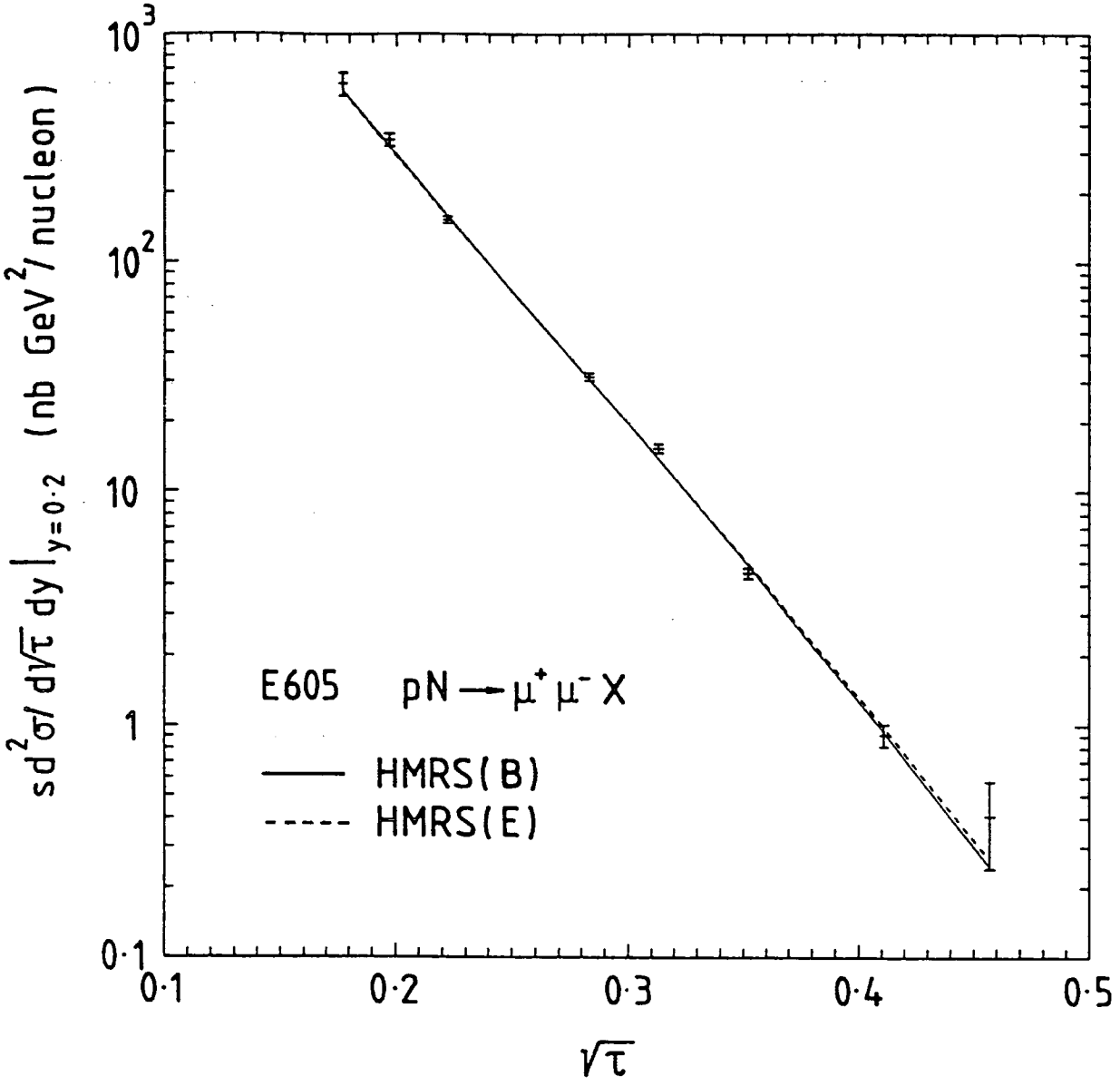

Figure 8.6 Drell-Yan data from the E605 collaboration [70] in pN collisions at $\sqrt{s} = 38.8$ GeV, together with the predictions using the HMRS(B) (continuous line) and HMRS(E) (dashed line) parton distributions.

still 'turn over' at this low Q^2. In Figure 8.8, we plot the ratios of the two HMRS sets (at $Q^2 = 20$ GeV^2) and the ratios between the HMRS and MRS′ sets (for completeness, we also show the ratio of the two MRS′ sets). This figure shows, most vividly, the great difference between the two HMRS sets.

In Figure 8.9, we compare the two HMRS sets (on a logarithmic scale) over a range in x and at a Q^2 value relevant to W and Z production. Figure 8.10

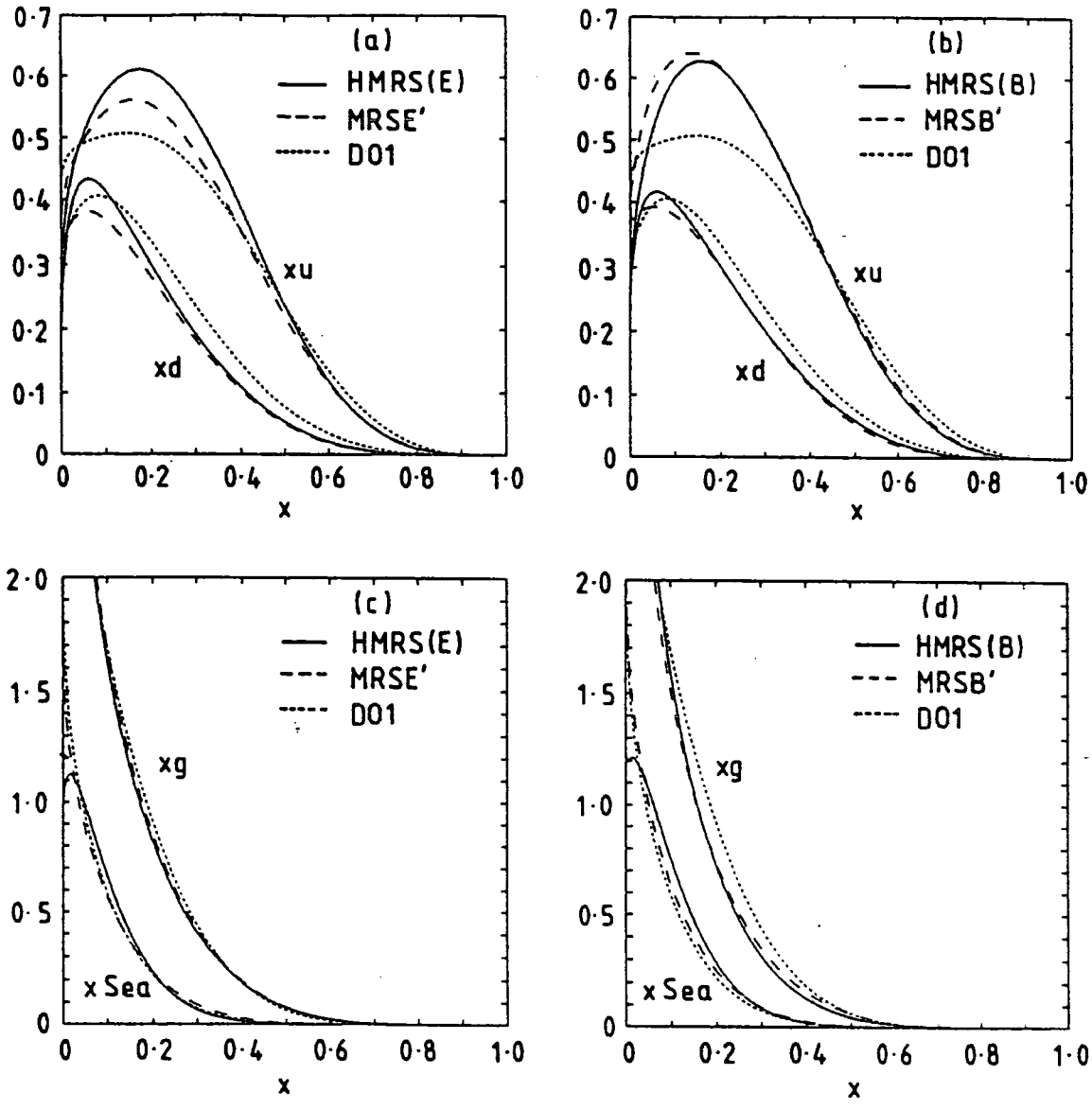

Figure 8.7 The continuous and dashed curves are the HMRS and MRS' [41] parton distributions $xf_i(x, Q^2 = 20\ \text{GeV}^2)$ respectively. The left- (right-)hand plots are the parton distributions obtained using data sets which include the EMC (BCDMS) $F_2^{\mu p}$ measurements. In each case, we show the distributions of Duke and Owens Set 1 [65] for comparison.

shows an extrapolation of the $F_2^{\mu p}$ of HMRS(E) and HMRS(B) to Q^2 values which the HERA ep collider will be able to probe within a few years. Our predictions provide the most accurate benchmark predictions for HERA. Note that we have not included Z^0 contributions to the neutral-current cross-section which become significant for $Q^2/(Q^2 + M_Z^2) \gtrsim O(1)$ (to the right of the dash-

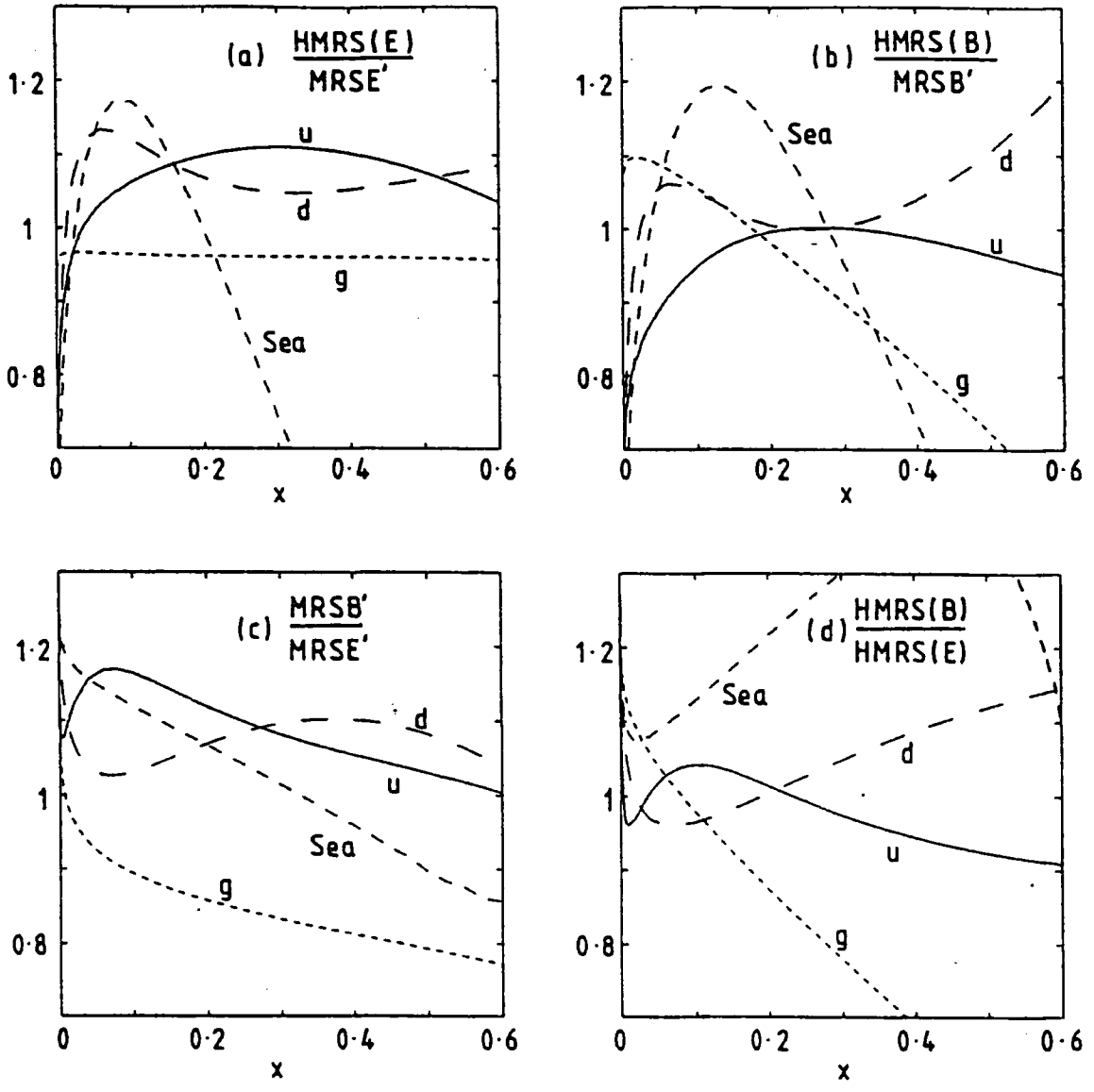

Figure 8.8 Ratios of the quark and gluon distributions at $Q^2 = 20\ \mathrm{GeV}^2$:
(a) f_i(MRSE')/f_i(HMRS(E)); (b) f_i(MRSB')/f_i(HMRS(B));
(c) f_i(MRSB')/f_i(MRSE'); and (d) f_i(HMRS(B))/f_i(HMRS(E)).

dotted line). The differences in the $F_2^{\mu p}$ predictions of the two sets persist at higher Q^2 and the dispersion in the predictions—due to the different values of $\Lambda_{\overline{\mathrm{MS}}}$—can also clearly be seen. Detailed simulations of structure functions at HERA have been performed by Blümlein *et al.* [74], [75]. It should be possible to discriminate between the two different predictions in the range $0.01 \lesssim x \lesssim 0.5$ and thereby resolve the conflict between the $F_2^{\mu p}$ measurements of EMC and BCDMS.

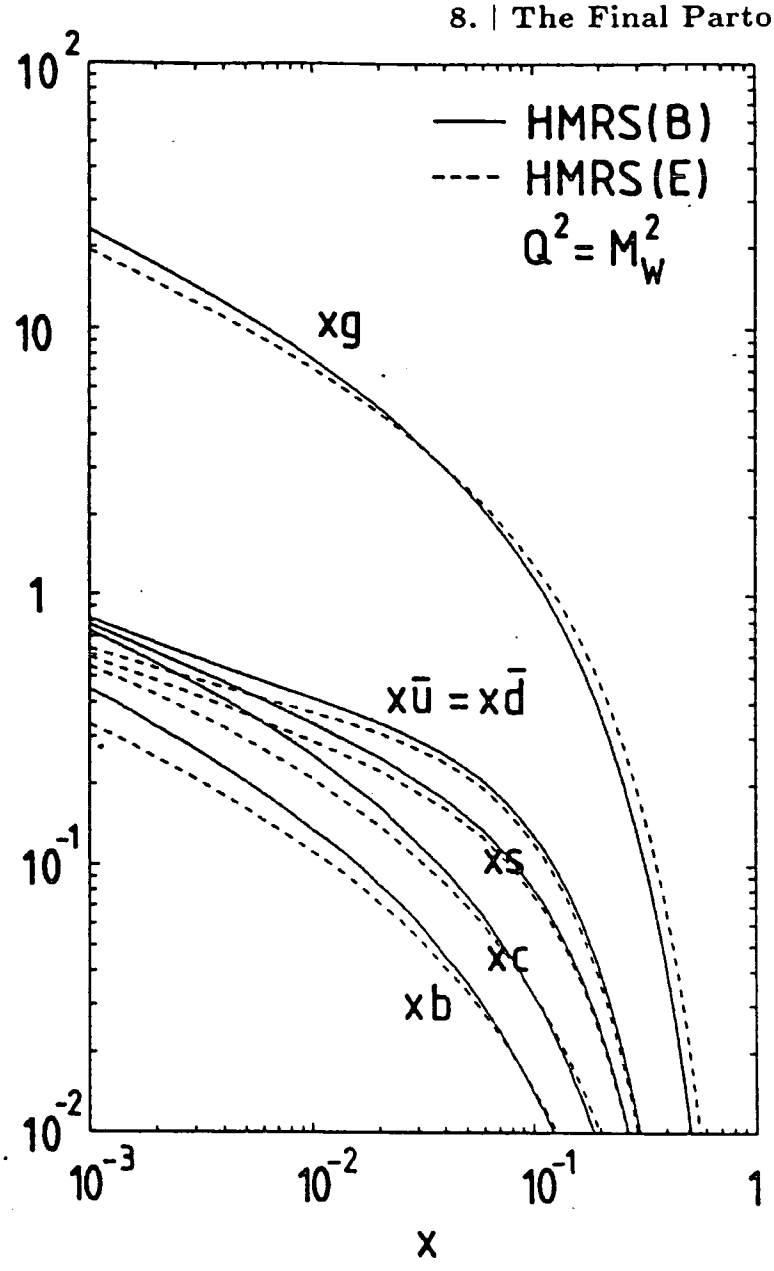

Figure 8.9 The HMRS gluon and sea quark distributions at $Q^2 = M_W^2$.

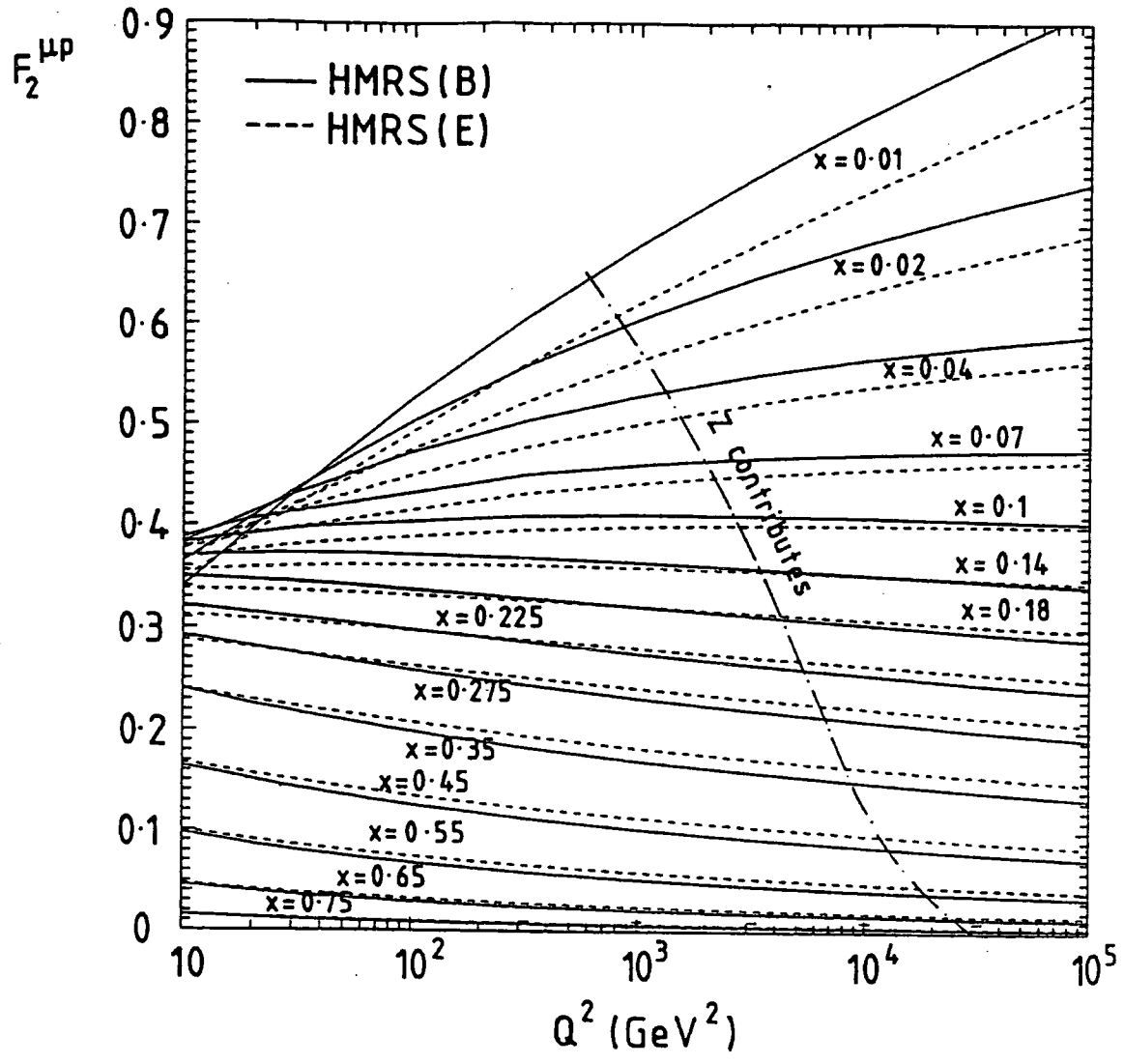

Figure 8.10 Predictions for $F_2^{\mu p}(x, Q^2)$ (electromagnetic part only) extrapolated to the HERA kinematic region.

9. Freedom in the Gluon Distribution

9.1 Uncertainty in the Final Distributions

We have presented parton distributions, HMRS(E) and HMRS(B), which give an excellent overall fit to deep-inelastic scattering data, prompt photon data and data on the Drell-Yan process. In this chapter, we should like to discover where the major uncertainties in these distributions lie.

We need some criterion on which to base our answer and, unfortunately, a meaningful one is not easy to find. We could, for example, vary each parameter in turn, keeping all others fixed, to find the positive and negative changes required to increase the total χ^2 by some amount thus producing a set of parameters, each with its own $\pm$ error. Having done this, we would realize that the results don't answer the question—what we should really like to know is, how well is the *shape* of each parton distribution determined and how is it correlated with the shapes of the other parton distributions. This is obviously very difficult (impossible?) to do in a systematic way so we will content ourselves with asking some simpler questions.

9.2 The Gluon Distribution

We shall start with the gluon distribution for which we could only justify *two* free parameters, given the two constraints below. First, we can be sure that the magnitudes of our gluon distributions are reasonably accurate in the range $0.35 < x < 0.55$ where the accurate prompt photon data exist. Secondly, we can also have some confidence that the integrated gluon distribution for $x \gtrsim 0.05$ has approximately the right value since we have fitted F_2 structure functions well, down to low x, and these depend, albeit somewhat indirectly, on the gluon (in DIS-schemes, the dependence is a consequence of the amount of momentum "left over" for the quark distributions after the gluon has taken its share while, in our $\overline{\text{MS}}$ scheme, there is also a direct contribution from the gluon, reduced by a factor α_s).

What flexibility is there in the form of the gluon distribution at the low values of x which will soon become accessible to colliders? This is a difficult question

which we choose to try to answer in the following way. Our gluon has previously been of the form

$$xg(x,Q_0^2) = A_g(1-x)^{\eta_g} \tag{9.1}$$

where A_g is determined by the constraint of the total momentum sum sule. The gluon distribution at low x is of great importance because many high-energy scattering cross-sections are dominated by gg interactions. So the question we will pose is: by allowing much greater flexibility in the Q_0^2 parametrization of the gluon, what is the spread in xg at low x (at various Q^2 values) ?

We extend the limited flexibility of our two-parameter gluon by allowing it two more:

$$xg(x,Q_0^2) = A_g x^{\delta_g}(1-x)^{\eta_g}(1+\gamma_g x) \tag{9.2}$$

and we determine acceptable fits to the WA70 prompt photon data for two extreme low-x behaviours: one with $\delta_g = -1/2$ which is a gluon with singular behaviour as $x \to 0$ and one with $\delta_g = +1/2$ which has the valence quark behaviour of $xg \to 0$ as $x \to 0$ (but only at $Q^2 = Q_0^2$—as Q^2 increases, $xg(x=0,Q^2)$ increases). There is good motivation for the small-x behaviour, $\delta_g \approx -1/2$, as discussed in [76] where it is shown to be

$$xg(x,Q^2) \sim h(Q^2)e^{\lambda_{max}\ln(1/x)} = h(Q^2)x^{-\lambda_{max}} \tag{9.3}$$

with $\lambda_{max} = (1.9 \pm 0.8)\alpha_s(k_0^2)$ where k_0^2 is an infra-red cut-off: taking $\alpha_s(k_0^2) \approx 0.25$ yields $\lambda_{max} \approx 1/2$.

The factor $(1+\gamma_g x)$ is included so that a good fit to the WA70 prompt photon data can easily be maintained. We proceed slightly differently to our previous fitting of prompt photon data in Chapter 6 in that we keep all of the quark parameters and $\Lambda_{\overline{\rm MS}}$ fixed to preserve our excellent fit to the DIS data, (thus, all our trial gluons carry the same percentage of the total momentum as the HMRS gluons at $Q^2 = Q_0^2$) and we evolve sets of parton momentum distributions for a range of (η_g, γ_g) pairs for each of $\delta_g = -1/2$ and $\delta_g = +1/2$. We, in fact do the same for a gluon with $\delta_g = 0$ in order to show the χ^2 'landscape' in the $\eta_g - \gamma_g$ plane, with the same δ_g as our optimum solutions. The contour plots we

obtain are shown in Figures 9.1–9.7 where the plots marked (a) show the χ^2 to the WA70 prompt photon data, (b) the χ^2 to all the DIS data, and (c) the sum of (a) and (b).

In Figure 9.1, we have detailed the immediate area of the HMRS(E) fit (denoted in this and Figure 9.2 by a star) in the $\gamma_g - \eta_g$ plane. This shows that the HMRS(E) fit is, in fact, a local minimum. Note that the points at $(\gamma_g = -1, \eta_g)$ are identical to those at $(\gamma_g = 0, \eta_g + 1)$ since $(1-x)^{\eta_g}(1-x)^1 \equiv (1-x)^{\eta_g+1}(1-x)^0$. Figure 9.2 shows the same plot extended to a much larger region of the $\gamma_g - \eta_g$ plane. Figure 9.2a shows that the fit to the WA70 data improves slightly with increasing γ_g and η_g at low γ_g (since these two parameters can almost compensate each other). Then, with $\gamma_g \gtrsim 10$, the χ^2 improves for constant η_g and increasing γ_g. The dependence on the DIS data in 9.2b is fairly weak but shows the same general trend. We would expect, as $\gamma_g \to \infty$ for fixed η_g, that the χ^2 would stay virtually constant since the parametrization, $A_g(1-x)^{\eta_g}(1+\gamma_g x)$, tends to $A'_g(1-x)^{\eta_g}x^1$ except for $x \lesssim 1/\gamma_g$ where there are no data.

In Figure 9.3(a), the E-type $\delta_g = +1/2$ gluon, we see that there is a 'valley' of points with χ^2/point $\lesssim 1$ (the best being around $\gamma_g = 0, \eta_g = 6$ with a χ^2 of 6.0 to the eight WA70 data points). Figure 9.4 shows we can also obtain a good fit with a 'singular' $\delta_g = -1/2$ E-type gluon. As $\gamma_g \to \infty$ in this plot, the parametrization tends to $xg = A''_g x^{+1/2}(1-x)^{\eta_g}$ for $x \gtrsim 1/\gamma_g$ and so, in that limit, we should reproduce the χ^2 values along the $\gamma_g = 0$ line of Figure 9.3.

The contour plots of the B-type gluons in Figures 9.5–9.7 have the same qualitative features as the E-type gluons (the HMRS(B) fit is denoted, in Figure 9.5, by a star). In this case, however, the much smaller errors on the BCDMS $F_2^{\mu p}$ data accentuate the dependence of the χ^2 on the DIS data and it is easier to see that this dependence is the same as that of the WA70 data (in the $\overline{\text{MS}}$ scheme, the gluon contributes directly to the F_2 structure functions as well as affecting the Q^2 evolution of the quark distributions). Again, acceptable fits to both DIS and prompt photon data can be achieved with all three values of δ_g

From these plots, we choose, for illustrative purposes, the fits marked E_+, E_-, B_+, and B_- plus the HMRS(E) and HMRS(B) fits where, for example, E_- is the E-type gluon with $\delta_g = -1/2$. We have chosen the $\delta_g = 0$ fits to be the

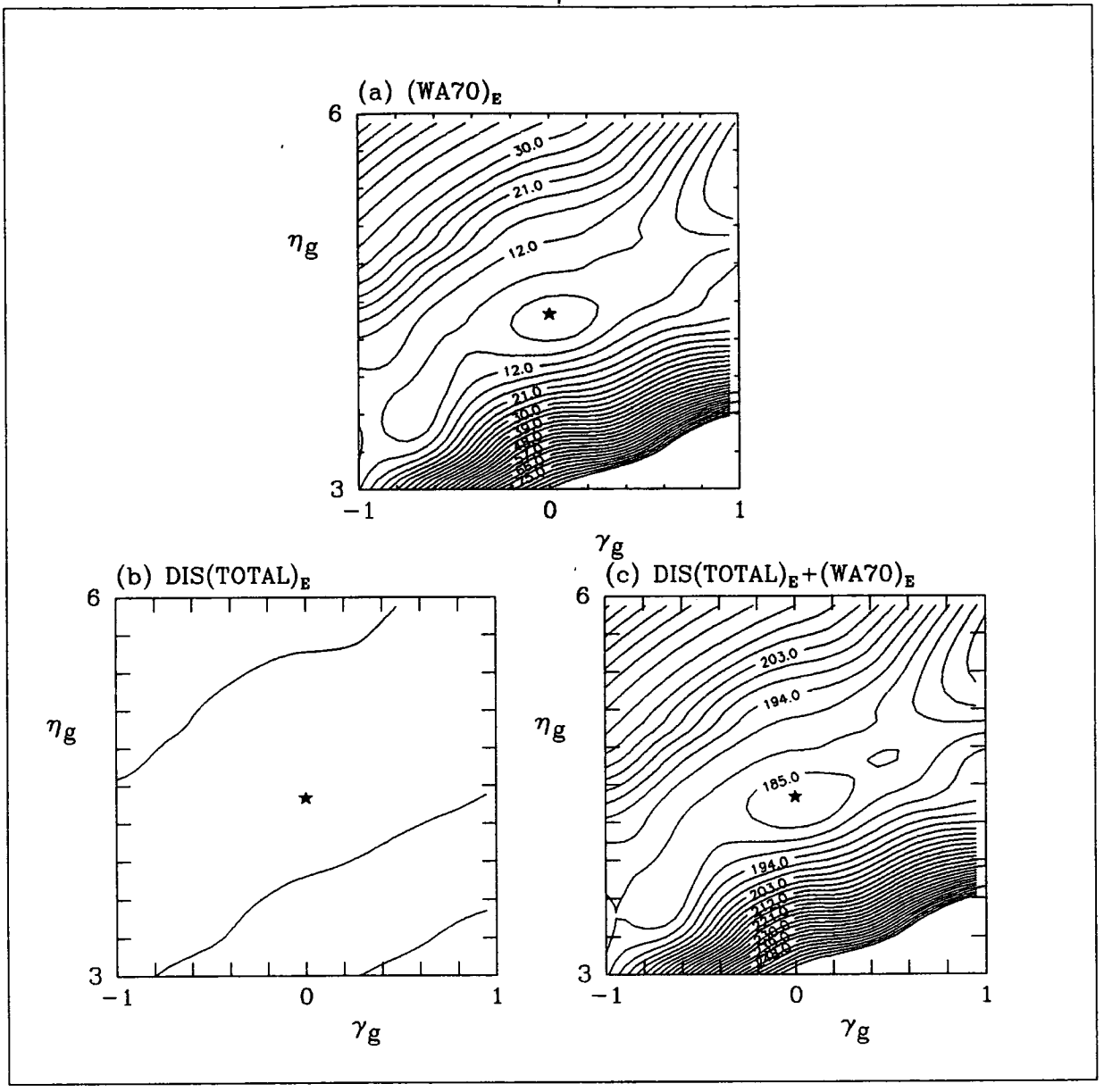

Figure 9.1 (a) shows contours of constant χ^2 in the $\gamma_g - \eta_g$ plane where χ^2 is a measure of the quality of the theoretical prediction for the WA70 prompt photon data [66] in the range $-0.35 < x_F < 0.45$ (corrected to $y = 0$) using the various sets of parton distributions obtained by re-evolving the HMRS(E) set with the gluon momentum redistributed in the form $xg(x, Q_0^2) = A_g x^{\delta_g}(1-x)^{\eta_g}(1+\gamma_g x)$ with δ_g fixed at zero. (b) shows the total χ^2 to the deep-inelastic scattering data of [32] (EMC $F_2^{\mu p}$), [36] ($F_2^{\nu N}$ and $xF_3^{\nu N}$) and [40], [42], [43] ($F_2^{\mu n}/F_2^{\mu p}$). (c) is the total of (a) and (b). The stars signify the position of the HMRS(E) fit. The statistical and systematic errors of all data have been combined in quadrature. The contour interval is three units of χ^2 for all three contour plots.

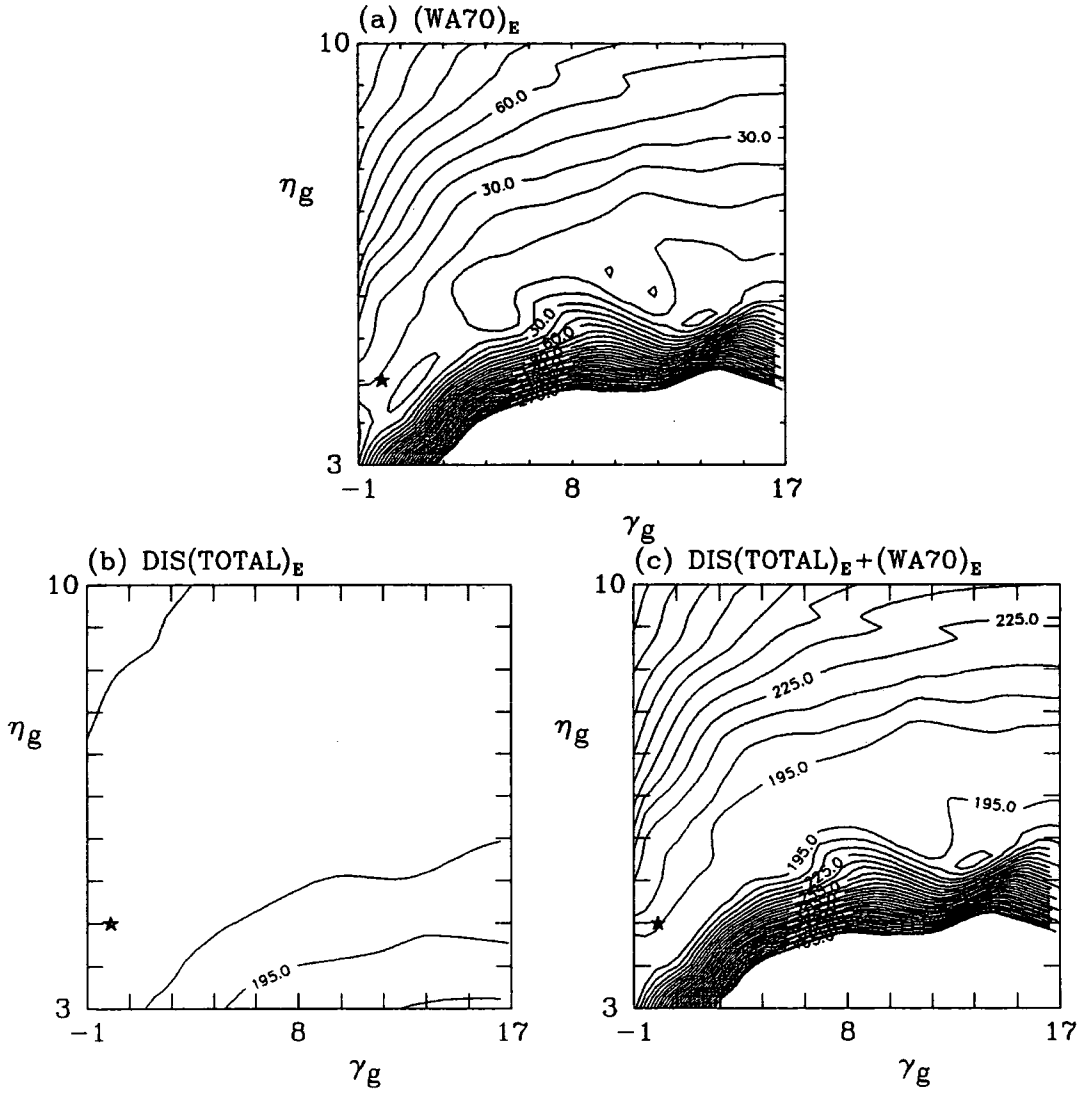

Figure 9.2 (a) shows contours of constant χ^2 in the $\gamma_g - \eta_g$ plane where χ^2 is a measure of the quality of the theoretical prediction for the WA70 prompt photon data [66] in the range $-0.35 < x_F < 0.45$ (corrected to $y = 0$) using the various sets of parton distributions obtained by re-evolving the HMRS(E) set with the gluon momentum redistributed in the form $xg(x, Q_0^2) = A_g x^{\delta_g}(1-x)^{\eta_g}(1+\gamma_g x)$ with δ_g fixed at zero. (b) shows the total χ^2 to the deep-inelastic scattering data of [32] (EMC $F_2^{\mu p}$), [36] ($F_2^{\nu N}$ and $xF_3^{\nu N}$) and [40], [42], [43] ($F_2^{\mu n}/F_2^{\mu p}$). (c) is the total of (a) and (b). The stars signify the position of the HMRS(E) fit. The statistical and systematic errors of all data have been combined in quadrature. The contour interval is 10 units of χ^2 for all three contour plots.

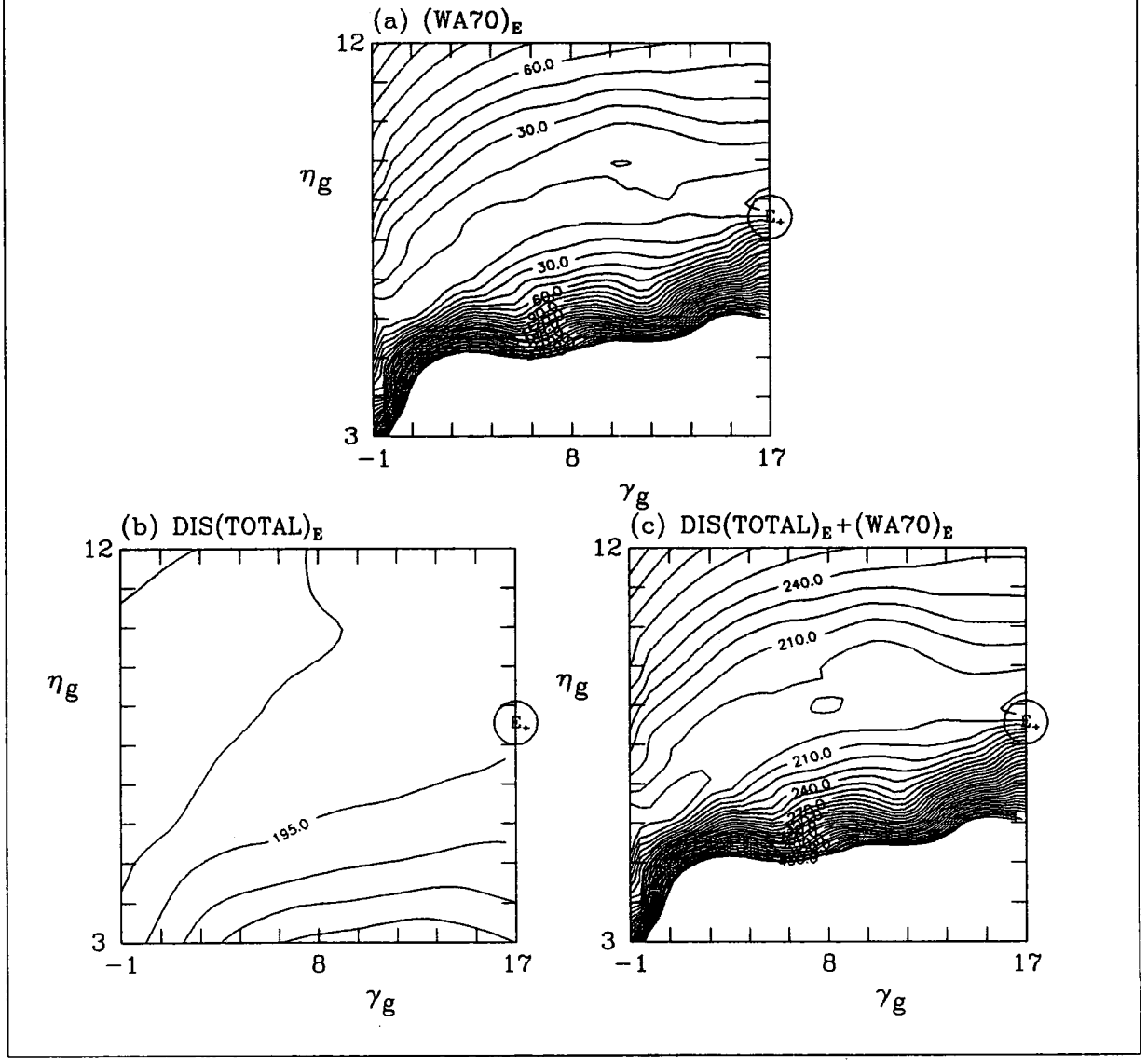

Figure 9.3 (a) shows contours of constant χ^2 in the $\gamma_g - \eta_g$ plane where χ^2 is a measure of the quality of the theoretical prediction for the WA70 prompt photon data [66] in the range $-0.35 < x_F < 0.45$ (corrected to $y = 0$) using the various sets of parton distributions obtained by re-evolving the HMRS(E) set with the gluon momentum redistributed in the form $xg(x, Q_0^2) = A_g x^{\delta_g}(1-x)^{\eta_g}(1+\gamma_g x)$ with $\delta_g = +1/2$. (b) shows the total χ^2 to the deep-inelastic scattering data of [32] (EMC $F_2^{\mu p}$), [36] ($F_2^{\nu N}$ and $xF_3^{\nu N}$) and [40], [42], [43] ($F_2^{\mu n}/F_2^{\mu p}$). (c) is the total of (a) and (b). 'E_+' signifies the position of the gluon chosen for illustrative purposes (see text). The statistical and systematic errors of all data have been combined in quadrature. The contour interval is 10 units of χ^2 for all three contour plots.

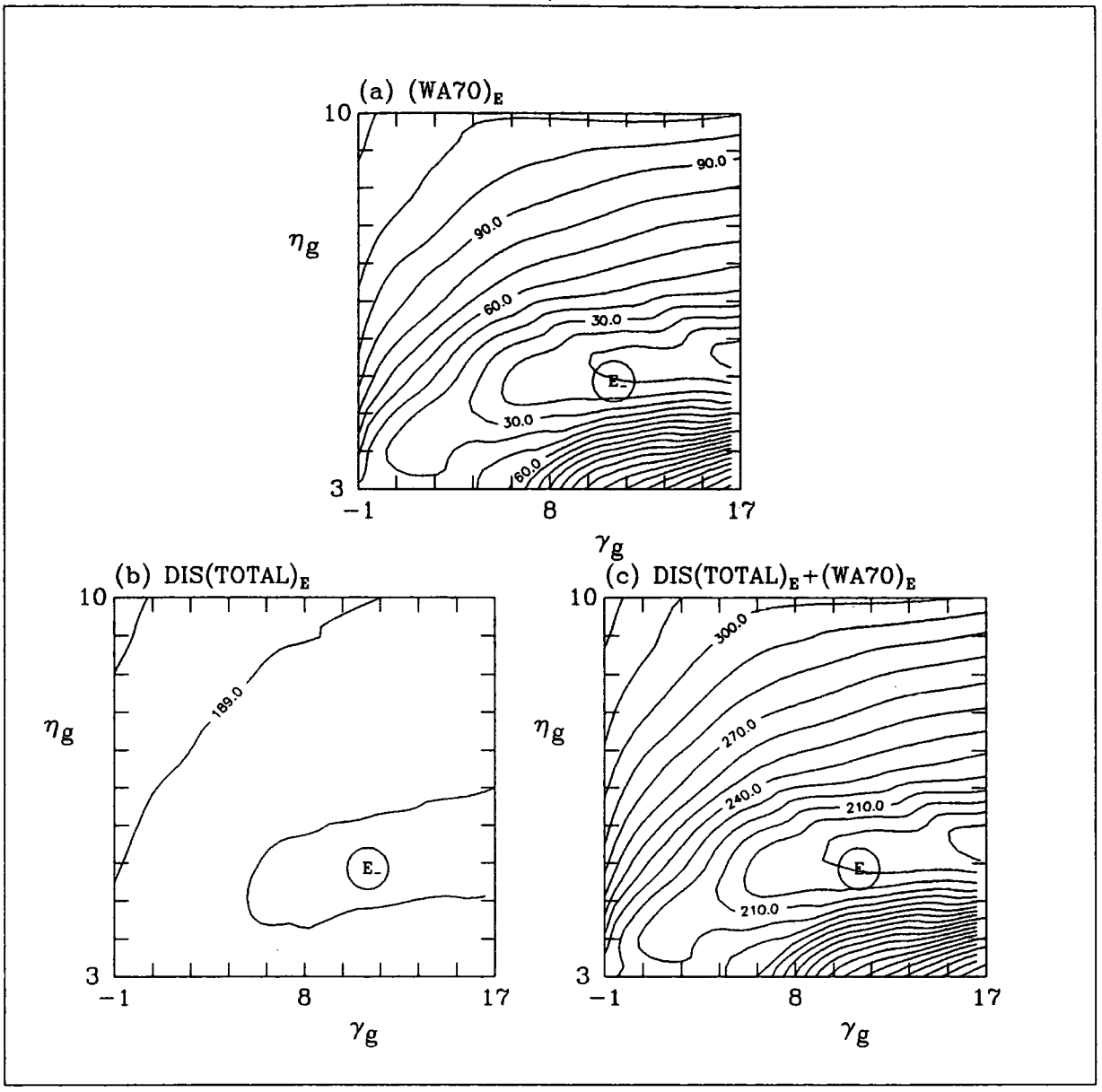

Figure 9.4 (a) shows contours of constant χ^2 in the $\gamma_g - \eta_g$ plane where χ^2 is a measure of the quality of the theoretical prediction for the WA70 prompt photon data [66] in the range $-0.35 < x_F < 0.45$ (corrected to $y = 0$) using the various sets of parton distributions obtained by re-evolving the HMRS(E) set with the gluon momentum redistributed in the form $xg(x, Q_0^2) = A_g x^{\delta_g}(1-x)^{\eta_g}(1+\gamma_g x)$ with $\delta_g = -1/2$. (b) shows the total χ^2 to the deep-inelastic scattering data of [32] (EMC $F_2^{\mu p}$), [36] ($F_2^{\nu N}$ and $xF_3^{\nu N}$) and [40], [42], [43] ($F_2^{\mu n}/F_2^{\mu p}$). (c) is the total of (a) and (b). 'E_' signifies the position of the gluon chosen for illustrative purposes (see text). The statistical and systematic errors of all data have been combined in quadrature. The contour interval is 10 units of χ^2 for all three contour plots.

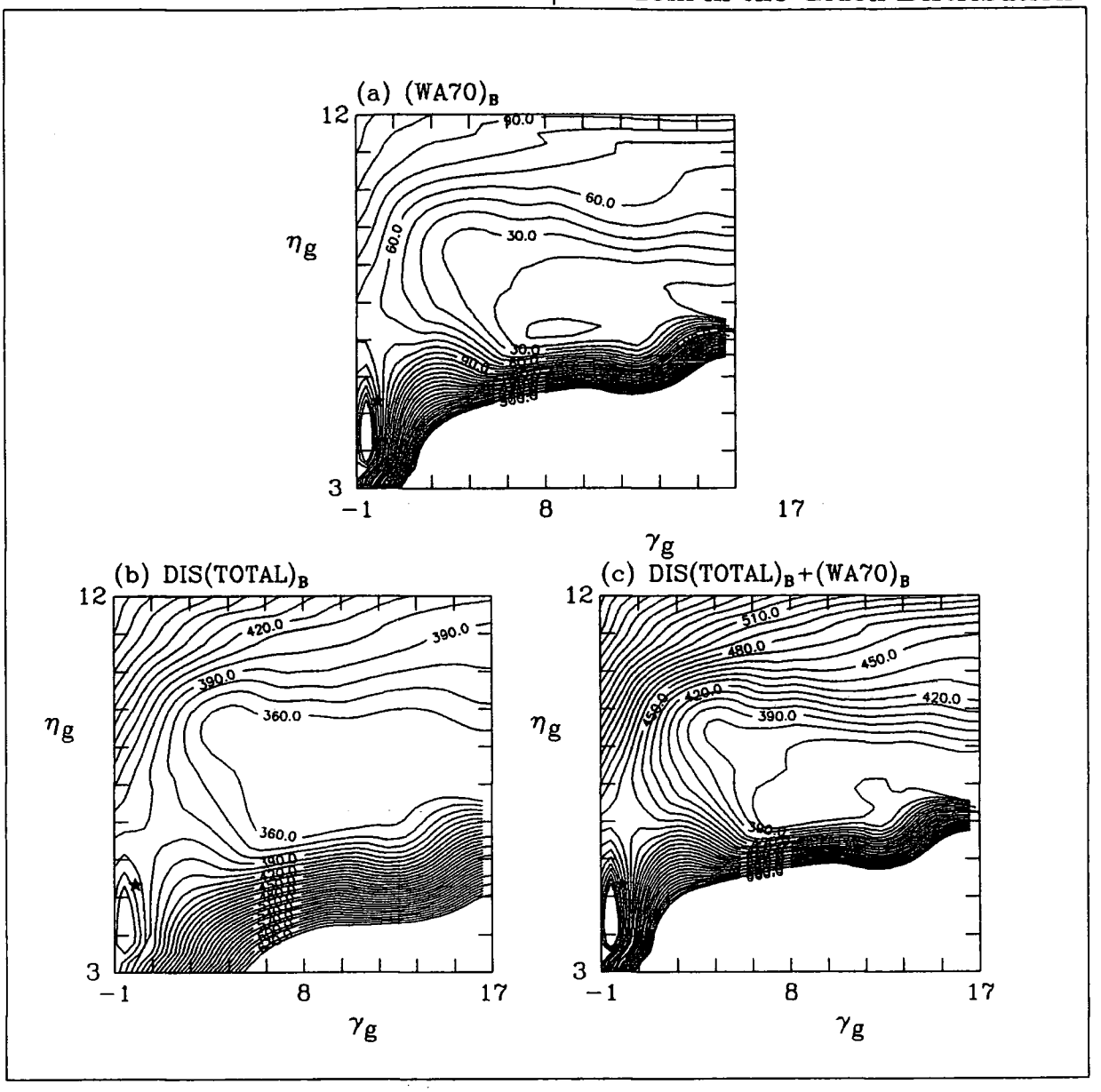

Figure 9.5 (a) shows contours of constant χ^2 in the $\gamma_g - \eta_g$ plane where χ^2 is a measure of the quality of the theoretical prediction for the WA70 prompt photon data [66] in the range $-0.35 < x_< 0.45$ (corrected to $y = 0$) using the various sets of parton distributions obtained by re-evolving the HMRS(B) set with the gluon momentum redistributed in the form $xg(x, Q_0^2) = A_g x^{\delta_g}(1-x)^{\eta_g}(1+\gamma_g x)$ with δ_g fixed at zero. (b) shows the total χ^2 to the deep-inelastic scattering data of [32] (BCDMS $F_2^{\mu p}$), [36] ($F_2^{\nu N}$ and $xF_3^{\nu N}$) and [40], [42], [43] ($F_2^{\mu n}/F_2^{\mu p}$). (c) is the total of (a) and (b). The stars signify the position of the HMRS(B) fit. The statistical and systematic errors of all data have been combined in quadrature. The contour interval is 10 units of χ^2 for all three contour plots.

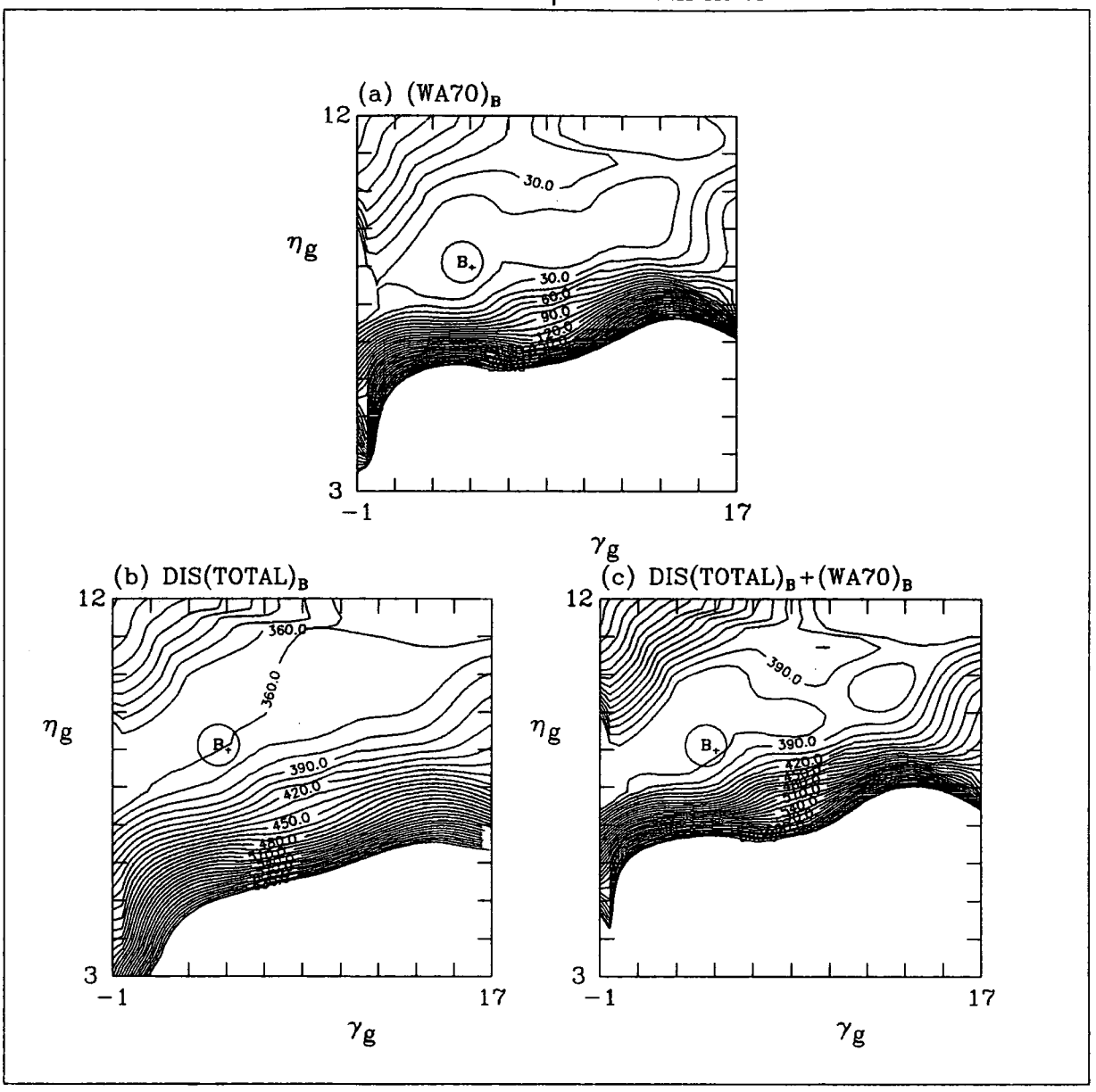

Figure 9.6 (a) shows contours of constant χ^2 in the $\gamma_g - \eta_g$ plane where χ^2 is a measure of the quality of the theoretical prediction for the WA70 prompt photon data [66] in the range $-0.35 < x_F < 0.45$ (corrected to $y = 0$) using the various sets of parton distributions obtained by re-evolving the HMRS(B) set with the gluon momentum redistributed in the form $xg(x, Q_0^2) = A_g x^{\delta_g}(1-x)^{\eta_g}(1+\gamma_g x)$ with $\delta_g = +1/2$. (b) shows the total χ^2 to the deep-inelastic scattering data of [32] (BCDMS $F_2^{\mu p}$), [36] ($F_2^{\nu N}$ and $xF_3^{\nu N}$) and [40], [42], [43] ($F_2^{\mu n}/F_2^{\mu p}$). (c) is the total of (a) and (b). 'B_+' signifies the position of the gluon chosen for illustrative purposes (see text). The statistical and systematic errors of all data have been combined in quadrature. The contour interval is 10 units of χ^2 for all three contour plots.

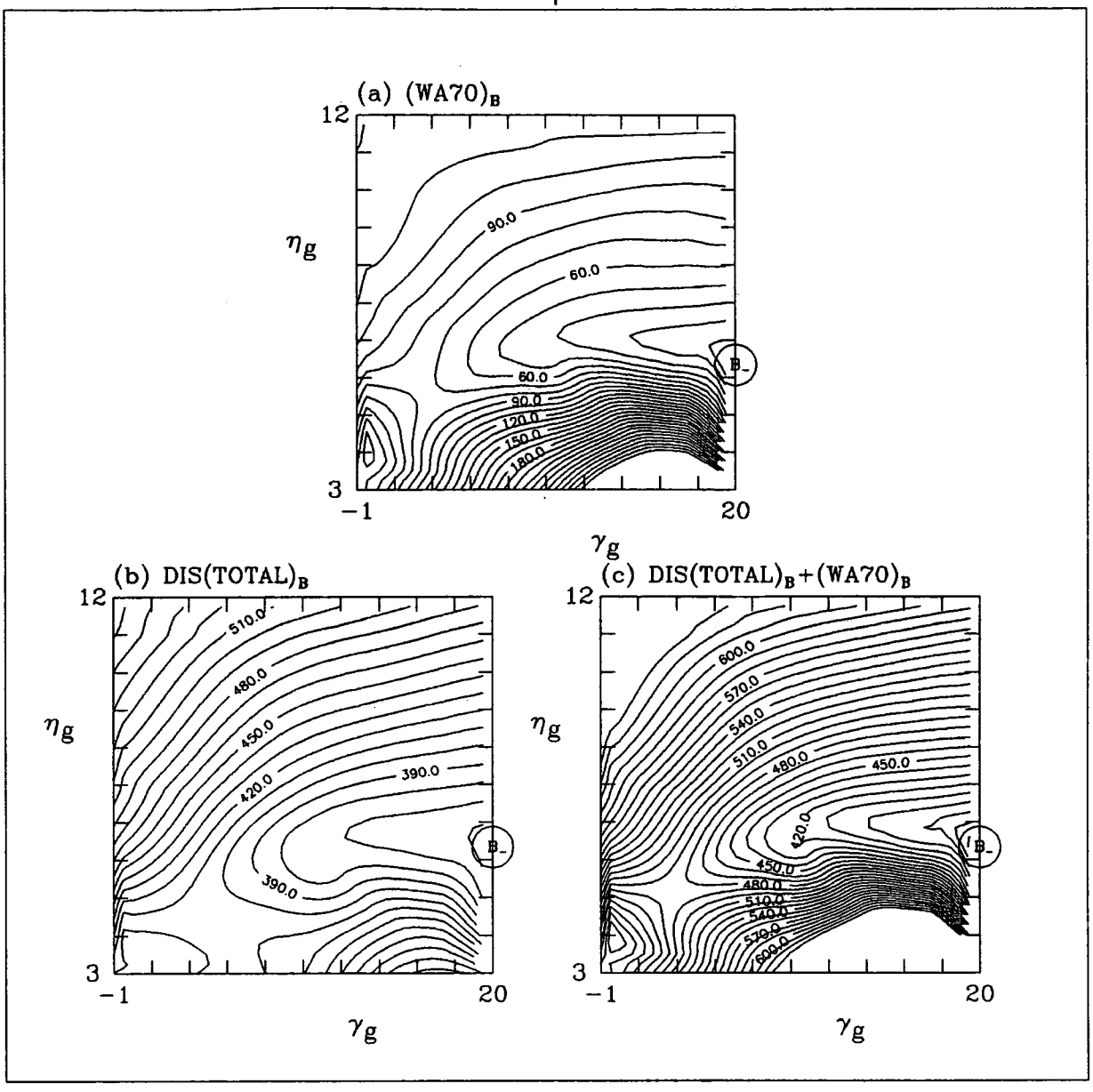

Figure 9.7 (a) shows contours of constant χ^2 in the $\gamma_g - \eta_g$ plane where χ^2 is a measure of the quality of the theoretical prediction for the WA70 prompt photon data [66] in the range $-0.35 < x_F < 0.45$ (corrected to $y = 0$) using the various sets of parton distributions obtained by re-evolving the HMRS(B) set with the gluon momentum redistributed in the form $xg(x, Q_0^2) = A_g x^{\delta_g}(1-x)^{\eta_g}(1+\gamma_g x)$ with $\delta_g = -1/2$. (b) shows the total χ^2 to the deep-inelastic scattering data of [32] (BCDMS $F_2^{\mu p}$), [36] ($F_2^{\nu N}$ and $xF_3^{\nu N}$) and [40], [42], [43] ($F_2^{\mu n}/F_2^{\mu p}$). (c) is the total of (a) and (b). 'B_' signifies the position of the gluon chosen for illustrative purposes (see text). The statistical and systematic errors of all data have been combined in quadrature. The contour interval is 10 units of χ^2 for all three contour plots.

actual HMRS fits so that we will have some 'controls' against which to measure the others. These fits give (by design) the acceptable fits to the WA70 data shown in Figures 9.8 and 9.9 (we have deliberately chosen non-optimum fits to attempt, simultaneously, to show borderline good fits to the WA70 data).

The low x behaviour of these gluons at three Q^2 values is shown in Figure 9.10. Momentum conservation ensures that the gluons cross, e.g. the singular gluon, being greater than the control at low x is forced to be smaller at high x. The three solutions are, predictably, similar in the region $0.4 \lesssim x \lesssim 0.6$ since they are good fits to the WA70 data which is sensitive to the gluon in this region of x. Looking at the Q^2 evolution of the three solutions, we see demonstrated the well-known fact that differences in the forms of the gluons decrease with increasing Q^2.

9.3 Discriminating between the Different Gluons

We now discuss what implications these different gluon distributions have on predictions of high-energy cross-sections which are sensitive to the gluon at low x (for $x \gtrsim 0.05$, we can see that the gluons are still very similar at all values of Q^2). We discuss the most promising methods—the cross-section for J/ψ photoproduction and the measurement of the longitudinal structure function, F_L, at the HERA ep collider. Studies of the phenomenology of these two processes can be found in [77] and an experimental simulation in [78] and [79].

The inelastic photoproduction of J/ψ mesons, $\gamma p \rightarrow J/\psi X$ is dominated by $\gamma g \rightarrow J/\psi g$ at low values of x and the production cross-section can be well approximated by the very simple form (see [80]):

$$\sigma(\gamma p \rightarrow J/\psi X) \approx 1.5 \overline{x} g(\overline{x}, m^2_{J/\psi}) \text{ nb} \tag{9.4}$$

where $\overline{x} = 3.4 m^2_{J/\psi}/s$ (with s equal to the square of the γp COM energy). The differences between the cross-sections for our three gluons therefore mirror the differences between the gluons at $Q^2 = m^2_{J/\psi}$ (see Figure 9.11). In [78], it is shown that an integrated luminosity of 100 pb^{-1} at the HERA collider will be able to put some data points on Figure 9.11, with small enough errors for a choice

to be made between the different gluons in this x region (the abcissa of Figure 9.11 corresponds to a range in x of 0.6×10^{-3} to 2.3×10^{-3}).

Another potential discriminator is the longitudinal structure function, F_L, which also depends quite strongly on the gluon distribution at low x. In fact, to a good approximation [79],

$$F_L(0.4x, Q^2) = \frac{2\alpha_s(Q^2)}{3\pi}\left(0.565xg(x, Q^2) + F_2(0.8x, Q^2)\right) . \qquad (9.5)$$

Figure 9.12 shows the three predictions at $Q^2 = 40$ GeV^2 , calculated using the exact formula (recall (3.52))

$$F_L = \frac{\alpha_s(Q^2)}{2\pi}x^2 \int_x^1 \frac{dy}{y^3}\left[\frac{8}{3}F_2(y, Q^2) + \frac{40}{9}(1 - x/y)yg(y, Q^2)\right] . \qquad (9.6)$$

The kinematic range in x accessible at HERA should be $10^{-3} \lesssim x \lesssim 10^{-2}$ so this method should also serve to help determine the low-x behaviour of the gluon.

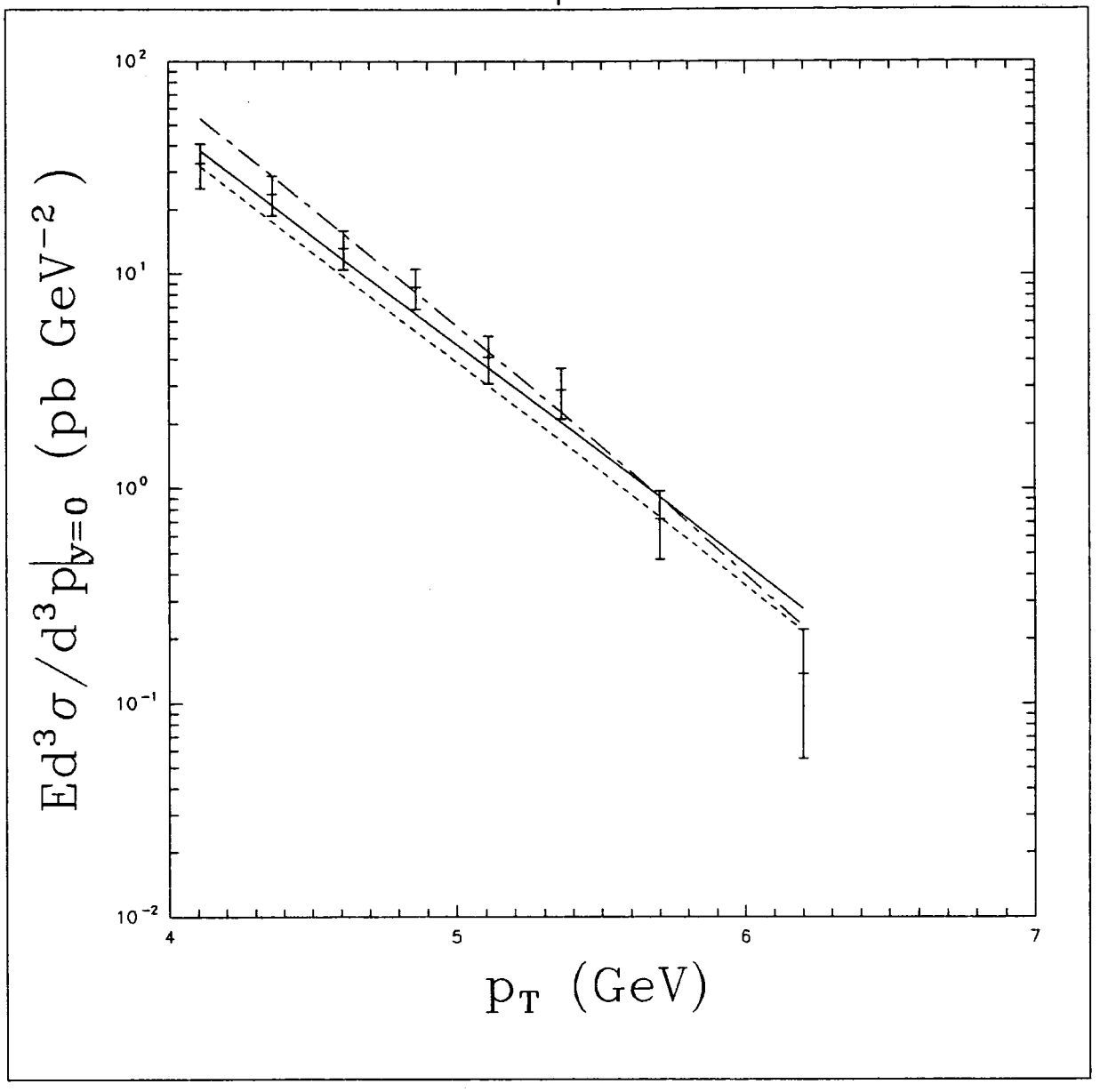

Figure 9.8 Data on the prompt photon transverse momentum distribution in pp collisions at $\sqrt{s} = 23$ GeV from the WA70 collaboration [66] (corrected to $y = 0$), together with the predictions using the E (continuous line), E_+ (dot-dashed line) and E_- (dashed line) parton distributions. The gluon parameters δ, γ, η of Equation (9.2) are $(0, 0, 4.4)$, $(1/2, 17, 8)$, $(-1/2, 11, 5)$ for E, E_+ and E_- respectively.

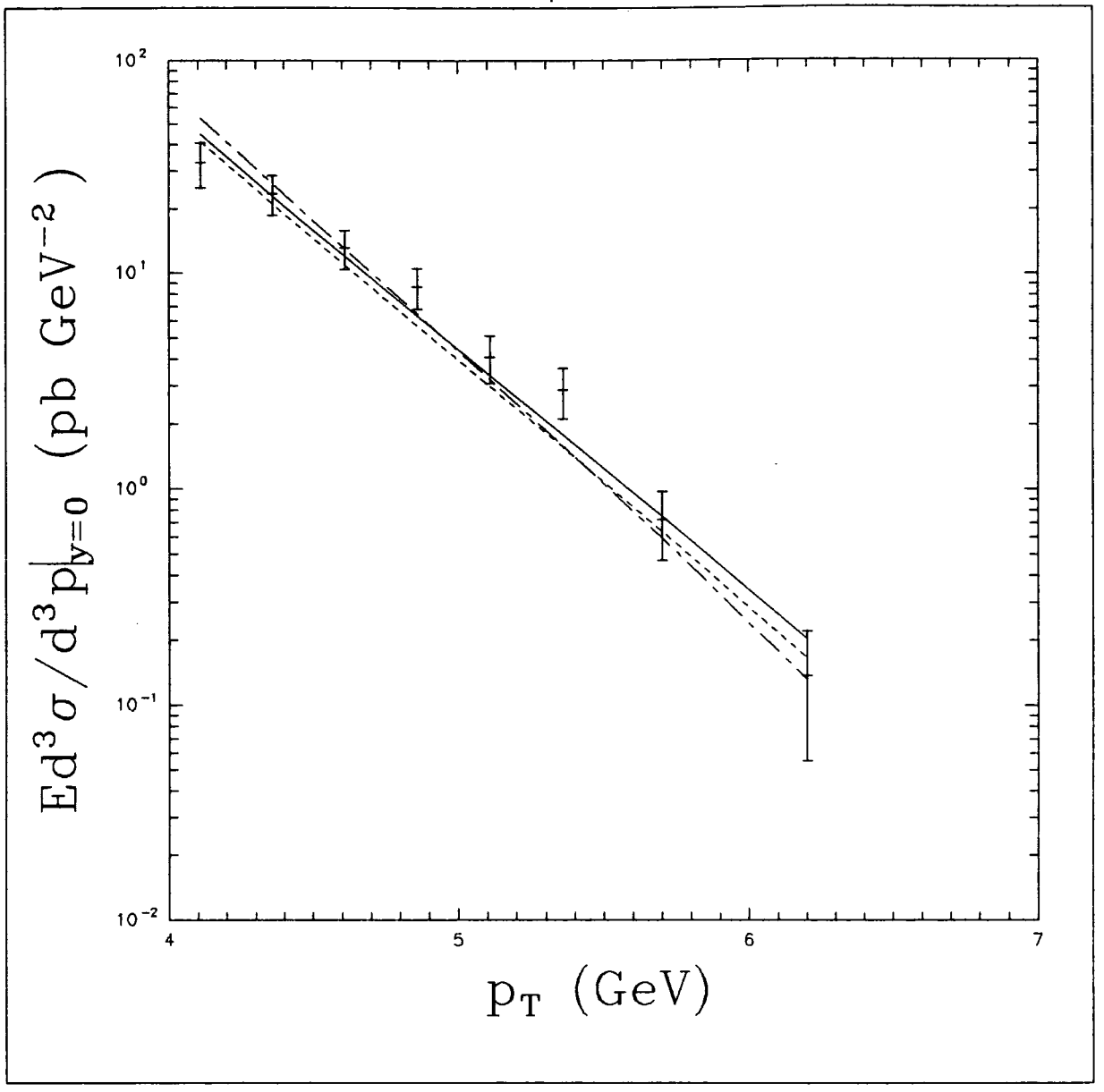

Figure 9.9 Data on the prompt photon transverse momentum distribution in pp collisions at $\sqrt{s} = 23$ GeV from the WA70 collaboration [66] (corrected to $y = 0$), together with the predictions using the B (continuous line), B_+ (dot-dashed line) and B_- (dashed line) parton distributions. The gluon parameters δ, γ, η of Equation (9.2) are $(0, 0, 5.1)$, $(1/2, 4, 8.5)$, $(-1/2, 20, 6)$ for B, B_+ and B_- respectively.

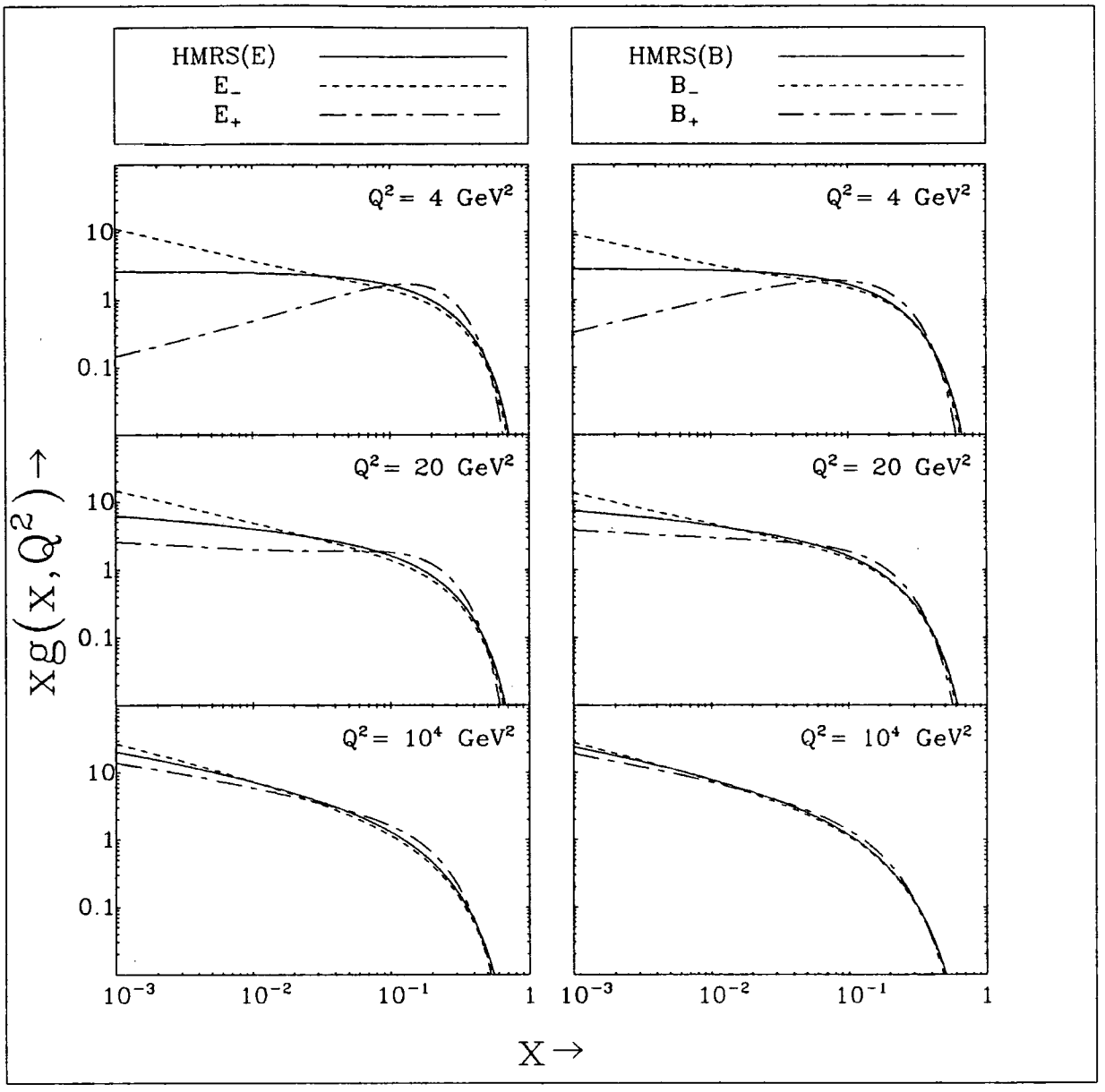

Figure 9.10 The left-hand column shows the three gluon distributions E (continuous line), E_+ (dot-dashed line) and E_- (dashed line) as functions of x for three Q^2 values: 4 GeV^2, 20 GeV^2 and 10^4 GeV^2. The right-hand column shows the same for the B (continuous line), B_+ (dot-dashed line) and B_- (dashed line) gluon distributions.

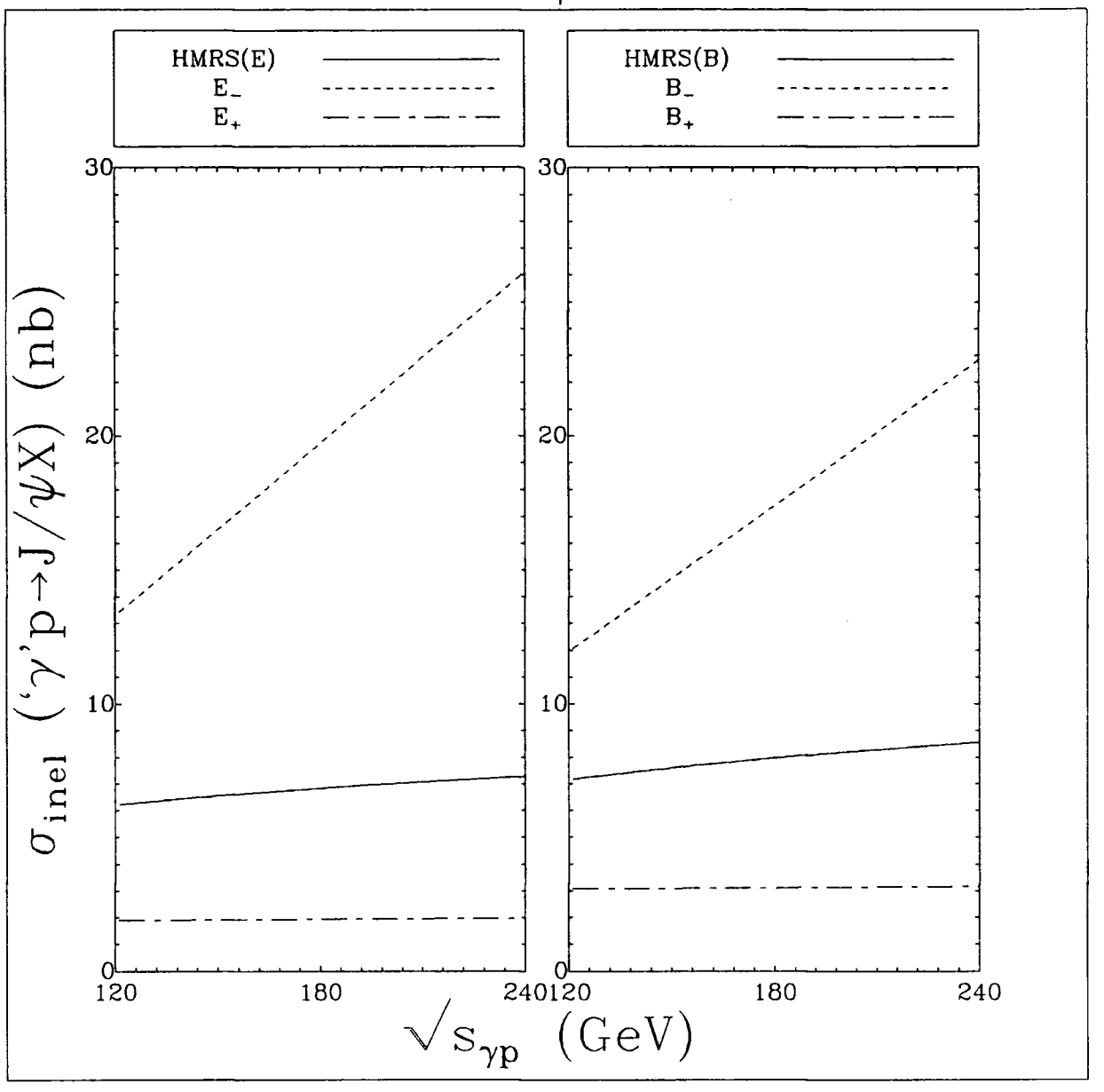

Figure 9.11 The left-hand column shows the predictions for the inelastic J/ψ production cross section, using the three gluons: E (continuous line), E_+ (dot-dashed line) and E_- (dashed line), as a function of $\sqrt{s_{\gamma p}}$ relevant to HERA energies and the right-hand column shows the same for the corresponding B (continuous line), B_+ (dot-dashed line) and B_- (dashed line) gluons. An energy cut of $E_\psi < 0.8E_\gamma$ and a momentum cut of $p_T^2 > 0.1m_\psi^2$ have been applied.

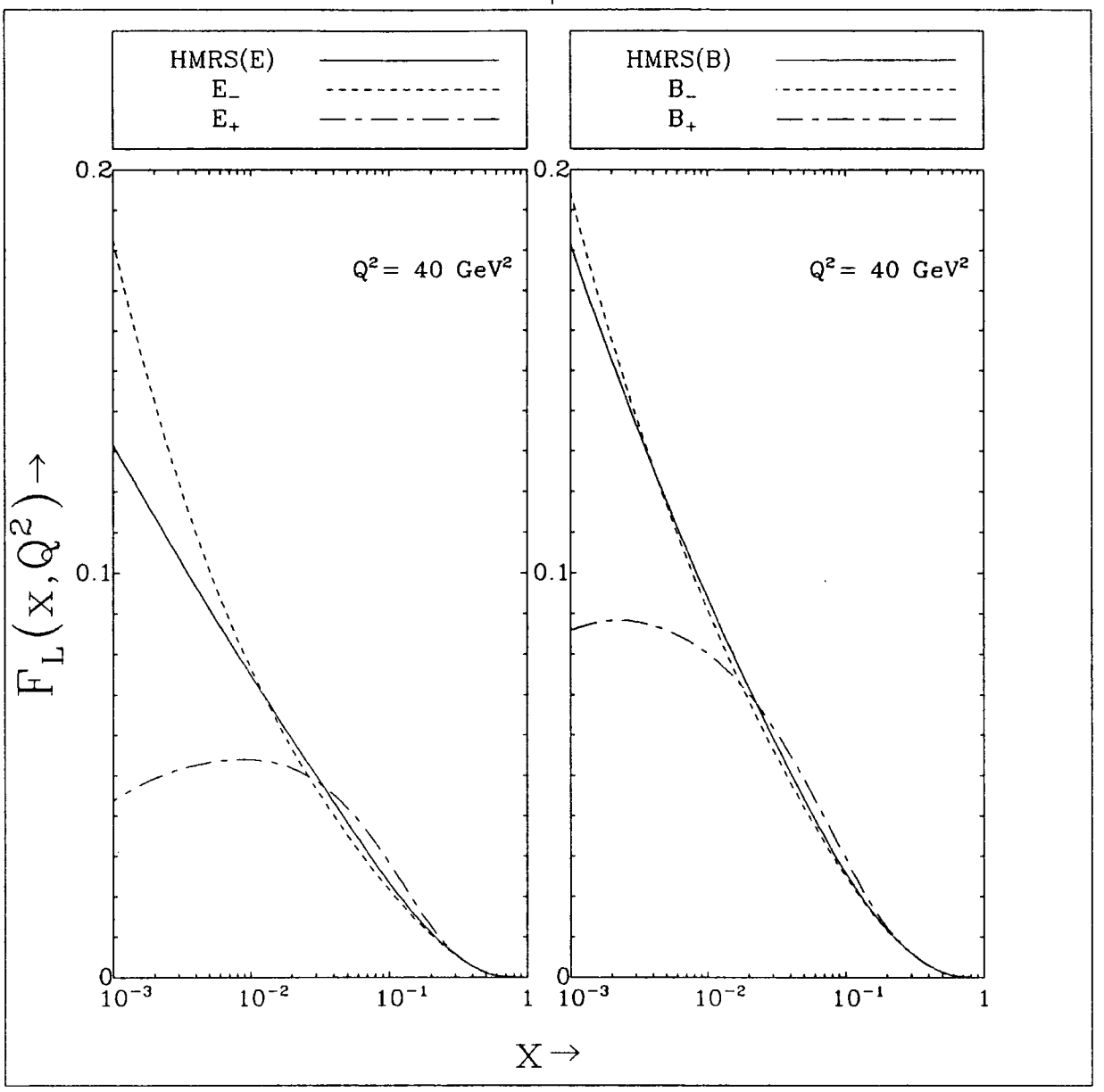

Figure 9.12 The left-hand column shows the predictions for the longitudinal structure function $F_L(x, Q^2)$ at HERA as a function of x at $Q^2 = 40$ GeV^2 , for the three gluons: E (continuous line), E_+ (dot-dashed line) and E_- (dashed line). and the right-hand column shows the same for the corresponding B (continuous line), B_+ (dot-dashed line) and B_- (dashed line) gluons.

10. Conclusions

We have determined parton momentum distributions using a next-to-leading logarithm approximation in the $\overline{\rm MS}$ scheme. We have not biased our analysis towards either of the mutually-inconsistent sets of $F_2^{\mu p}$ data of BCDMS and EMC and have performed it using both. We cannot conclude that our analysis favours either of these sets in preference to the other and so that remains a problem to be resolved.

We have taken pains to ensure that the data we used were as up-to-date as possible—the determination of the parton momentum distributions was, in fact, repeated many times to accommodate revisions of the BCDMS $F_2^{\mu p}$ data, the NMC $F_2^{\mu n}/F_2^{\mu p}$ data and the CDHSW $F_2^{\nu N}$ and $xF_3^{\nu N}$ data.

We have tried to be systematic in our methods, for example, in the way we have calculated the high-x ratio of the valence quarks, the way we have tried to break the correlation between the 'hardness' of the gluon distribution and $\Lambda_{\overline{\rm MS}}$, and our determination of the sea quark distribution (for which we do not assume SU(3) flavour symmetry but use the more realistic $\overline{s} = \overline{u}/2 = \overline{d}/2$ as indicated by the dimuon neutrino data).

We have also attempted a kind of 'error analysis' of the gluon distribution to show, in particular, what behaviours are possible in the very important low-x region and have also shown predictions for processes which look promising for pinning down this behaviour.

Appendix: the Cross-Section of the Drell-Yan Process

Here we present the explicit expressions for the differential cross-section of the data of the E605 collaboration based on those given by Kubar *et al.* [81], but tranformed into the $\overline{\rm MS}$ scheme by W.J. Stirling. For convenience, we have set

$$A = \frac{4\alpha^2(Q^2)}{3\pi} \tag{01}$$

$$w_1 = -t_1 \ln x_1 \tag{02}$$

$$w_2 = -t_2 \ln x_2 \tag{03}$$

and defined functions

$$G_A(\xi_1,\xi_2) = \frac{(\tau+\xi_1\xi_2)(\tau^2+(\xi_1\xi_2)^2)}{(\xi_1\xi_2)^2(\xi_1+x_1)(\xi_2+x_2)} \tag{04}$$

$$H_A(\xi_1,\xi_2) = \frac{-2\tau(\tau+\xi_1\xi_2)}{\xi_1\xi_2(\xi_1 x_2+\xi_2 x_1)^2} \tag{05}$$

$$G_C(\xi_1,\xi_2,\xi_3,\xi_4) = \frac{\xi_4(\tau+\xi_1\xi_2)(\tau^2+(\tau-\xi_1\xi_2)^2)}{\xi_1^3\xi_2^2(\xi_1\xi_4+\xi_2\xi_3)(\xi_2+\xi_4)} \tag{06}$$

$$H_C(\xi_1,\xi_2,\xi_3,\xi_4) = \frac{\tau(\tau+\xi_1\xi_2)(\xi_1\xi_2^2\xi_3+\tau(\xi_1\xi_4+2\xi_2\xi_3))}{(\xi_1\xi_2)^2(\xi_1\xi_4+\xi_2\xi_3)^3} \tag{07}$$

where the dilogarithm function, Li_2, is

$$\mathrm{Li}_2(\xi) = \sum_{n=1}^{\infty} \frac{\xi^n}{n^2} \,. \tag{08}$$

We have shown the convolution with the structure functions explicitly in terms of the joint probability distribution functions

$$J_{qq}(\xi_1,\xi_2) = \sum_q e_q^2(q(\xi_1)\overline{q}(\xi_2)+q(\xi_2)\overline{q}(\xi_1)) \tag{09}$$

$$J_{qg}(\xi_1,\xi_2) = \sum_q e_q^2(g(\xi_1)(q(\xi_2)+\overline{q}(\xi_2))+g(\xi_2)(q(\xi_1)+\overline{q}(\xi_1))) \tag{010}$$

and it only remains to integrate over t_1 from x_1 to 1 and over t_2 from x_1 to 1 to obtain the physical differential cross-sections from these sub-process ones.

The "annihilation" contribution is

$$
\begin{aligned}
&\text{“}J \otimes \frac{d\hat{\sigma}^A}{d\sqrt{\tau}dy}\text{”} = \\
&J_{qq}(x_1,x_2)[1+\frac{A}{2}(-8+\pi^2-\ln^2 x_1-2\mathrm{Li}_2(1-x_1)-\ln^2 x_2-2\mathrm{Li}_2(1-x_2) \\
&+\ln^2\left(\frac{1-x_1}{x_1}\right)+\ln^2\left(\frac{1-x_2}{x_2}\right)+2\ln\left(\frac{x_1}{1-x_1}\right)\ln\left(\frac{x_2}{1-x_2}\right))] \\
&+w_1\frac{A}{2}[(J_{qq}(t_1,x_2)\frac{(t_1^2+x_1^2)}{t_1^2}\ln\left(\frac{2x_1(1-x_2)}{x_2(t_1+x_1)}\right)-J_{qq}(x_1,x_2)2\ln\left(\frac{1-x_2}{x_2}\right)\cdot\frac{1}{t_1-x_1} \\
&+((1+(x_1/t_1)^2)J_{qq}(t_1,x_2)-2J_{qq}(x_1,x_2))\frac{\ln(1-(x_1/t_1))}{t_1-x_1} \\
&-J_{qq}(t_1,x_2)(-\frac{1}{t_1}+\frac{x_1}{t_1^2}+(1+(x_1/t_1)^2)\frac{\ln(x_1/t_1)}{t_1-x_1})) \\
&+w_2\frac{A}{2}[(J_{qq}(t_2,x_1)\frac{(t_2^2+x_2^2)}{t_2^2}\ln\left(\frac{2x_2(1-x_1)}{x_1(t_2+x_2)}\right)-J_{qq}(x_2,x_1)2\ln\left(\frac{1-x_1}{x_1}\right)\cdot\frac{1}{t_2-x_2} \\
&+((1+(x_2/t_2)^2)J_{qq}(t_2,x_1)-2J_{qq}(x_2,x_1))\frac{\ln(1-(x_2/t_2))}{t_2-x_2} \\
&-J_{qq}(t_2,x_1)(-\frac{1}{t_2}+\frac{x_2}{t_2^2}+(1+(x_2/t_2)^2)\frac{\ln(x_2/t_2)}{t_2-x_2})) \\
&+w_1w_2A[(J_{qq}(t_1,t_2)G_A(t_1,t_2)-J_{qq}(t_1,x_2)G_A(t_1,x_2) \\
&-J_{qq}(x_1,t_2)G_A(x_1,t_2)+J_{qq}(x_1,x_2)G_A(x_1,x_2))\cdot\frac{1}{(t_1-x_1)(t_2-x_2)} \\
&+J_{qq}(t_1,t_2)H_A(t_1,t_2)]
\end{aligned}
\tag{011}
$$

and the "Compton" contribution is

$$
\begin{aligned}
&\text{“}J \otimes \frac{d\hat{\sigma}^C}{d\sqrt{\tau}dy}\text{”} = \\
&\frac{3}{8}Aw_1J_{qg}(t_1,x_2)(\frac{x_1^2+(t_1-x_1)^2}{2t_1^3}\ln\frac{2(t_1-x_1)(1-x_2)}{x_2(t_1+x_1)}+\frac{1}{2t_1}) \\
&+\frac{3}{8}Aw_2J_{qg}(t_2,x_1)(\frac{x_2^2+(t_2-x_2)^2}{2t_2^3}\ln\frac{2(t_2-x_2)(1-x_1)}{x_1(t_2+x_2)}+\frac{1}{2t_2}) \\
&+\frac{3}{8}Aw_1w_2((J_{qg}(t_1,t_2)G_C(t_1,t_2,x_1,x_2,\tau)-J_{qg}(t_1,x_2)G_C(t_1,x_2,x_1,x_2,\tau))\cdot\frac{1}{t_2-x_2} \\
&+J_{qg}(t_1,t_2)H_C(t_1,t_2,x_1,x_2,\tau)) \\
&+\frac{3}{8}Aw_2w_1((J_{qg}(t_2,t_1)G_C(t_2,t_1,x_2,x_1,\tau)-J_{qg}(t_2,x_1)G_C(t_2,x_1,x_2,x_1,\tau))\cdot\frac{1}{t_1-x_1} \\
&+J_{qg}(t_2,t_1)H_C(t_2,t_1,x_2,x_1,\tau))
\end{aligned}
\tag{012}
$$

References

1. Langacker, P., *Phys. Rep.* **72C**, 185 (1981).
2. Fayet, P. & Ferrara, S., *Phys. Rep.* **32C**, 249 (1977).
3. Schwarz, J.H. (ed.), *Superstrings—The First 15 Years* (World Scientific, Singapore, 1985).
4. Aitchison, I.J.R. & Hey, A.J.G., *Gauge Theories in Particle Physics* (Adam Hilger Ltd., Bristol, 1982).
5. Halzen, F. & Martin, A.D., *Quarks and Leptons: An Introductory Course in Modern Particle Physics* (John Wiley & Sons, Inc., New York, 1984).
6. Itzykson, C. & Zuber, J.-B., *Quantum Field Theory* (McGraw-Hill Book Company, New York, 1980).
7. Bjorken, J.D., *Proceedings of the* 3^{rd} *International Symposium on* $e-p$ *Interactions,* Stanford
8. Feynman, R.P., *Phys. Rev. Lett.* **23**, 1415 (1969).
9. Bjorken, J.D. & Paschos, E.A., *Phys. Rev.* **D1**, 3151 (1970).
10. Bjorken, J.D. & Paschos, E.A., *Phys. Rev.* **185**, 1975 (1969).
11. Feynman, R.P., *Photon-Hadron Interactions* (ed. W.A. Benjamin, New York, 1972).
12. Kogut, J. & Susskind, L., *Phys. Rep.* **8**, 76 (1973).
13. Callan, C.G. & Gross, D., *Phys. Rev. Lett.* **22**, 156 (1969).
14. Bjorken, J.D., *Phys. Rev.* **163**, 1767 (1967).
15. Bjorken, J.D., *Phys. Rev.* **179**, 1547 (1969).
16. BCDMS: Benvenuti, A.C. et al., *Phys. Lett.* **223B**, 485 (1989).
17. Gell-Mann, M., *Phys. Lett.* **8**, 214 (1964).
18. Zweig, G., *CERN Report* **8419/Th 412**, (1964).
19. Politzer, H.D., *Phys. Rep.* **14C**, 129 (1974).

20. Marciano, W. & Pagels, H., *Phys. Rep.* **36C**, 137 (1978).

21. Pennington, M.R., *Rep. Prog. Phys.* **46**, 393 (1983).

22. Altarelli, G. & Parisi, G., *Nucl. Phys.* **B126**, 298 (1977).

23. Gribov, V. & Lipatov L., *Yad. Fiz.* **15**, 78,1218 (1972).

24. Lipatov, L., *Yad. Fiz.* **20**, 181 (1974).

25. Politzer, H.D., *Phys. Rev. Lett.* **30**, 1346 (1973).

26. Buras, A., *Rev. Mod. Phys.* **52**, 199 (1980).

27. Dokshitzer, Y., Dyakonov, D. & Troyan, S., *Phys. Rep.* **58**, 269 (1980).

28. Altarelli, G., *Phys. Rep.* **81C**, 1 (1982).

29. Altarelli, G. et al., *Nucl. Phys.* **B153**, 52 (1978).

30. Altarelli, G. et al., *Nucl. Phys.* **B157**, 461 (1979).

31. Milsztajn, A., *DPhPE preprint* **90-07**, (1990).

32. EMC: Aubert, J.J. et al., *Nucl. Phys.* **B259**, 189 (1985).

33. Virchaux, M., *DPhPE preprint* **90-07**, (1990).

34. Whitlow, L.W. et al., *SLAC preprint* **SLAC-PUB-5100**, (1989).

35. Martin, A.D., Roberts, R.G. & Stirling, W.J., *Phys. Lett.* **B206**, 327 (1988).

36. CDHSW: Berge, J.P. et al., *CERN preprint* **EP/89-103**, (1989).

37. CCFRR: MacFarlane, D. et al., *Zeit. Phys.* **C26**, 1 (1984).

38. Whitlow, L., PhD thesis, *SLAC-REPORT* **357**, (1990).

39. BCDMS: Benvenuti, A.C. et al., *Phys. Lett.* **237B**, 592 (1990).

40. EMC: Aubert, J.J. et al., *Nucl. Phys.* **B293**, 740 (1987).

41. Martin, A.D., Roberts, R.G. & Stirling, W.J., *Mod. Phys. Lett.* **A4**, 1135 (1989).

42. BCDMS: Benvenuti, A.C. et al., *CERN preprint* **EP/89-171**, (1989).

43. NMC: presented by J. Nassalski at *Europhysics Conference on High Energy Physics,* Madrid (1989).

44. Brodsky, S.J. & Farrar, G., *Phys. Rev. Lett.* **31**, 1153 (1973).

45. Brodsky, S.J. & Farrar, G., *Phys. Rev.* **D11**, 1309 (1975).

46. Matveev, V.A., Murddyan, R.M., Tavkheldize, A.N., *Lett. Nuo. Cim.* **7**, 719 (1973).

47. Close, F.E.: 'Structure Functions and Counting Rules' in Proceedings of the 19^{th} International Conference on High Energy Physics, Tokyo (1978)

48. EMC: Aubert, J.J. et al., *Nucl. Phys.* **B213**, 31 (1983).

49. Martin, A.D., Roberts, R.G. & Stirling, W.J., *Phys. Lett.* **228B**, 149 (1989).

50. CCFR: Foudas, C. et al., *Phys. Rev. Lett.* **64**, 1207 (1990).

51. Particle Data Group, *Phys. Lett.* **B204**, (1988).

52. Devoto, A., Duke, D.W., Owens, J.F., Roberts, R.G., *Phys. Rev.* **D27**, 508 (1983).

53. Hamming, R.W., *Introduction to Applied Numerical Analysis* (McGraw-Hill, New York, 1971).

54. Bevington, P.R., *Data Reduction and Error Analysis for the Physical Sciences* (McGraw-Hill, New York, 1969).

55. Aurenche, P. et al., *Phys. Lett.* **140B**, 87 (1984).

56. Aurenche, P. et al., *Phys. Lett.* **169B**, 441 (1986).

57. Aurenche, P. et al., *Nucl. Phys.* **B297**, 661 (1988).

58. Aurenche, P. & Whalley, M.R., *Durham-RAL HEP Database* **RAL-89-106**, (1989).

59. Aurenche, P. et al., *Phys. Rev.* **D39**, 3275 (1989).

60. Grunberg, G., *Phys. Lett.* **95B**, 70 (1980).

61. Grunberg, G., *Phys. Rev.* **D29**, 2315 (1984).

62. Stevenson, P.M., *Phys. Lett.* **100B**, 161 (1981).

63. Stevenson, P.M., *Phys. Rev.* **D23**, 2916 (1981).

64. Stevenson, P.M. & Politzer, H.D., *Nucl. Phys.* **B277**, 758 (1986).

65. Duke, D.W., Owens, J.F., *Phys. Rev.* **D30**, 49 (1984).

66. WA70 Collaboration: Bonesini, M. et al., *Zeit. Phys.* **C38**, 371 (1988).

67. Aurenche, P. *(Private communication)*

68. Drell, S.D., Yan, T.M., *Phys. Rev. Lett.* **24**, 181 (1970).

69. Drell, S.D., Yan, T.M., *Ann. Phys. (New York)* **66**, 595 (1971).

70. E605: C.N. Brown *et al.*, *Phy. Rev. Lett.* **63**, 2637 (1989).

71. Eichten, E., Hinchliffe, I., Lane, K. & Quigg, C., *Rev. Mod. Phys.* **56**, 579 (1984).

72. Diemoz, M., Ferroni, F., Longo, E., & Martinelli, G., *Zeit. Phys.* **C39**, 21 (1988).

73. Harriman, P.N. *(In preparation)*

74. Blümlein, J., Klein, M., Naumann, Th., & Riemann, T., *Proceedings of the HERA Workshop,* ed. R.D. Peccei, DESY 1988, Vol.1, page 67.

75. Blümlein, J., Ingelman, G., Klein, M., & Rückl, R., *DESY preprint* **89-101**, (1989).

76. Kwiecinski, J., Martin, A.D., Roberts, R.G. and Stirling, W.J., *RAL preprint* **90-053**, (1990).

77. Martin, A.D., Roberts, R.G. & Stirling, W.J., *Phys. Rev.* **D37**, 1161 (1988).

78. Tkaczyk, S.M., Stirling, W.J. & Saxon, D.H., Proc. HERA Workshop, ed. R.D. Peccei, DESY 1988, Vol.1, page 265.

79. Cooper-Sarkar, A.M., Ingelman, G., Long, K.R., Roberts R.G. & Saxon, D.H., Proc. HERA Workshop, ed. R.D. Peccei, DESY 1988, Vol.1, page 231; Zeit. Phys. **C39**, 281 (1988).

80. Martin, A.D., Ng, C.-K. & Stirling, W.J., *Phys. Lett.* **191B**, 200 (1987).

81. Kubar, J., Le Bellac, M., Meunier, J.L. & Plaut, G., *Nucl. Phys.* **B175**, 251 (1980).